2010

SYNTHESIS, FUNCTIONALIZATION AND CHARACTERIZATION OF DUAL MODE NANOPARTICLES FOR BIOMEDICAL APPLICATIONS

Farah Radwan
Virginia Commonwealth University

SYNTHESIS, FUNCTIONALIZATION AND CHARACTERIZATION OF DUAL MODE NANOPARTICLES FOR BIOMEDICAL APPLICATIONS

A dissertation submitted in partial fulfillment of the requirement for the degree of Doctor of Philosophy at Virginia Commonwealth University.

by

Farah Nazih Radwan
B.S. Virginia Commonwealth University, 2005

Director: Dr. Everett E. Carpenter
Associate Professor, Department of Chemistry

Virginia Commonwealth University
Richmond, Virginia
July, 2010

ACKNOWLEDGMENTS

I would like to thank my advisor, Dr. Everett Carpenter for his continuous help, guidance, patience, and encouragement throughout the past five years. Dr. Carpenter has been extremely supportive during very tough times in my life, which gave me strength and determination to continue my studies, and for that I will forever be grateful. I consider myself very lucky to have had this great opportunity to be one of his students. I am also thankful for my committee members Dr. Maryanne Collinson and Dr. Joseph Topich for their time, guidance and valuable advice. I want to express thanks to Dr. Lidia Vallarino who inspired and motivated me to take my first steps towards research in chemistry. I would like to acknowledge the chemistry department here at VCU as it has been my home for the past 9 years. I have learned so much from the remarkable people in it, students and faculty, which I have met and got to know over the years.

I would like to dedicate few lines to express my appreciation to my loving family. I want to thank my father who has always believed in me and encouraged me to pursue my dreams. I want to thank my mother for her love, support and hard work that made it possible for this work to be accomplished. I am also very fortunate to have helpful and caring siblings, Sara, Forsan, Motaz and Ahmad that I want thank for their love and support.

Table of Contents

List of Figures

List of abbreviation

Fe@FeOx	Iron core and iron (II/III) shell
APD	2-amino-1,3- propae diol
TEM	Transmission Electron Microscopy
XPS	X-ray Photon Spectroscopy
MALDI	Matrix- assisted Laser Desorption Ionization
VSM	Vibrating Sample Magnetometer
CdS	Cadmium sulfide
XRD	X-ray powder diffraction
QDs	Quantum dots
PB@Fe	Prussian blue coated iron nanoparticles
UV	Ultraviolet
$MnFe_2O_3$	Manganese iron oxide
Ag@Ni	Silver core and nickel shell
CdSe	Cadmium selenide
ZnS	Zink sulfide
IR	Infrared
χ	susceptibility
M-H	Magnetization-Applied field
M_s	Magnetization saturation
M_r	Remnant magnetization
H_c,	Coercivity
A	Exchange constant
ΔE	Energy barrier
K	Anisotropy constant
V	Particles volume
k_B	Boltzmann constant
T	Temperature
MRI	Magnetic Resonance Imaging
α-Fe_2O_3	Maghemite
γ- Fe_2O_3	Hematite
Fe_3O_4	Magnetite
Cy5.5	Cyanine fluorescent dye
FITC	Fluorescein isothiocyanate
ΔG	Free energy change
V	Molecular volume of the precipitated solid
r	Radius of the nuclei
k_B	Boltzmann constant
S	Saturation ratio
T	Temperature
γ	Surface free energy per unit surface area

r*	Critical size of the nuclei
CMC	Critical micelles concentration
ω	Water to surfactant molar ratio
υ	Molecular volume of surfactant
σ	The area per polar head
l	The length of the hydrophobic part of the surfactant
R	The radius of sphere
∑	Surface of the sphere
DNA	Deoxyribonucleic acid
ξ	Zeta potential
PEG	Poly ethylene glycol
PS-PAA	Polystyrene-ploy(acrylic acid) block copolymer
DMSA	2,3 dimercaptosuccinic
Fe	Iron
O	Oxygen
P	Phosphorous
APD	2-amino-1,3-propane diol
$NaBH_4$	Sodium borohydride
$NiCl_2.\ 6H_2O$	Nickel chloride hexahydrate
U293	Human kidney cells
PBS	Phosphate buffer saline
FOOH	Iron oxyhydroxide
TEM	Transmission electron microscopy
XPS	X-ray Photon Spectroscopy
IR	Infrared spectroscopy
UV-vis	Ultraviolet- visible absorption spectroscopy
MALDI/ TOF	Matrix assisted laser desorption/ ionization/ time of flight spectroscopy
VSM	Vibrating sample magnetometer
CCD	Charged coupled device
FT-IR	Fourier transform- Infrared spectroscopy
KBr	Potassium bromide
KE	Kinetic energy
hυ	Energy for X-ray source
σ	Bonding sigma orbital
σ*	Antibonding sigma orbital
π	Bonding pi orbital
π	Antibonding pi orbital
OH^-	Hydroxide anion
C	Carbon
m/z	Mass to charge ratio
N	Nitrogen
CdTe	Cadmium telluride
ZnS	Zinc Sulfide

GaAs	Gallium Arsenide
InP	Indium phosphide
PbTe	Lead telluride
SnTe	Tin telluride
E_g	Band gap energy
CdSe	Cadmium selenide
DHLA	Dihydrolipoic acid
TOPO	Trioctylphosphine oxide
TOP	Trioctylphoshine
HDA	Hexadecylamine
ODE	Octadecane
AOT	Sodium dioctyl sulfosuccinate
MPA	Mercaptopropoinic acid
H_2O	Water
$Cd(CH_3COO)_2.\ 2H_2O$	Cadmium acetate dihydrate
$NaS.\ 9H_2O$	Sodium sulfide nonahydrate
n	The order of diffracted beam
n	Nonbonding(lone-pair) orbital
λ	Wavelength of incident X-ray beam
d	Space between adjacent plane of atoms
θ	Angle of incidence of X-ray beam
Cu	Copper
JCPDS	Joint Committee on Powder Diffraction Standards
CdS@Fe	Cadmium sulfide coated iron nanoparticles
PB	Prussian blue
$Fe^{III}_4Fe^{II}(CN)_6.\ xH_2O$	Ferric ferrocyanide
FCC	Face centered cubic
Fe(II)	Iron (II)
Fe(III)	Iron (III)
MRI	Magnetic Resonance Imaging
$K_2\ Fe^{II}Fe^{II}(CN)_6$	Prussian white
$Fe^{III}Fe^{III}(CN)_6$	Berlin green
Tc	Curie temperature
Co(II)	Cobalt (II)
Co(III)	Cobalt (III)
Mn	Manganese
CN	Cyanide
TGA	Thermogravimetric analysis
N_2	Nitrogen gas
DSC	Differential scanning Calorimetry
α-Fe	Alpha iron
FC	Field cooled
ZFC	Zero Field cooled
SQUID	Superconducting quantum interference devices

$FeCl_2.\ 4H_2O$ Iron (II) chloride tetrahydrate

NP	Nonylphenoxypoly(ethylenoxy)ethanols
NP4	Nonylphenoxypoly(ethylenoxy)ethanols with 4 repeating(ethylenoxy) units
NP7	Nonylphenoxypoly(ethylenoxy)ethanols with 7 repeating(ethylenoxy) units
NP5	Nonylphenoxypoly(ethylenoxy)ethanols with 5 repeating(ethylenoxy) units
NP9	Nonylphenoxypoly(ethylenoxy)ethanols with 5 repeating(ethylenoxy) units

Abstract

SYNTHESIS, FUNCTIONALIZATION AND CHARACTERIZATION OF DUAL MODE NANOPARTICLES FOR BIOMEDICAL APPLICATIONS

By Farah N. Radwan

A dissertation submitted in partial fulfillment of the requirement for the degree of Doctor of Philosophy at Virginia Commonwealth University.

Virginia Commonwealth University, 2010

Director: Dr. Everett E. Carpenter
Associate Professor, Chemistry Department

Three different approaches were used to prepare dual mode nanoparticles using a previously described reverse micelle technique. Superparamagnetic Fe@FeOx core shell nanoparticles were chosen to be the magnetic component for all three dual mode systems.

In the first type of particles, 2- amino-1,3- propane diol (APD) was used as a functionalization ligand to stabilize the surface of the particles and its functional amino group also provided a binding site for the attachment of a fluorescent probe.

The TEM analysis showed that the APD coated particles have a size range of 8-13 nm while XPS and MALDI measurements confirmed the presence of the APD ligand on the surface of the particles. The VSM data showed that the magnetization of the unfuntionalized particles was 60 emu/g and after functionalization the magnetization became 33 emu/g. The slight reduction magnetization was a result of the organic surface coating of APD. At this point, we realized that attaching a bulky organic fluorescent probe will cause the particles' magnetization to further decrease. Therefore, our attention was directed towards inorganic semiconductors nanoparticles to be used as the optical component of the dual mode particles.

The second approach included replacing the FeOx shell around the metallic iron core with a quantum dots shell (QDs). Thioglycerol was used to stabilize the surface of the synthesized CdS particles. The diffraction pattern of the produced particles was in agreement with the reference patterns of both alpha iron and CdS hexagonal crystal lattice, as illustrated by the XRD measurements. The TEM images of the coated particles revealed core shell morphology before the addition of thioglycerol and the particles were aggregated. After thioglycerol was added, the particles became more isolated with an approximate size of 14 nm. Optical measurements of the coated particles showed an emission peak at 670 nm using an absorbance peak of 335 nm. XPS scans verified the presence of CdS shell on the surface of the iron particles. The magnetization of the coated particles was 22 emu/ g, which is lower than that of the APD coated particles. Although, the optical properties of the dual mode system were enhanced, the magnetization was reduced. This leads to our third approach in preparing the dual mode system,

we used organometallic Prussian blue compound as our optical probe. Similar to the XRD data of the CdS@Fe nanoparticles, the core consists of metallic iron for PB@Fe nanoparticles. The TEM images showed core shell morphology and approximate size of 11 nm. The attachment of PB ligand on the surface of the particles was verified using XPS and the magnetic data revealed that PB@Fe nanoparticles has the highest magnetization value of 80 emu/ g and it's the highest in comparison to the previous two system.

In conclusion, we have taken three approaches to develop magnetic and optical dual mode nanoparticles. Each system has its advantages and limitations. For instance, CdS nanoparticles have the most enhanced optical properties but the lowest magnetization. On the other hand PB@Fe has the highest magnetization saturation but not the optimal optical properties. Future work includes the improvement of both the magnetic and optical properties of these systems.

Chapter 1: Introduction

I. Nanoparticles properties

Indisputably, the field of nanomaterials has been the center of attention for decades; it has invaded the laboratories of many researchers and mesmerized their thoughts and vision. This fascination with nanoparticles is not entirely recent, in fact it dates back to the middles ages, specifically in Mesopotamia, when a thin layer of silver and copper nanoparticles (known as luster) was used to add iridescence effect to Medieval pottery.[1] This was followed by the use of gold nanoparticles colloids, which appeared red instead of gold, to color glass windows in the seventeenth century.[2] Since then, many other advances in the nanomaterials field followed, for instance, the use of zinc oxide nanoparticles in sunscreen lotions, due to their advanced UV blocking abilities in comparison to their bulk counterparts.[3] Furthermore, it was found that silicon nanoparticles with the size range of 40-100 nm are among the hardest materials known including its bulk equivalent.[4] Also, multicolor semiconductor nanoparticles and florescent carbon nanotubes are yet just few more examples of the advancement in nanoscience.[5,6]

Researchers have realized that nanomaterials acquire unique chemical, physical, optical, electronic and magnetic properties that differ from their larger counterparts (bulk materials) or their smaller sized materials (single atoms).[7-11] However, it was not until few decades ago that a better understanding of nanomaterials was achieved. There are many reasons behind these changes in properties; the nanosize of these particles is considered to have a crucial and an essential role in this modification. Although researchers hold opposing views on what size range a particle is considered to be in the nanoscale, many agree that nanoparticles fall into the size range of 1-100 nm.[12,13] Consequently, these particles can be used in a variety of applications, in the medical field, for instance, nanoparticles can be used in targeted drug delivery, since human cells are about 10 μm in diameter, these nanosized particles can easily be introduced to the cells.[14] In addition, this size reduction can lead to the appearance of unique optical properties in certain materials, such as semiconductors, leading to their use as fluorescent biological labels.[15]

The size of these materials, their shape, and their composition also take part in the change in properties between their bulk phase and the nano phase.[8,12] The shape of the particles affects their use in different applications, namely magnetic ones, such as in data storage and advanced magnets. As reported by Zeng et al., the shape of $MnFe_2O_3$ nanoparticles influences their magnetic properties including anisotropy which is defined as the alignment of a material's magnetic moment with its easy axis and it is influenced by the crystal structure's shape of these particles.[16]

The choice of the application in which nanoparticles are suitable does not only depend on the size of the particles but also on the composition. Metal alloys differ in their physical and chemical properties from nanoparticles composed of one type of metal. As shown by Mottet et al., doping Ni or Cu impurities in Ag nanoclusters affect their thermal stability by increasing their melting points.[17] On top of the change in thermal stability, the structural, thermodynamic, and electronic stabilities can be modified by changing the nanoparticles composition. As illustrated by Rossi et al., Ag@Ni core shell nanoclusters are under examination to be used in optoelectronic or single-electron tunneling devices instead of either pure Ag or Ni nanoparticles alone.[18] The following sections include a detailed overview of the unique properties of nanoparticles, the origin of these properties and their importance.

I.1. Chemical properties

Although the reduction in size is not the only factor leading to these unique properties, at the nanoscale however, it has a main effect on modifying the surfaces and interfaces of these materials. Consequently, the chemical properties of these materials will be altered.[11] For instance, at the nanoscale regime, the surface to volume ratio of these materials increases leading to an increase in the number of the surface atoms available for different activities. This surface adjustment made these nanoparticles, namely transition metals, very appealing to be used in catalysis. Nanoparticles have higher accessibility to their surface atoms and larger coordination number resulting in

enhanced reactivity in comparison to their bulk counterparts, they are also considered to be green catalysts since they provide hazard-free and solvent-free single step synthesis.[8,19-21] For example platinum nanoparticles supported on ionic liquids were used to catalyze the selective hydrogenation reaction of alkynes under mild conditions.[22]

I.2. Optical and electronic properties

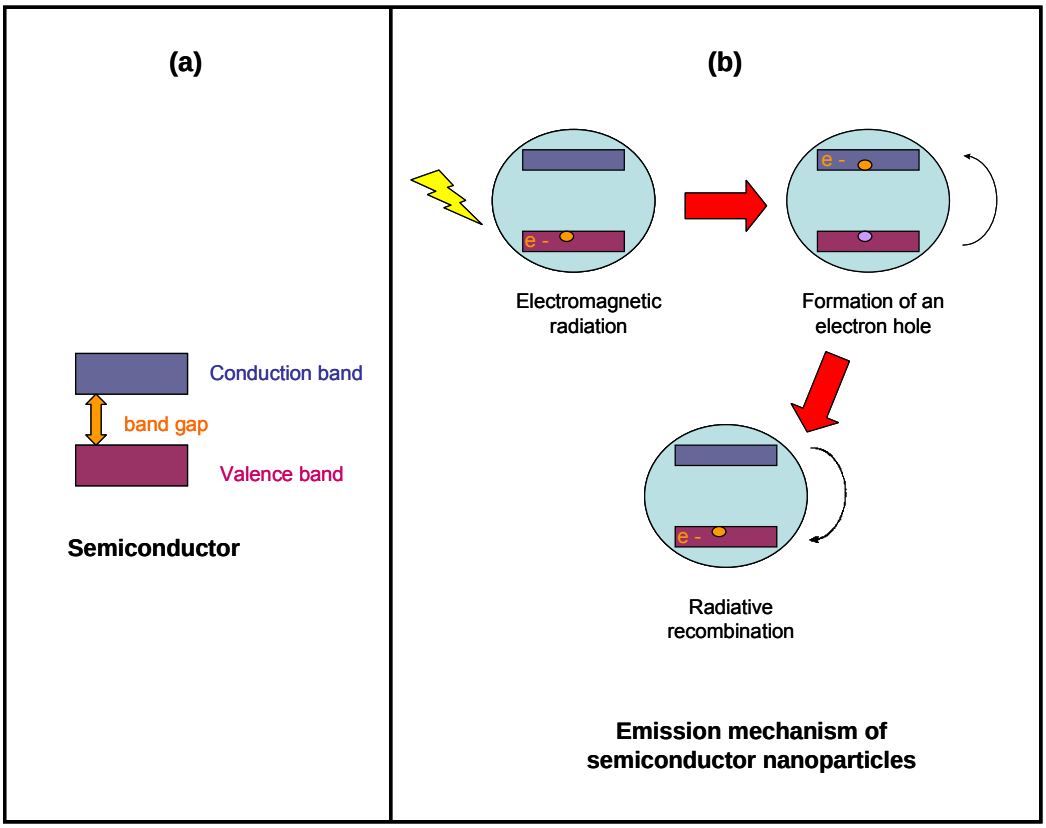

Figure 1-1: Optical properties

Another outcome of size reduction is the appearance of unique optical properties of these materials at the nanoscale. These optical properties originate due to either the

quantum confinement effect in semiconductors or the surface plasmon resonance in certain conductors.

Figure 1-1 (a) shows that in bulk semiconductor materials there is a band gap of a certain energy between the valence and the conduction bands.[23] Light emission in bulk semiconductors take place by the promotion of an electron from the valence band to the conduction band upon excitation leaving a hole in the conduction band. When the electron relaxes back to the valence band it recombined with the whole and emits light with energy equal to the energy of the band gap. As the size of the bulk material decreases to the nanoscale, the particle size becomes comparable or smaller than the exciton's Bohr radius which is the distance between the electron and the hole pair. Accordingly, one or more dimensions of the bulk material will become restricted to the nanoscale altering its band gap and the energy of the emitted light, this change is referred to as the quantum confinement effect.[24-26] This effect will be further discussed in chapter 4 along side with the light emission mechanism of quantum dots. These light emitting semiconductors nanocrystals are made from I-VII, II-V, III-V and IV materials, such as CdS, CdSe and ZnS to mention a few.[27]

Light emitting nanoparticles are not only limited to semiconductors, other nanostructures with unique optical properties also exist such as fluorescent metallic silver and gold nanoparticles. Metals are surrounded by weakly attracted electrons which generate an electron cloud around their surface; known as the surface plasmon. In general, when a metal is excited by electromagnetic radiation, the surface plasmon

absorbs the light causing a vibration, the surface plasmon then becomes excited. Subsequently, the absorbed energy will dissipate in the form of emitted light with a specific wavelength. In bulk metals, the emitted light cannot be seen because it has a wavelength that falls in the IR region of the electromagnetic spectrum.[28] However, in metallic nanoparticles, the emitted light falls in the visible range of the spectrum and therefore it can be seen. The reason behind nanoparticles' light emission properties is that metallic nanoparticles have larger surface area than their bulk counterparts and hence, more surface atoms are present in the metallic nanoparticles. Since more energy is absorbed, more surface plasmon resonance is generated and consequently the light with higher energy but lower wavelength is emitted.[29-32] Just as the unique chemical properties of these nanocrystals allows for their use in certain applications such as catalysis, their distinctive optical properties facilitate their access into variety of other applications. In the biomedical field for instance, light emitting semiconductors were used in live cell imaging, such as lymph node mapping and imaging of targets expressed in tumor vasculature.[33-35]

Semiconductors nanocrystals also have exceptional electronic qualities, such as high-temperature stability and higher defect and radiation tolerance which have paved the way for them to be used in opto-electronic and single electron devices.[36-38] It is worthy to note that all of these distinguished electronic properties were yet another result of the quantum confinement effect. The magnetic properties of the bulk materials are also

affected by the decrease in the materials dimensions to the nanoscale as shown in the next section.

I.3. Magnetic properties

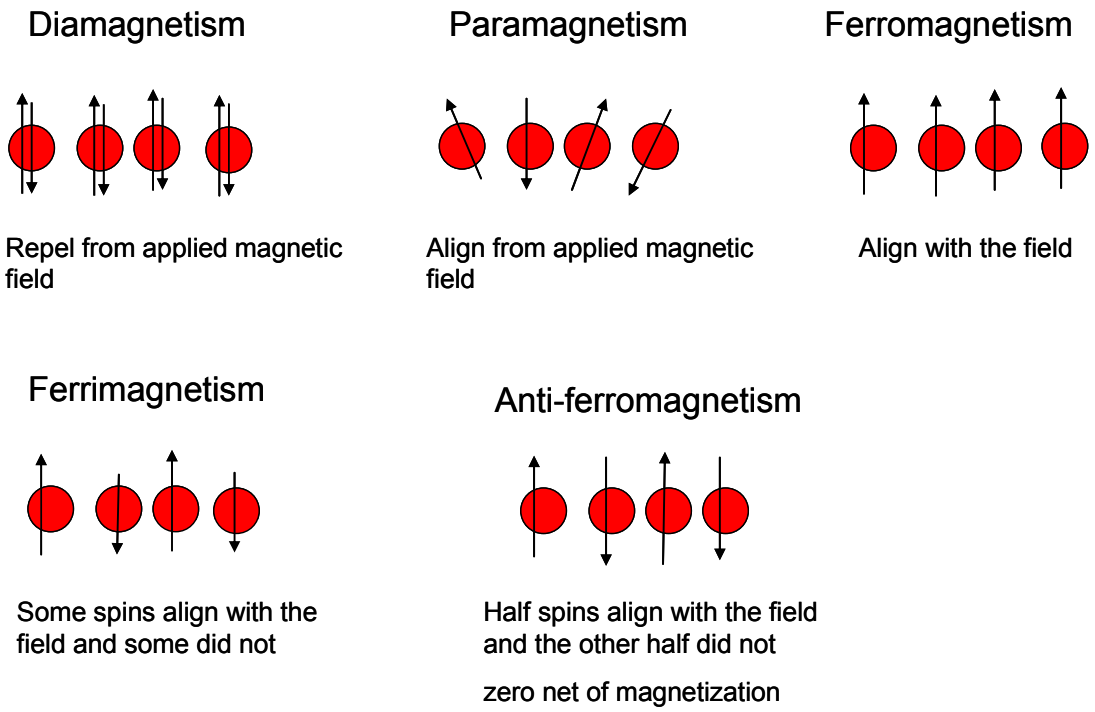

Figure 1-2: Schematic of the main five kinds of magnetism in response to an applied magnetic field. Diamagnetic and anti-ferromagnetic materials have a zero net magnetization while para-, ferro- and antiferromagnetism have a net magnetic moment in the direction of the applied field.

The change in the magnetic properties of bulk metallic materials is another outcome of the decrease in the size to the nanoscale regime. However, understanding magnetism in bulk metals is an essential step on the way into understanding the magnetism of these same metals at the nanoscale.

Magnetism background

Figure 1-2 shows the five main types of magnetism; these types can be separated into two main categories based on their response to an applied magnetic field. The first category includes paramagnetism, ferro and ferrimagnetism which are present in materials that are attracted to the applied magnetic field. These materials have unpaired electrons in their valence atomic shell.[39] The unpaired electrons align in the same direction as the applied field resulting in a net magnetic moment leading to a positive susceptibility (χ).[39] The response of the magnetic moments of electron spins to an applied field is defined as the susceptibility.[39]

In a paramagnetic material, the spins of the electrons are not coupled as shown in Figure 1-2 (b). As a result they have short range magnetic order because they relax back to their original random state in the absence of magnetic field.[39] The spins in a ferromagnet align with the applied field (Figure 2-1 (c)). However, they are coupled and aligned parallel to each other in the same direction as the applied field.[39] Consequently, ferromagnetic materials have larger positive susceptibility and long range order.[39] In ferrimagnetic material the spins have non-equalvent magnitudes and align in an antiparallel fashion as presented in Figure 1-2 (d). The net magnetic moment in

ferromagnetic materials (resulting from spins with stronger magnitudes) aligns in the direction of the applied field. The second category contains the remaining types of magnetism and they are present in materials that repel the magnetic field; these types are diamagnetism and antiferromagnetism. Diamagnetic material has paired electrons in their valence shell as illustrated in Figure 1-2 (a). The spins in diamagnetic materials align in an opposite direction to the field leading to negative susceptibility. Antiferromagnetic materials have zero net magnetization because they are of same magnitude but are coupled in an antiparallel fashion as shown in Figure 1-2 (e).

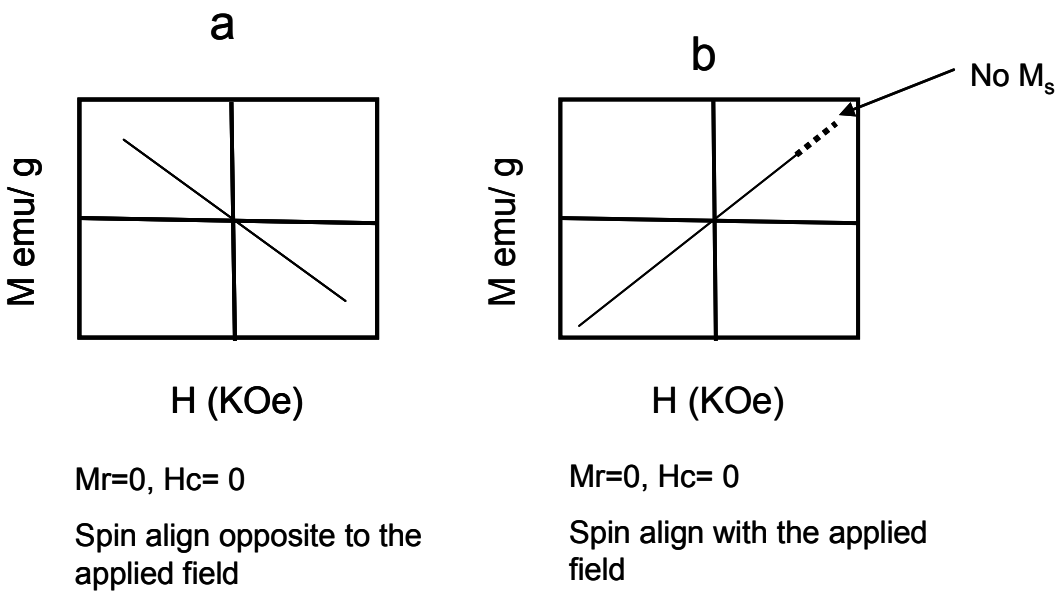

Figure 1-3: Magnetization vs. Field (M-H) curves of diamagnetism **(a)**, paramagnetism **(b)** M_s is the magnetization saturation, M_r is the remnant magnetization and H_c is the coercivity .

Figure 1-3 represents the curve of the magnetization (alignment of the spins with magnetic field) versus the applied field curve, commonly known as the M-H curves of diamagnetic (a), paramagnetic (b) materials. Figure 1-3 (a) shows an inverse relation between the applied field and the magnetization because the spins of a diamagnetic material oppose the direction of the applied field. On the contrary, part (b) of the Figure shows a direct relationship between the applied field and the magnetization because small portion of the spins of a paramagnetic material align in the same direction as the applied field. Thus paramagnetic material has no saturation magnetization (M_s) which is described as the alignment of all the spins of the particles with the applied external magnetic field.[40] Consequently it has zero remnant magnetization (M_r) which is the retention of magnetization in the absence of an applied magnetic field. Also, paramagnetic materials have zero coercivity (H_c), that is the required magnetic field to bring the particles magnetization to zero after it has reached saturation.[40]

In contrast, the M-H curve of ferromagnetic materials has a different shape. Since the spins in ferromagnetic materials are coupled and retain a long range order, the magnetic moments reach high magnetization saturation. Thus, ferromagnetic materials have a coercivity value higher than zero, because a certain amount of energy is needed to randomize the highly aligned spins, accordingly, they also retain magnetization after the applied field is removed.[41] Due to these properties the M-H curve of ferromagnetic material has the shape of hysteresis loop.[41]

Superparamagnetism

In bulk ferromagnetic materials, when an external magnetic field is applied the magnetic moments exhibit multi domain properties, each domain presents a group of spins that are aligned similarly and the domains are separated by domain walls.[42] When the bulk materials are reduced in size to the nanoscale, the width of the walls decrease as well until a certain size is reached, this size is called the critical size which is described as follows

$$2A^{1/2} / M_s \qquad (1)$$

where A is the exchange constant and M_s is the moment per unit volume, this critical size equals or smaller than 20 nm.[41,43] At this size, the spins act as a single domain and the magnetic behavior of the particles at this point is called superparamagnetic.[39,42,44] When an external magnetic field is applied, all the spins are aligned with the magnetic field reaching to a saturation magnetization. However, when the magnetic field is removed, the magnetic moments undergo magnetic relaxation governed by [41]

$$\Delta E = KV,\ KV = k_B T \qquad (2)$$

where ΔE is the energy barrier for the spins to relax back to their randomized state after reaching saturation, K is the anisotropy constant, V is the particles volume, k_B is the Boltzmann constant and T is the temperature.[45] At the nanoscale, the volume of the particle is reduced; accordingly the anisotropy component (KV) becomes comparable to

the thermal energy (k_BT). As a result, when the external field is removed, the electrons of the particles oscillate from one position to another due to thermal fluctuations, leading to zero remnant magnetization. Thus, no energy is needed to randomize the electrons after they reached magnetization saturation resulting in zero coercivity as well.[45]

Superparamagnetic properties of metallic nanoparticles make them outstanding candidates in many applications and specifically in the biomedical field due to their compatibility with the physiological conditions.[40,46-49] These applications include the use of superparamagnetic nanoparticles as MRI contrast agents, in targeted drug delivery and in the treatment of hyperthermia.[49-51] Our main biomedical application of interest is bio-imaging, which will be discussed briefly in the next section.

II. The application of biomarkers

Cancer detection is just as or even more important than cancer treatment, because malignant cells are much harder to treat and more dangerous in their advanced stages.[52] Accordingly, the need for a reliable detection system for early stage diagnosis is necessary and the use of biomarkers was considered for this purpose. Unlike traditional organic dyes and fluorescent proteins, nanoparticles have been used for more sensitive and precise biomarker detection as a result of their previously discussed unique optical, magnetic, physical and chemical properties.[53] Gold nanoparticles, magnetic nanoparticles, quantum dots carbon nanotubes and nanowires are all examples of the use

of nanoparticles as biomarkers. Gold nanoparticles can absorb and scatter light from the visible to near-infrared region due to their strong surface plasmon absorption and scattering which allowed their use as contrast agents for *in vivo* tumor imaging.[54] Pegylated colloidal gold nanoparticles have been used for *in vivo* tumor targeting.[55] They are also more biocompatible, less cytotoxic, resistant to photobleaching and they have size tunable properties.[53]

Quantum dots also have several advantages over traditional organic dyes; they are more resistant to photobleaching and they have size and composition tunable emission.[53] One of the most interesting and very useful properties of quantum dots is their broad excitation spectrum and narrow emission spectrum which eliminates or minimize the spectral interferences resulting from the excitation of different quantum dots sizes simultaneously.[53] Variety of biomolecules can be attached to the surface of the QDs in order for them to be used in many biomedical applications which provide a. multifunctional quantum dots that can be used in cancer targeting and drug delivery.[56]

Magnetic nanoparticles have been functionalized with QDs and antibody for the use in cancer targeting and separation.[57] Magnetic nanoparticles make exceptional candidates to be used as biomarkers due to their reduced bulk spin-spin relaxation time of the surrounding water molecules as a result of their aggregation which stems from their affinity to the molecular target.[53] For instance, superparamagnetic iron and iron oxide nanoparticles can be used as contrast agent for magnetic resonance imaging (MRI) technique to deliver higher resolution images.[58] To further improve bio-imaging, our goal

was to produce a dual mode system that is magnetic and fluorescent to enhance the application of bio-imaging.

II.1. Dual mode nanoparticles

Dual mode nanoparticles contain both optimum magnetic and fluorescent properties. Many researchers have identified the importance of such system in a variety of biomedical applications including targeted drug delivery, bio-imaging and the magnetic separation and fluorescent detection of biomolecules and different cell types.[59-61] Both of the magnetic and the fluorescent parts of the dual mode system will be discussed in details in sections II.1.1 and II.1.2 respectively.

II.1.1 Magnetic nanoparticles

Magnetic iron oxide nanoparticles exist in sixteen different types; however, the three main types, maghemite (α-Fe_2O_3), hematite (γ- Fe_2O_3) and magnetite (Fe_3O_4) nanoparticles are the most commonly used in biomedical applications due to the many advantages they possess.[62,63] First, they can be synthesized in the size of 20 nm or less which is ideal for in vivo applications since the size of a cell is 5-100 μm, a protein is 5-50 nm, a virus is 20-450 nm and that of a gene is 2 nm wide and 1-100 nm long.[41,45] Moreover, these small size nanoparticles can be dispersed inside the cells and will not

precipitate out even under the influence of gravitation forces.[63] Also, iron oxide nanoparticles have a low toxicity and are less prone to oxidation which make them more appealing for biomedical applications than other magnetic materials including nickel and copper.[64,65] Moreover, ferrimagnetic materials exhibit superparamagnetic properties at that size range, this is extremely important for a number of reasons. First; superparamagnetic nanoparticles are responsive to external magnetic fields, which make them ideal for applications such as targeted drug delivery and in biosensing to mention a few.[66,67] Once the external magnetic field is removed, they lose their magnetism due to their zero remnant magnetization, which will prevent the particles from aggregating.[68] Because of the small size of these particles and their large surface area, their surface can be functionalized and tailored to fit certain biomedical applications.[63,69,70] In this dissertation we will focus on functionalization the surface of magnetic particles with a fluorescent probe. The optical part of the dual mode system is discussed next.

II.1.2 Fluorescent biomarkers

The most commonly used biomarkers are fluorescent proteins and organic dyes.[23] Rhodamine and fluorescein derivatives have been used for in vitro fluorescence imaging while near infrared fluorescent dyes such as cyanine fluorescent dye (Cy5.5) have been used in pre-surgical planning in addition to optical imaging.[60,71-74] Organic fluorophores commonly attach to the coating ligand used to functionalize the surface of iron oxide

nanoparticles. For instant, fluorescein isothiocyanate (FITC) was attached to the surface of iron oxide nanoparticles using chitosan as a cross linker for the potential use in bio-imaging of tumor cells.[75]

III. Synthesis and stabilization of iron oxide magnetic nanoparticles

III.1. Overview of nanoparticle formation

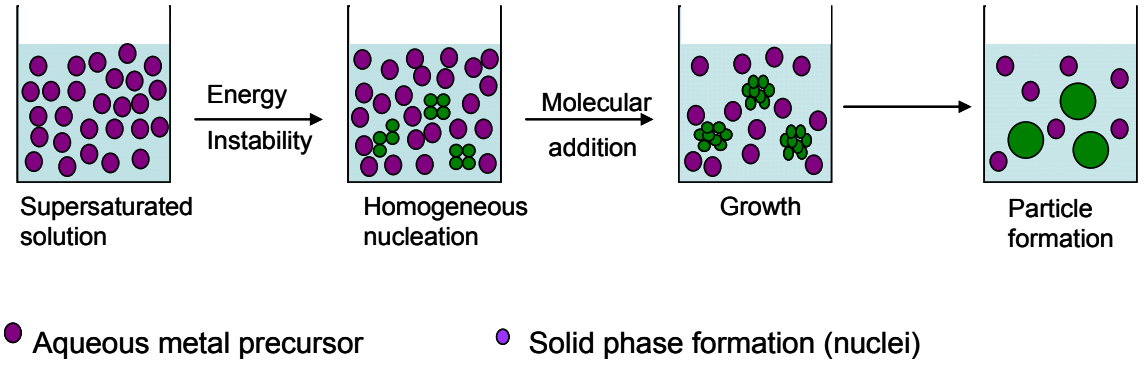

Figure 1-4: Stepwise schematic for nanoparticle formation highlighting nucleation and growth

Even though there are a variety of well known and thoroughly reviewed synthetic methods for nanoparticles, all these methods revolve around two main events; nucleation and growth. [6,39,40] As illustrated in Figure 1-4, when a supersaturated solution is present, its free energy becomes unstable and nucleation occurs. Nucleation is the formation of nuclei in a supersaturated solution; the nucleation process can be either homogeneous or heterogeneous. Homogenous nucleation occurs by combining the solute molecules to produce nuclei in the absence of a solid interface and heterogeneous nucleation occurs in

the presence of a solid interface.[3] Once nuclei are formed, their size increase via molecular addition and this process is called chemical growth which is the second event in nanoparticles synthesis.[3] These two events will change the overall free energy of the solution as described in equation 5:

$$\Delta G = - (4/V) \pi r^3 k_B T \ln(S) + 4\pi r^2 \gamma \qquad (3)$$

where V is the molecular volume of the precipitated solid, r is the radius of the nuclei, k_B is the Boltzmann constant, S is the saturation ratio, T is the temperature and γ is the surface free energy per unit surface area. Equation (3) illustrates the relationship between the free energy and the growth of the particles.[3] Lower free energy is associated with nuclei that are larger than a critical size (r*), which allow their growth to form particles. On the other hand, smaller nuclei than the critical size will dissolve and would not form particles. It is worthy to point out that the nuclei critical size is inversely related to the saturation ratio as demonstrated in Equation (4)

$$r^* = (2V\gamma)/(3k_B T \ln(S)) \qquad (4)$$

the saturation ratio increases as the nuclei critical size decreases and hence, the particle size can be predicted and controlled.[3] Nanoparticles' shape can be controlled by controlling the synthesis parameters; the particle shapes can be manipulated in one, two

and three dimensions to form nanospheres, nanocubes, nanostars and nanorods.[3,36,42-44] The ability to control the nanoparticles size and shape is a significant quality because it allows for synthesizing the nanoparticles to fit the desired applications. In order to obtain nanoparticles with the desired size and morphology, the synthetic route has to be chosen carefully and specifically. The next section provides an overview of the countless ways nanoparticles can be synthesized.

III.2. Synthetic methods for nanoparticles

There are variety of synthetic methods that are used in nanoparticle preparation such as the sol-gel process, reverse micelles, chemical precipitation, hydrothermal synthesis, chemical and physical vapor deposition, and pyrolysis.[8,46,76-81] All these methods are well used procedures for nanoparticles preparation; however, their produced particles differ in the size, morphology, size distribution and properties. In general, the most suitable synthetic methods are the ones offering the control over nucleation and growth. In general, monodispersed nanoparticles can be obtained when the nucleation event occurs separately and the growth takes place at a slower pace.[82] Therefore, our focus will be directed towards the simpler synthetic routes that have certain advantages and qualities and allows for easier control over the nucleation and growth events. We will focus on certain techniques: thermolysis, chemical precipitation and reverse micelles.

III.2.1 Synthesis of nanoparticles using thermolysis

Thermolysis is a synthetic technique in which metallic nanoparticles are produced through the reduction of a metal salt by a certain coordinating solvent while heating. If the solvent was a diol such as ethylene glycol, diethylene glycol and propandiol, this method is often referred to as the polyol process.[45] The liquid polyol is used as the solvent and a reducing agent.[45] The first step of this process after the reactants are added is the hydrolysis of the metal salt dissolved in the polyol and then, the reduction of the metal precursor. Due to reactant addition and the increase in the reaction rate due to heating, the solution becomes supersaturated. Consequently, a short nucleation burst will occur followed by a slow growth of the metallic particles.[31, 45]

The advantages of this process is highlighted by the production of finely dispersed, nonagglomerated metal nanoparticles with well defined morphology, narrow size distribution and high crystillanity.[83,46-49] Obtaining such properties was possible since the polyol methods allows for controlling the nucleation and the growth steps through controlling the temperature, the reactant concentration, the time of the reaction and by avoiding the aggregation of particles during these steps.[45] In this regards, the polyol process precedes many other synthetic routs, especially that the polyol solvent can also act as a productive layer preventing particles' aggregation and passivate them against oxidation.[84]

III.2.2 Synthesis of nanoparticles using aqueous chemical precipitation

Metals, metal oxide, and semiconductor nanoparticles can be synthesized via aqueous precipitation technique. This method outshines the polyol processes in certain parts; it can be done in an aqueous media which is a crucial step if the produced particles are to be used in biomedical application. Aqueous precipitation method can be done at room temperature or under mild heating conditions.[85] Furthermore, it is a one step process in most reactions and, hence, it is a simple technique. In general, the metal precursor is dissolved in distilled water and a simple precipitation agent is added such as sodium hydroxide, ammonium hydroxide or long chain amines.[86,87] Then, the mixture is stirred at room temperature or mild heating conditions under nitrogen gas. The produced particles using this technique have several advantages including narrow size distribution, fast crystalline formation rate, high crystallinity, biocompatibility, complete hysteresis loop.[86,87] On the contrary, these particles are highly aggregated and cross linked which can hinder their dispersion in water. Also, the particle size and morphology is sensitive to pH changes as well as the synthesis time which is longer on average that the polyol process.

III.2.3 Reverse micelles synthesis preparation

Collectively, the two previous methods produce the most suitable particles' properties that are needed for a variety of applications and specifically in biomedicine.

The polyol method generate monodispersed particles that are stable against oxidation and highly magnetic, however, they are synthesized in organic environment and need further modification to disperse in water. The aqueous precipitation method takes place at a milder reaction conditions and produces particles with high crystallinity and biocompatibility. In contrast, these particles are more prone to oxidize and highly aggregate due to the Van der Waals forces and the absence of a capping agent. Some reactions using this technique can take long hours to be completed.

These facts have directed our search towards a technique that could combine the advantages of both routes. Reverse micelles technique was the most fitting candidate to obtain such properties. An overview of normal micelles is an essential component in understanding the concepts and properties of reverse micelles.

Overview of micelles

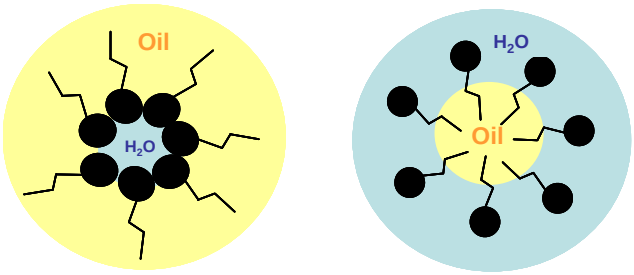

Figure 1-5: Reverse micelles (left) and micelles (right).

Normal micelles or micelles are surfactant aggregates that are dissolved in an organic solvent. Figure 1-5 shows the difference between normal micelles (right) and reverse micelles (left). In general, micelles are surfactant aggregates dissolved in an organic solvent; they are only formed when the concentration of the surfactant exceeds the critical micelles concentration (CMC) in water.[3] In normal micelles the surfactant's hydrophobic tail is directed toward the interior part and the hydrophilic head is directed to the surrounding aqueous media. Alternatively, in reverse micelles, the hydrophilic head of the surfactant is directed towards the interior of the micelles and the hydrophobic tail is directed to the nonaqueous surrounding. Consequently, the aqueous phase can be dissolved in the organic phase producing small aqueous droplets surrounded by surfactant aggregates. These small aqueous droplets are referred to as the "water pool" described as "ω" which represent the water to surfactant molar ratio, and it is one of the factors influencing the size of micelles. In addition to ω, the size of micelles can also be affected by the water content inside the micelles, average number of reactants per micelle, and intermicellar potential.[8,88] The ability to control the particles size by controlling the size of the formed micelles is easier to manage in comparison to other synthetic routes.

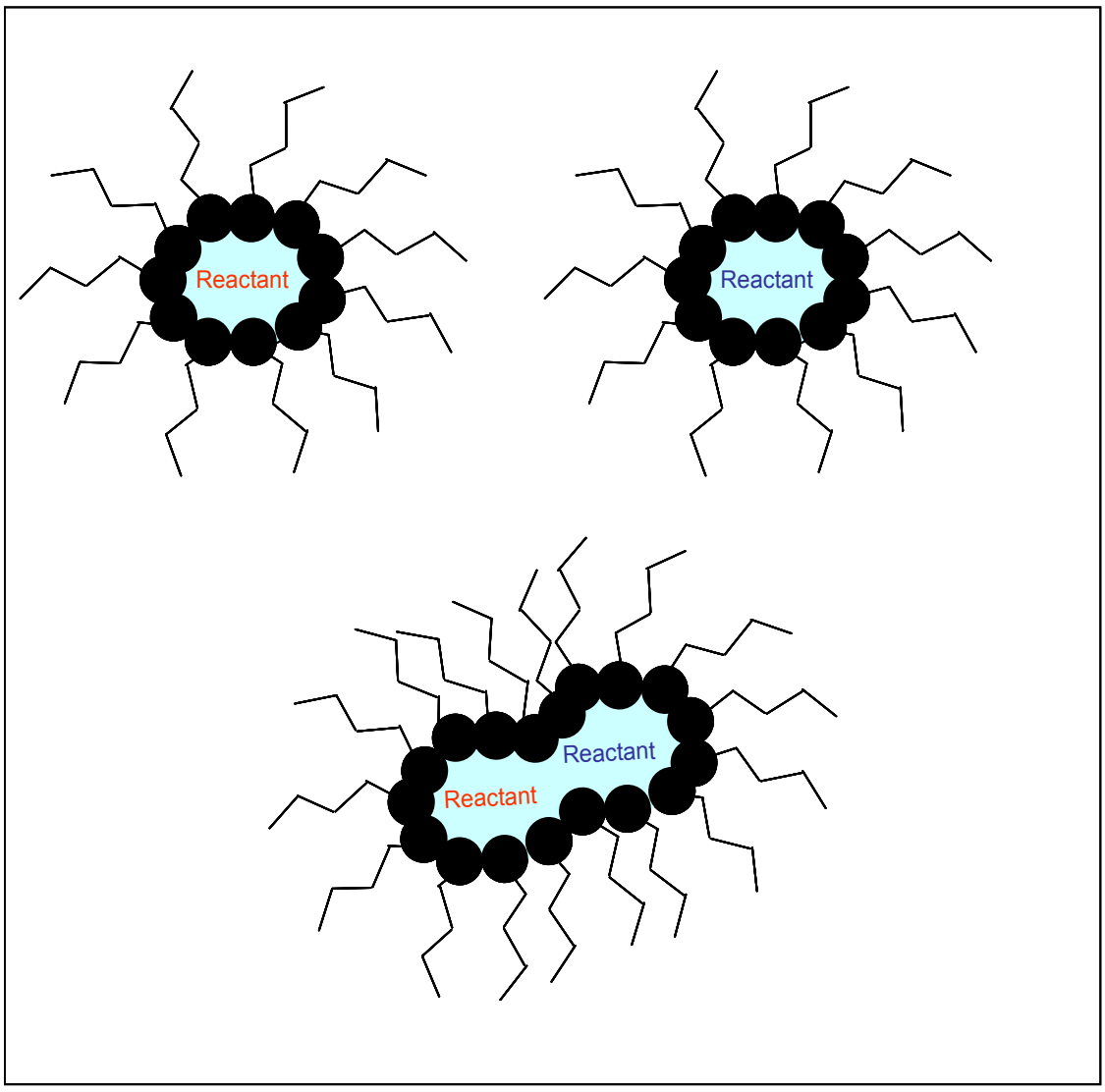

Figure 1-6: Content exchange between two reverse micelles through the formation of short lived dimers

Reverse micelles can also act as nanoreactors inside which, many chemical reactions or co-precipitations can take a place; this happens because of the Brownian motion of these reverse micelles which leads to their continuous collision.[89,90] As shown in Figure 1-6, these micelles can exist as short lived dimmers, during which, they exchange their water content.[90] Yet again, this technique illustrates extraordinarily property of carrying out reaction in reverse micelles in comparison to the bulk solution where flocculation takes place due to the different solubilities of the reactants and products. Also, reverse micelles technique allows for the control of the micelles size distribution, monodispersion occurs when the nucleation and growth steps are strictly separated. Moreover, the geometry of the reverse micelles can also be synthesized through the shape of the surfactant used, entropy and energy terms of the micelles and solvent properties. It was reported by Pileni et al. that the curvature of reverse micelles depends upon the surfactant parameter or the packing parameter which is defined as[90]

$$\upsilon / \sigma l \qquad (5)$$

where υ is the surfactant molecular volume, σ is the area per polar head and l is the length of the hydrophobic part of the surfactant. For spherical particles, the radius of the sphere is stated as

$$R = 3V / \sum \qquad (6)$$

Where R is the radius, V is the volume and $\sum$ is the surface of the sphere.[90] To insure a uniform nanodroplet structure, isolated nucleation sites should be formed simultaneously at large number of positions within the micelles.[81]

Reverse micelles methods possess further advantages beside the ability to control the micelles' size, shape and size distribution. It is also low cost, fast, requires simple equipments and it does not require temperature or pressure control. Though the reaction takes place in aqueous media, the produced particles are not limited to metal oxides but they also include metallic nanoparticles. This is possible because reverse micelles synthesis allows for the formation of core shell morphologies that can passivate the particles and protects them against further oxidation.[91]

IV. Limitations of reverse micelles technique

Since our applications of interest revolve around the field of biomedicine, biocompatibility is a key issue. There are several challenges that need to be overcome before such goal is achieved; these challenges include the fast rate of nanoparticles' oxidation and particles' aggregation. It is worth pointing out that the attachment of a fluorescent probe to the surface of magnetic particles can only take place when the particles are stable and well dispersed. The following sections present the reason behind such limitations along side with the attempts that have been made in an effort to address these issues.

IV.1 Nanoparticles stability against oxidation

Nanoparticles composed of pure metals have high sensitivity to air and they are more prone to oxidation than their bulk counterparts.[92,93] At the nanoscale, metallic nanoparticles are more susceptible to oxidation because they have more surface atoms resulting from their high surface area.[94] The high rate of oxidation of pure metal nanoparticles is a major concern that can limit their use in biomedical applications. Various methods have been applied to passivate these particles against oxidation or at least to slow its rate. The simplest passivation route consist of inducing controlled oxidation of the magnetic core to generate a metal oxide shell around it, The oxide shell protects the metallic core against further oxidation.[94] Controlled oxidation of nanoparticles' surface has been done using different methods. For instance cobalt/ cobalt oxide core/ shell nanoparticles were synthesized by exposing the metal to oxygen plasma or synthetic air while iron/ iron oxide core/ shell nanoparticles have been synthesized using reverse micelle technique.[91,95,96]

Further attempts in this regard included coating metallic nanoparticles with silica, carbon and noble metals.[97-99] For instant, silica coated magnetic nanoparticles were prepared using sol-gel technique to produce stable and uniform particles for the use in magnetic DNA separation.[97] Carbon is used to coat metallic nanoparticles and protect them against oxidation and degradation. Carbon coated metallic nanoparticles are most

commonly synthesized using arc discharge techniques.[98,100] Noble metals are also used as a coating shell around magnetic nanoparticles to prevent their oxidation and corrosion and to enhance their biocompatibility.[101] For instance, coating iron particles with gold to form core shell structures yields highly monodispersed particles with controllable surface capping properties as reported by Wang et al.[101] Moreover, the formation of an noble metal shell over a magnetic core protects the magnetic properties of the core which are essential for the particles' use in high density memory devices.[102] Although the formation of a protective shell around the particles can slow the oxidation rate of the magnetic core, particle aggregation remains a challenge that needs to be solved.

IV.2 Nanoparticle stability against aggregation

The aggregation and agglomeration of metallic nanoparticles in an aqueous medium is an ongoing obstacle in the way of utilizing the particles in biomedical applications. The origin of nanoparticles aggregation stems from the attractive forces originating from Van der Waals, dipolar and magnetic dipolar forces.[103,104] In order to achieve colloidal stability and limit particle aggregation, these attractive forces must be balanced out by repulsive forces such as electrostatic or steric repulsion.[105,106] In order to achieve colloidal stability and limit particle aggregation, these attractive forces must be balanced out by repulsive forces such as electrostatic or steric repulsion.[105,106]

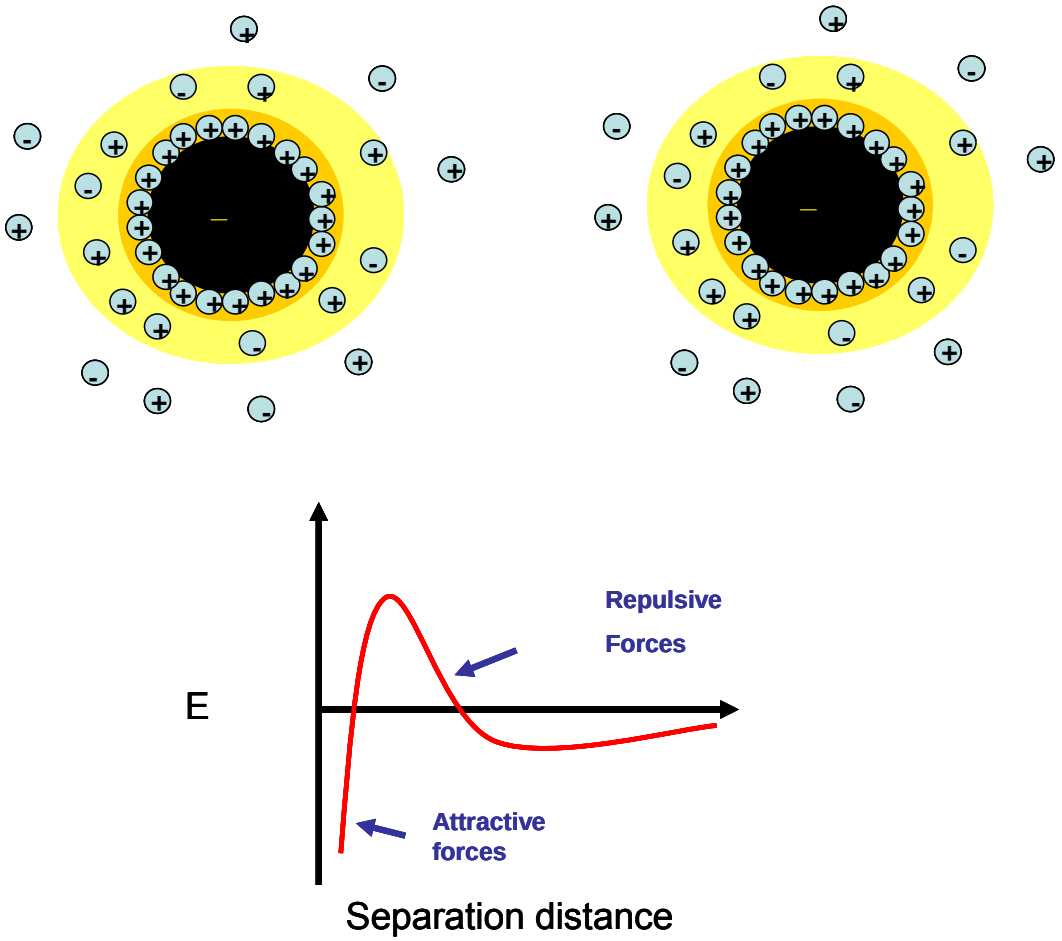

Figure 1-7: The potential energy between particles as a function of their separation distance

Figure 1-7 represents the particles interaction potential energy as a function of the separation distance. There is a certain potential energy barrier that should be overcome in

order for repulsive forces to overpower the attractive forces between the particles at a certain distance.[107]

1V.2.1 Electrostatic repulsion

Electrostatic repulsion is a stabilization method used to counterbalance the Van der Waals forces acting between particles in a colloid by providing counter-ions to neutralize the charges on the particles surface.

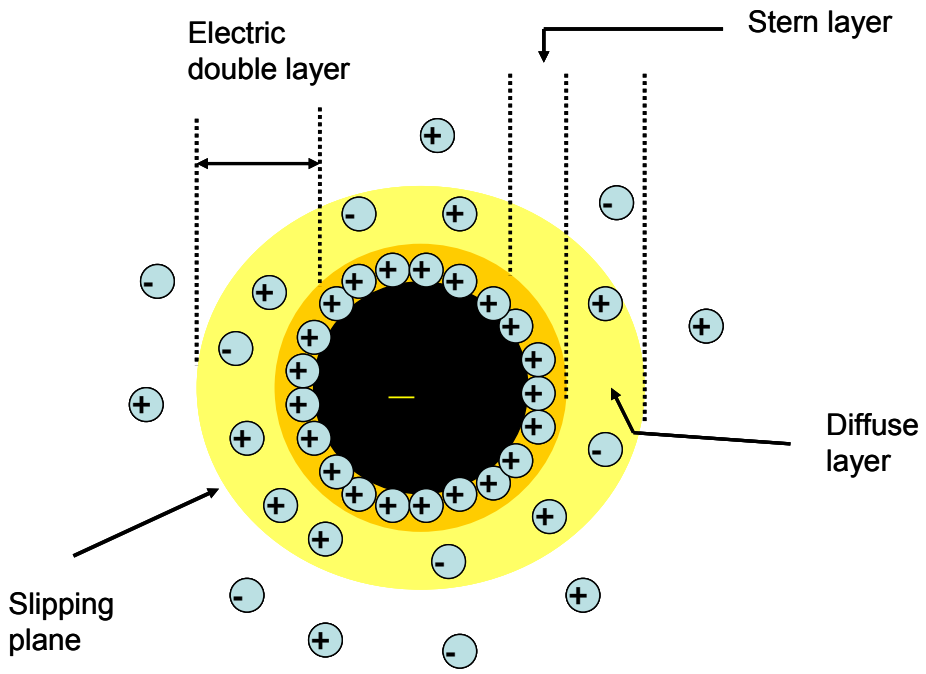

Figure 1-8: Zeta potential

Figure 1-8 represents a negatively charged particle in an aqueous colloid with positively charged ions adsorbed near the surface of the particle via electrostatic interaction. These positive charges form an inner layer near the surface of the particles defined as the stern layer.[108,109] The charges in the stern layer are strongly bonded to the charge on the surface of the particle by columbic forces. The solvent surrounding the particle and the stern layer contains free ions with higher concentration of the counter-ions also attracted to the particle forming a second layer defined as the diffusive layer.[108,109] The double layer containing both the Stern and diffusive layers has an associated electric potential that is the highest near the surface of the particle and decreases as the distance from the particles surface increase. It is important to note that when a particle moves, a layer of the surrounding liquid remain attached to it, the boundary of this layer is called the slipping plane.[110] The charges present in the double layer that contains both the stern and the diffuse layer are separated from the charges in the surrounding liquid by the slipping plane. At this boundary, strongly bond charges (high charge surface) are separated from (weakly bonded charges (low charges). The value of the electric potential at the slipping plan is defined as the Zeta (ζ) potential.[110] Since highly charged surface contribute to a higher stability of magnetic nanoparticles, zeta potential plays a major role in drawing the line between high and low charged surfaces. An arbitrary zeta potential value of 25–30 mV (positive or negative) separate high and low charged surfaces.[110] Adjusting the value of the particles zeta potential by

increasing the surface charges will stabilize the nanoparticles colloid in aqueous media. This can be done either by titrating the colloid with an acid or a base.[110]

1V.2.2 Steric Repulsion

Steric repulsion can be produced by functionalizing metallic nanoparticles with polymers, surfactant or organic ligands. The choice of coating is dependent on the nature of the particle surface and their intended application. Iron oxide nanoparticles synthesized via thermal techniques are covered with organic surfactants such as oleic acid or oleylamine which only allow for their dispersion in organic solvents.[111] This issue can be addressed by coating the surface of the nanoparticles with polymers or surfactants that physically adsorb to the particles surface or chemically anchor to the surface through ligand exchange reaction.[94]

Surfactant addition

Amphiphilic surfactants can render the hydrophobic surface of metallic nanoparticles to a hydrophilic one. The hydrophobic part of the added surfactant will interact with the hydrophobic coating on the surface of the prepared particles through hydrophobic interactions.[112] On the other hand, the hydrophilic part of the surfactant will enable the particles dispersion in water and limit their aggregation.[112] Amphiphilic ligands include poly(maleic anhydride-alt-1-octadecene)-PEG block copolymer, PEG-

phosphlipids, Polystyrene-ploy(acrylic acid) block copolymer (PS-PAA) and tetradecyphosphonate.[113]

Ligand exchange

Particle aggregation can also be resolved by ligand exchange reaction where hydrophobic ligand on the surface of the particles is exchanged with hydrophilic ones. Polymers or ligands with that contains multifunctional groups such as carboxylic acid, phosphates and sulfates enable the attachment of the ligand to the surface of the particles while the remaining unattached functional groups which allow the dispersion of the particles.[94] Such polymers include polyvinyl alcohol and poly(hydroxyethylmethacrylate)[112], ploy(aniline) and poly(lactic acid)[94]. Polyethylene glycol (PEG) and dextran are two of the most commonly used hydrophilic polymers to functionalize the surface of iron oxide nanoparticles owing to their excellent characteristics in biological environment.[94,114] Some these characteristics include stability over time, biocompatibility, availability and anti-biofouling properties which protect the particles' surface against protein adsorption in biological media.[110,115,116] Despite all the exceptional properties for the previously mentioned hydrophilic polymers, there are several drawbacks associated with their use as functionalization ligands. Their large molecular weights increase the hydrodynamic radius of the nanoparticles which can alter their use in *vivo* and affect their magnetic properties.[113]

Researcher started to explore other avenues to find smaller compounds that are stable and biocompatible. Silanes, betaine hydrochloride, 2,3 dimercaptosuccinic acid

(DMSA), organophosphorus coupling agents and dopamine are few examples of small bi- or multi-functional compounds that have been used to coat variety of nanoparticles.[117,118] For instant, DMSA is commercially available and chelates to the surface of FeOx nanoparticles via its carboxylate group forming four membered ring with iron.[119] However, these particles can lose stability upon the oxidation of the thiol to polysulfide.[120, 116] Another common small sized ligand used to functionalize the surface of FeOx particles is organophosphorus compounds such as 4-aminophenyl phosphoric acid and 4-carboxyphenyl phosphonic acid.[117] They are stable due to their easily formed Fe-O-P bond. Nonetheless, coating the particles with such ligand requires multiple and lengthy functionalization steps and specific reaction conditions including high temperatures. Furthermore, organophosphorous precursors are not readily available and have to be synthesized.[117,120]

Dopamine has been used to coat FeOx nanoparticles due to the simplicity of the functionalization steps and the stability of the ligand. FeOx nanoparticles can be functionalized with dopamine via simple aqueous co-precipitation methods.[121] Dopamine chelates to the surface of FeOx nanoparticle through its hydroxide oxygen and forms two strong Fe-O bonds.[121,122] Dopamine creates a five membered ring with the iron on the surface of the particles resulting in a stable coating and reduced steric environment when compared to the four membered ring generated when using DMSA.[123]

Since our goal is to manufacture unique metallic nanoparticles that are stable, monodispersed, have exceptional magnetic and optical properties and disperse in water,

choosing a suitable functionalization ligand and an optical probe is not an easy task. The aspiration of this work is to make outstanding nanoparticles to be used as biomarkers and yet more, to deliver dual performance in some medical applications such as the detection and destruction of cancerous cells in one step. The following chapters contain the journey of several routes that were taken in anticipation to achieve this goal.

Chapter 2: Functionalization of iron oxide/ iron core/shell (Fe@FeOx) nanoparticles with 2-amino-1,3-propane diol (APD)

I. Overview

The use of dopamine to functionalize the surface of iron oxide nanoparticles was discussed in chapter one. Dopamine has distinctive advantages over many other organic ligands, such as its small size, availability, stability and simple functionalization steps.

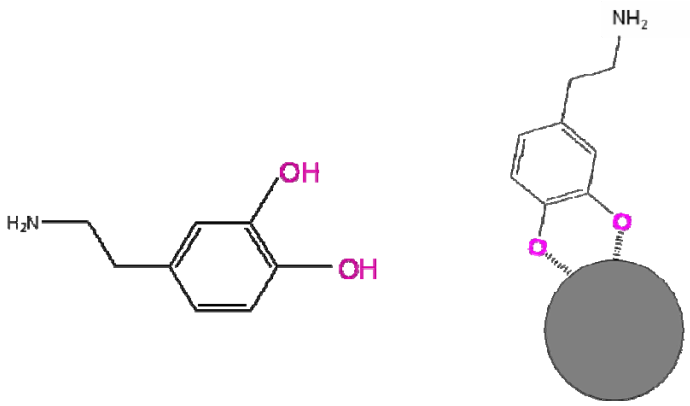

Figure 2-1: Dopamine (left) and dopamine attached to the surface of iron oxide nanoparticles through the formation of two Fe-O bonds (right) forming five membered ring.

It was reported by Xu etal., that dopamine creates a five membered ring with the iron on the surface of the particles resulting in a stable coating and reduced steric environment as shown in Figure 2-1.[122]

In addition, dopamine contains an amino group that can be further functionalized with a fluorescent dye. Therefore, dopamine was our first choice to be used as a functionalization ligand. Once dopamine attaches to the surface of the particle via it hydroxide oxygen, the free amino group remains available for further functionalization with an optical probe.

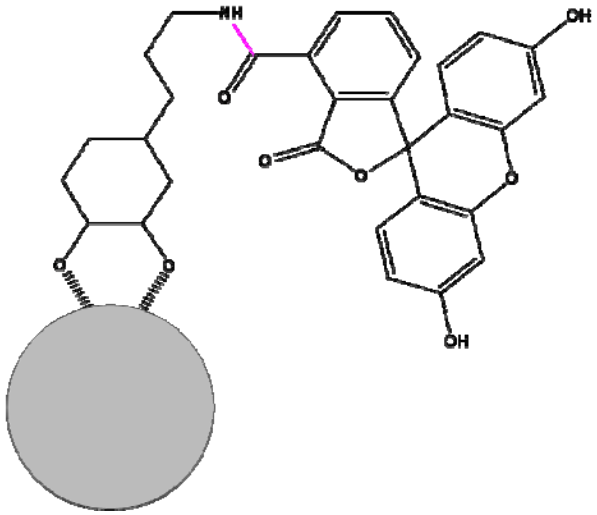

Figure 2-2: Dicarboxyl fluorescein attached to dopamine coated iron oxide nanoparticles through the formation of an amide bond.

Dicarboxylfluorescein was chosen because of its availability and biocompatibility. In addition, one of the carboxyl groups can interact with the amino group of the dopamine to form an amide bond by undergoing an esterification reaction as shown in Figure 2-2. The other carboxyl group allows for the particles dispersion in water. The synthesis of our first dual mode system is presented in section II. Unlike many of the work reported on the use of iron oxide nanoparticles in biomedical applications, we are using iron@ iron oxide (Fe@FeOx) core shell nanoparticles. The presence of a pure metallic core will enhance the superparamagnetic properties of the particles such as the saturation magnetization. The iron oxide shell will protect the core and slow its oxidation rate as it was presented in chapter one.

II. Synthesis of fluorescein – dopamine coated magnetic Fe@FeOx nanoparticles

II.1 Synthesis of Fe@FeOx core-shell nanoparticles

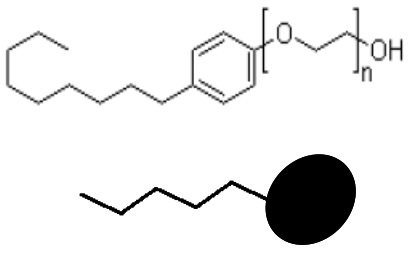

Figure 2-3: Nonylphenoxypoly(ethyleneoxy)ethanols abbreviated as (NP). The "n" represents the number of the ethylenoxy repeating units.

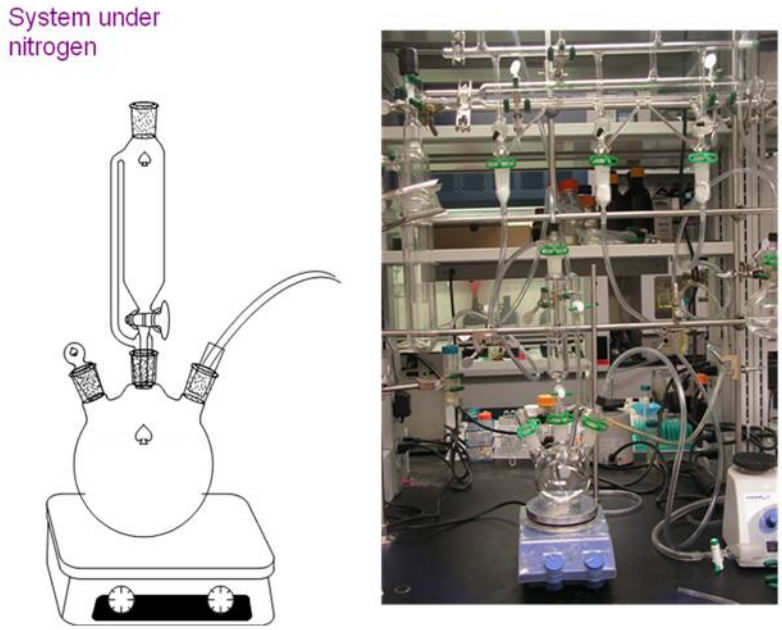

Figure 2-4: Schematic for the reaction set-up (left) picture of the reaction set-up (right). The reaction was carried out in a closed environment under nitrogen to protect the produced particles against oxidation.

Fe@FeOx nanoparticles were synthesized under nitrogen using a previously described reverse micelle technique.[91] The surfactants used for this synthesis were nonylphenoxy poly(ethyleneoxy)ethanols (NP4) for a chain length of four and (NP7) for a chain length of seven receptively (shown in Figure 2-3), while cyclohexane was used as the solvent. The reaction set up is presented in Figure 2-4.

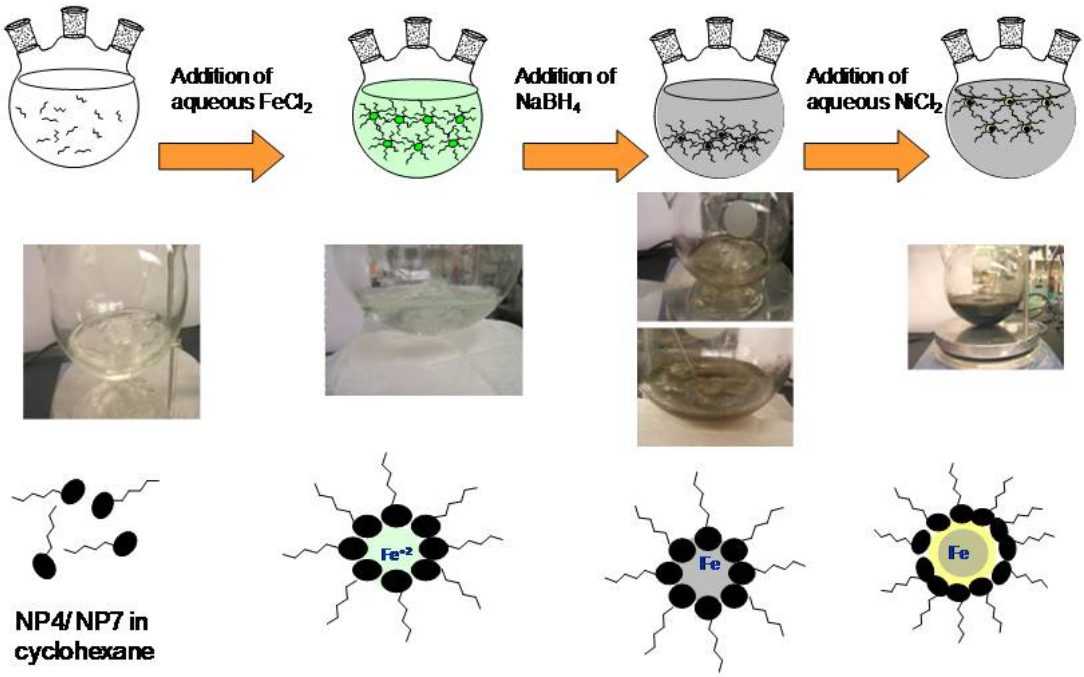

Figure 2-5: Schematic of the reverse micelles synthesis of iron/ iron oxide nanoparticles

Figure 2-5 shows a schematic of the Fe@FeOx synthesis using reverse micelles accompanied with pictures taken during the synthesis. The colorless color of the first surfactant solution presented in the reaction vessel turned green upon the addition of 0.72M of aqueous $FeCl_2$. $4H_2O$. At this point, reverse micelles started to form around the water pool containing the salt. These reverse micelles act as nanoreactors as discussed in chapter one. Then, the Fe (II) cations were reduced using 0.23g of solid $NaBH_4$. In 20 minutes, 0.45M of $NiCl_2$. $6H_2O$was added to the second surfactant solution. The mixture was then transferred into the reaction vessel to enhance the formation of the FeOx shell and to passivate the nanoparticles against further oxidation.

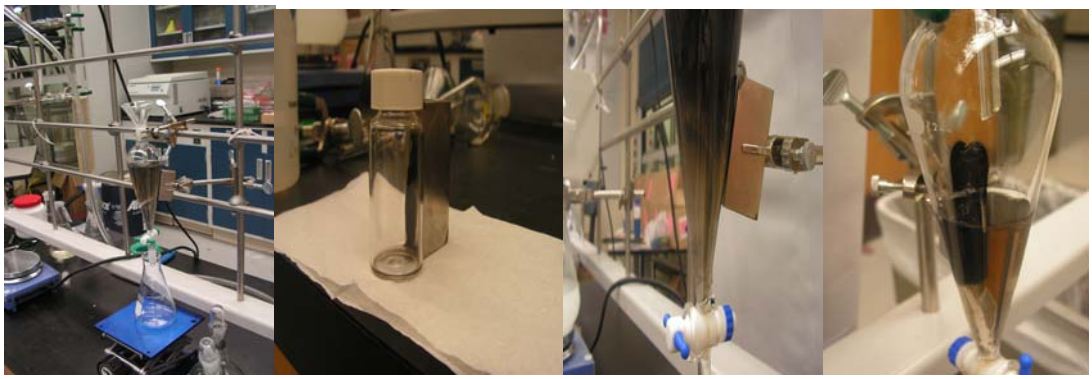

Figure 2-6: Pictures representing the magnetic extraction of iron/ iron oxide nanoparticles. When the reaction is complete, the produced particles in the reaction mixture were transferred into a separation funnel and a magnet was used to separate the magnetic particles from the reaction mixture. After decanting, methanol was used to wash the particles; this process was repeated 4-5 times. After the last wash, the particles were suspended in methanol and transferred into a glass vial before they were magnetically extracted again and left to dry overnight under vacuum.

In 5 minutes, a solution containing 1:1 ratio of methanol and chloroform was used to quench the reaction by disturbing and scattering the previously formed micelles. The resulting Fe@FeOx nanoparticles were washed with methanol to remove excess surfactant and cyclohexane, and then, the resultant particles were collected in methanol by magnetic extraction as presented in Figure 2-6.

II.2 Coating the Fe@FeOx nanoparticles with dopamine and dicarboxyl fluorescein

0.053g of dopamine was added to the collected particles in methanol and the mixture was sonicated until a purple tinge was visible. Dicarboxyl flourescein (0.092g) was introduced to the mixture and followed by 30 minutes of sonication. This process continued until a yellow-orange tinge covered the solution. The coated particles were then washed and dispersed in ethanol and immediately taken to the Cancer Massy Center for cell culturing.

II.3 Imaging of the coated particles inside the human kidney cells

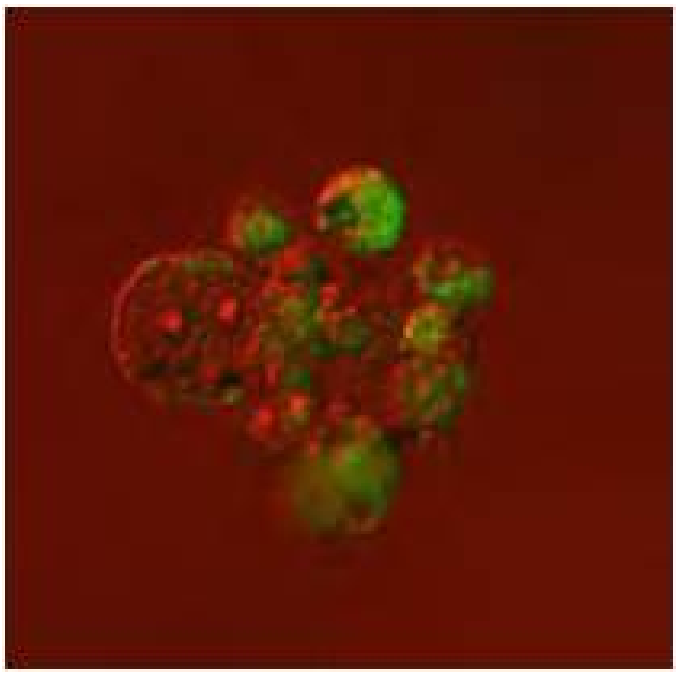

Figure 2-7: Confocal microscopy image of the dopamine– fluorescein coated iron nanoparticles inside U293 cells

Six human kidney cell cultures were prepared; two were control cultures which contained human kidney cells (293), 5 µL of cell media and 200 µL of ethanol. The other four cultures contained 5 µL of media, and 50, 100, 150 and 200 µL of the particles respectively and 150, 100, 50 and 0 µL receptively of ethanol respectively. These cultures were incubated for 2 days and the culture with the largest particle volume (200 µL) was chosen for cell imaging. The cells and the particles were washed and collected in phosphate buffer saline (PBS) and centrifuged at 950 rpm for five minutes. The PBS was decanted The PBS was decanted while the pelleted cells gathered at the bottom of the tube. Saline 90% was added and the mixture was vortexed while cold ethanol was slowly introduced. After incubating for two days, the cells were imaged using confocal microscopy as shown in Figure 2-7. This image illustrates that our coated nanoparticles entered inside the cells. Confocal microscopy is an imaging method that delivers optical resolution and contrast of micrograph images that appears blurry when imaged using a conventional microscope.[124]

Although dopamine has exceptional properties, Shultz et al. established that dopamine itself is reactive towards iron creating cytotoxins. Consequently, the iron oxide nanoparticles degrade to FeOOH resulting in a less stable particles.[123] For that reason, our efforts were directed towards attempting to find a suitable ligand to functionalize the surface of the Fe@FeOx nanoparticles that remains stable over time. In our search we aimed for a stable and biocompatible ligand that minimizes particles aggregation and just like dopamine can be further functionalized with a fluorescent dye.

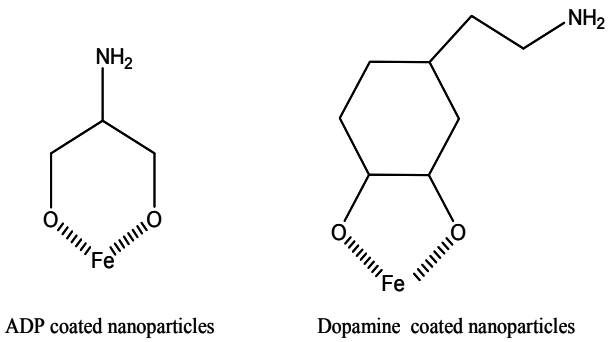

Figure 2-8: six membered ring APD coated nanoparticles (left) and five membered ring dopamine (right)

We introduce 2-amino-1,3-propane diol (APD) as a stable robust coating on the surface of Fe@FeOx nanoparticles. APD is unreactive but can functionalize these particles in the same fashion that dopamine does. Just as in the case of dopamine, the two diol oxygen of APD deprotonate and coordinate to the metal centers as shown in Figure 2-8. In addition APD also contains a free amino group to which dicarboxyl fluroscein could be attached just like the free amine in dopamine.

III. Synthesis of APD coated Fe@FeOx nanoparticles

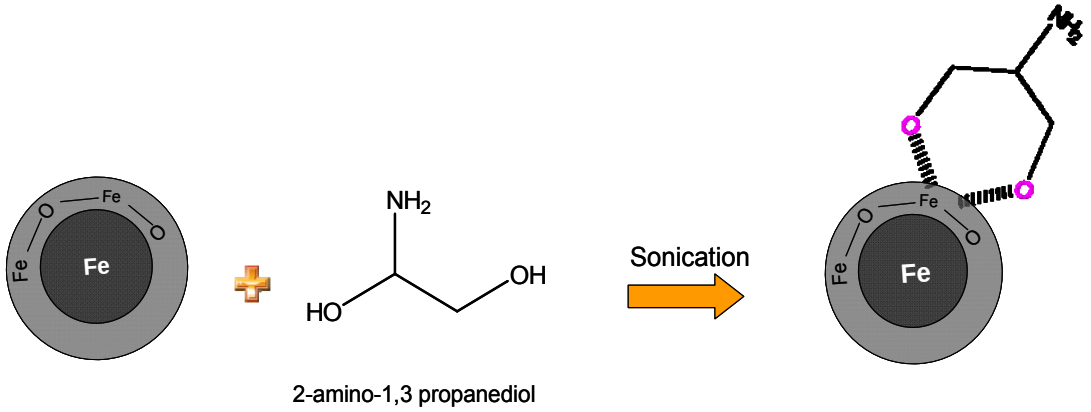

Figure 2-9: Functionalization of Fe@FeOx core shell nanoparticles with APD

The synthesis of the Fe@FeOx nanoparticles via reverse micelles method is the same as described in section II.1. The collected particles in methanol were functionalized with APD by adding 0.033 g of APD to the produced particles suspended in methanol. The mixture was then followed by 30 minutes sonication as shown in Figure 2-9. Then the coated particles were magnetically extracted and left to dry overnight under vacuum.

IV. Experimental section

The APD coated iron oxide nanoparticles were characterized using variety of analytical techniques including transmission electron microscopy (TEM), X-ray photon spectroscopy (XPS), Infrared (IR) and absorption spectroscopy (UV-Vis) and Matrix-assisted laser desorption/ionization / time of flight (MALDI/TOF) spectroscopy. The magnetic properties were measured using vibrating sample magnetometer (VSM).

The size, dispersion and morphology of the coated particles were determined using JEOL CM120 Transmission Electron Microscope (TEM) fitted with a Gatan digital camera. TEM uses high energy (>100 kv) electrons to interact with the sample instead of photons that are used in the optical microscope. This feature is of a great importance when characterizing a sample at the nanoscale because it allows for high resolution imaging down to 0.2 nm while an optical microscope provide a resolution of few tenth of micrometer. In addition, electromagnetic lenses are used instead of light lenses in TEM to deliver higher resolution images.

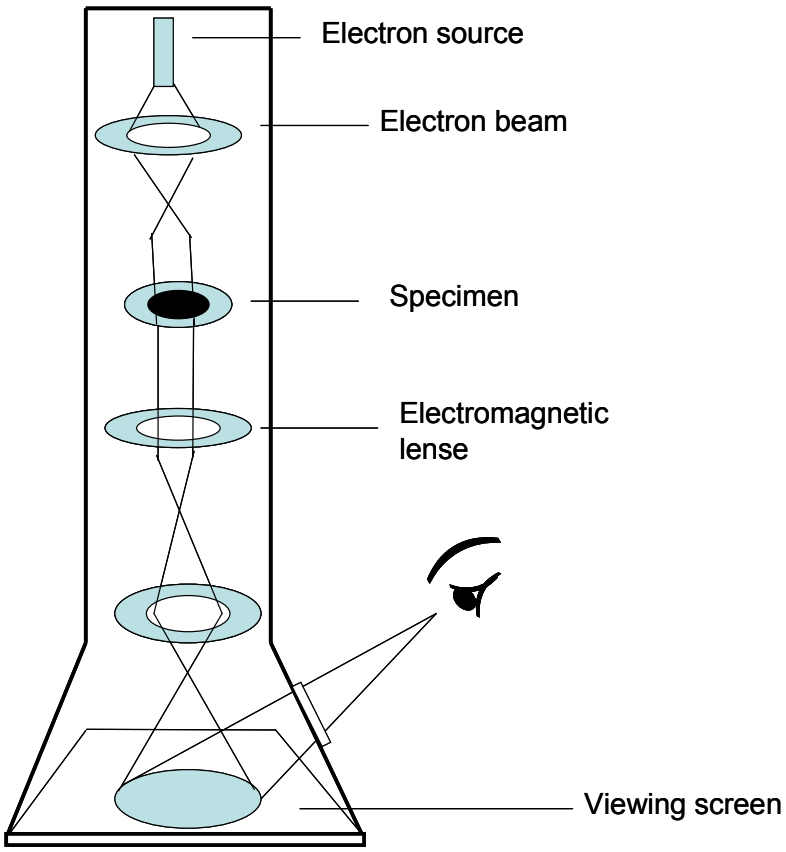

Figure 2-10: Schematic of main components of TEM. Electron beam passes through an electron transparent sample (specimen). The images are magnified using a set of electromagnetic lenses and then projected on a charged coupled device (CCD).

Figure 2-10 shows a schematic of the main components of the transmission electron microscope. The images are acquired when an electron beam passes through an electron transparent sample (specimen).[125] The images are magnified using a set of electromagnetic lenses and then projected on a charged coupled device (CCD) camera, which is an equipment that converts optical brightness into electrical amplitude signals and then reproduce the image using the electric signals.[126]

The core-shell morphology of the APD coated FeOx nanoparticles are represented in the TEM image by dark and grey areas. This contrast in color is due to the interaction of the electron beam with sample. Upon the interaction of the electron beam with the sample, the dark regions represent the core because it constitutes of heavier and denser element which is metallic iron. On the other hand, the FeOx shell is represented by the grey hallow around the dark center because it is less dense when compared to the core. The TEM samples were prepared by dispersing the coated particles in methanol, then delivering 9 μL of the suspension to the TEM grid, after the sample air dries, the grid is placed in the sample compartment of the microscope and the images are obtained as described above.

Infra-red (IR) spectra were obtained using a Nicolet Nexus 670 FT-IR with a KBr beam splitter. IR spectroscopy measures the vibrational frequencies resulting from the absorbance of radiation. Since Infra-red radiation has a low energy, it only allows for atomic vibrations upon the absorption of light. For this work the IR spectra of Fe@FeOx nanoparticles, APD and APD coated Fe@FeOx nanoparticles were obtained. The samples were prepared by combining them with potassium bromide, and then grinding until uniform. Then these samples are pressed into transparent pellets. Infrared spectroscopy data is beneficial because it provides information about the functional groups present in a certain compound. Since the vibrational frequencies of atoms are dependent on their dipole moment, we are able to obtain information about the electronic environment of certain atoms has changed when reactions take place. For example, comparing the IR spectrum of the APD coated nanoparticles to the free APD ligand and the uncoated nanoparticles, the shift in the vibrational frequencies of the same functional group present in the three different spectra, will serve as an indication of the attachment of the ligand to surface of the particles.

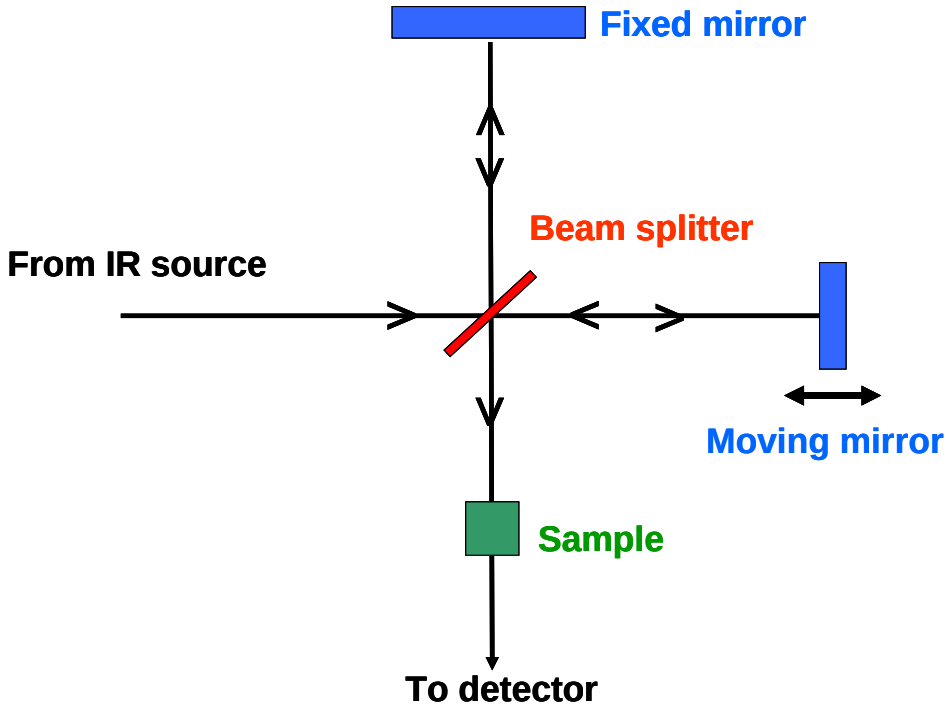

Figure 2-11: Schematic of the main components of the IR spectrometer. The light beam passes first through a beam splitter which separates it into two beams. One will reflect from a fixed mirror and the other will reflect from a moving mirror. The two beams combine at the beam splitter again and are directed towards the sample. The frequencies of energy that are specific and characteristics of the sample being measured are absorbed. Finally the beam passes through the detectors for final measurements.

As shown in Figure 2-11, the beam from the light source pass first through a beam splitter which separate it into two beams. One will reflect from a fixed mirror in place and the other will reflect from a moving mirror.[127] The two beams combine at the beam splitter again and are directed towards the sample and it is either transmitted through or reflected off of the sample.[127] The specific frequencies that are specific and characteristics of the sample being measured are absorbed. Finally the beam passes through the detectors for final measurements.[127]

Matrix-assisted laser desorption ionization/ time of flight (MALDI/TOF) techniques was used to further characterize the surface of the APD coated nanoparticles. MALDI/TOF is a sensitive mass spectroscopy technique that is used to measure the mass to charge ratio of the ionized fragments of the sample of interest. For the purposes of this work, MALDI is used to confirm the attachment of APD to the surface of the particle by providing the mass to charge ratio of the coated particles, the free ligand and the uncoated particles. Matrix is commonly used when performing measurements using MALD. The role of the matrix is to absorb most of the ultraviolet (UV) light in order to prevent unwanted fragmentation of the sample.

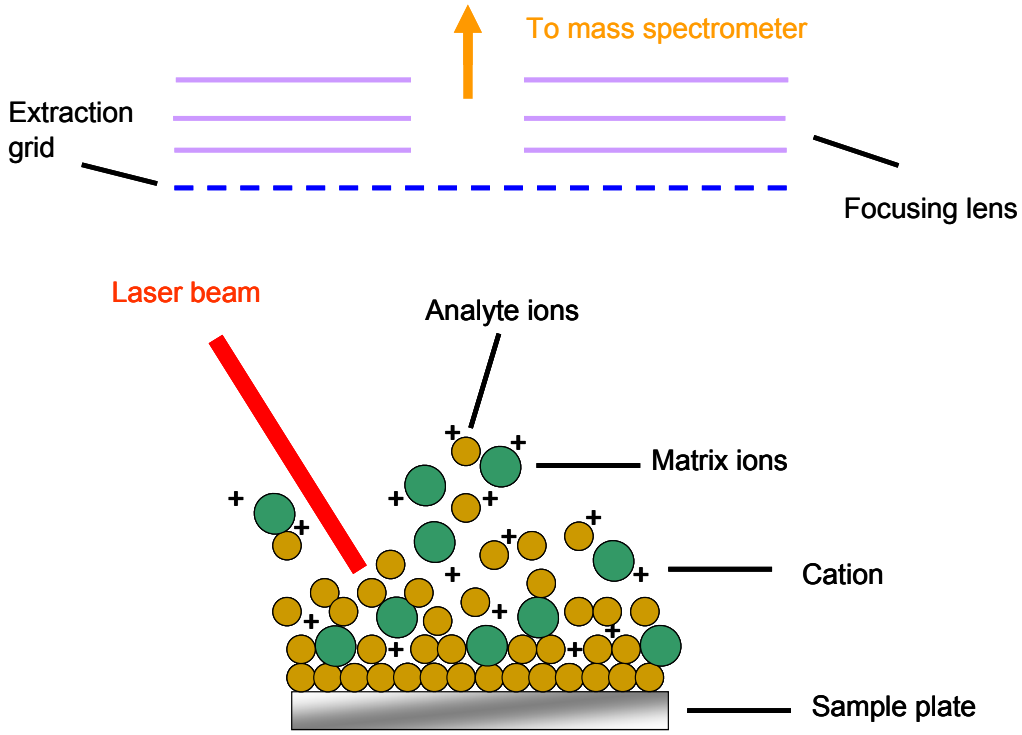

Figure 2-12: matrix molecules absorb energy, they are ionized and they transfer the energy to the sample molecules resulting in their ionization as well. The charged ions are accelerated towards the flight tube (mass spectrometer) by applying an electric field where the larger ions will move slower than the smaller ions, so ions of different masses will reach the detector at different times

Figure 2-12 shows that as the matrix molecules absorb energy, they are ionized and they transfer the energy to the sample molecules resulting in their ionization as well. The charged ions are accelerated towards the flight tube (mass spectrometer) by applying an electric field where the larger ions will move slower than the smaller ions, so ions of different masses will reach the detector at different times. As the laser beam hit the APD coated nanoparticles, the outermost layer of the particles surface will be ionized and the detector measures the different fragments as each layer is ionized. Since APD is present on the surface of the particle, the signal from APD should disappear as the inner layer of the coated particles are ionized.

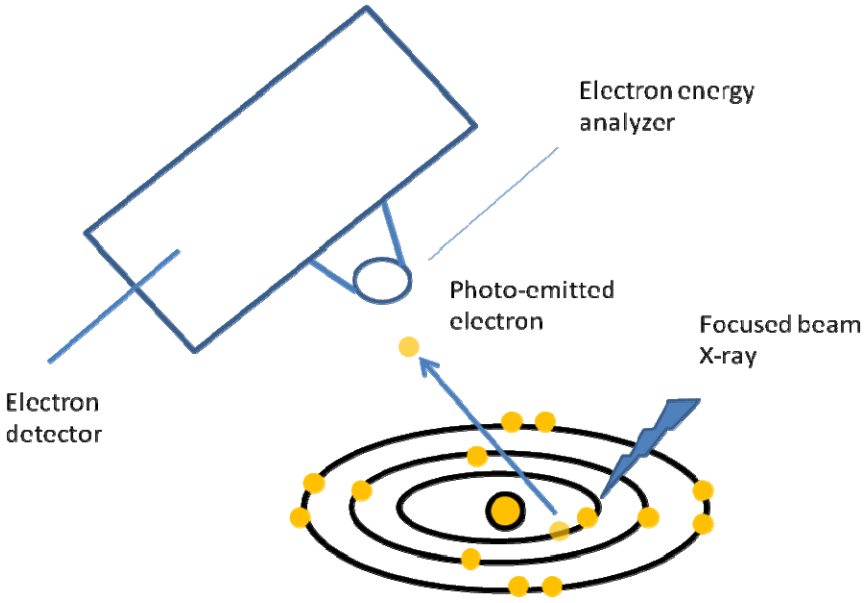

Figure 2-13: Schematic showing the mechanism of measuring the kinetic energy of the emitted photoelectrons

X-ray photoelectron spectroscopy (XPS) is an analytical technique commonly used to analyze the chemical composition of materials' surfaces. As the sample of interest is irritated using X-ray beam, a core electron is ejected and it is defined as a photoelectron as shown in Figure 2-13.[128] The number of electrons escaping from the top 1-5 nm of the material of interest is measured as well as their kinetic energy. XPS provides information about the binding energy of the ejected electrons by subtracting the kinetic energy (KE) of these electrons from the energy of the X-ray source (hv).[128] The binding energy and the chemical shifts in the collected XPS data is dependant on the chemical environment surrounding the elements of interest.[128] When an X-ray beam interacts with a core electron, total energy transfer takes a place and the electron is emitted as a photoelectron. The energy needed to eject an electron is defined as the

binding energy and it is specific to the type of atom and its environment.[128] The ejected electron will pass through electron energy analyzer and then the electron detector.

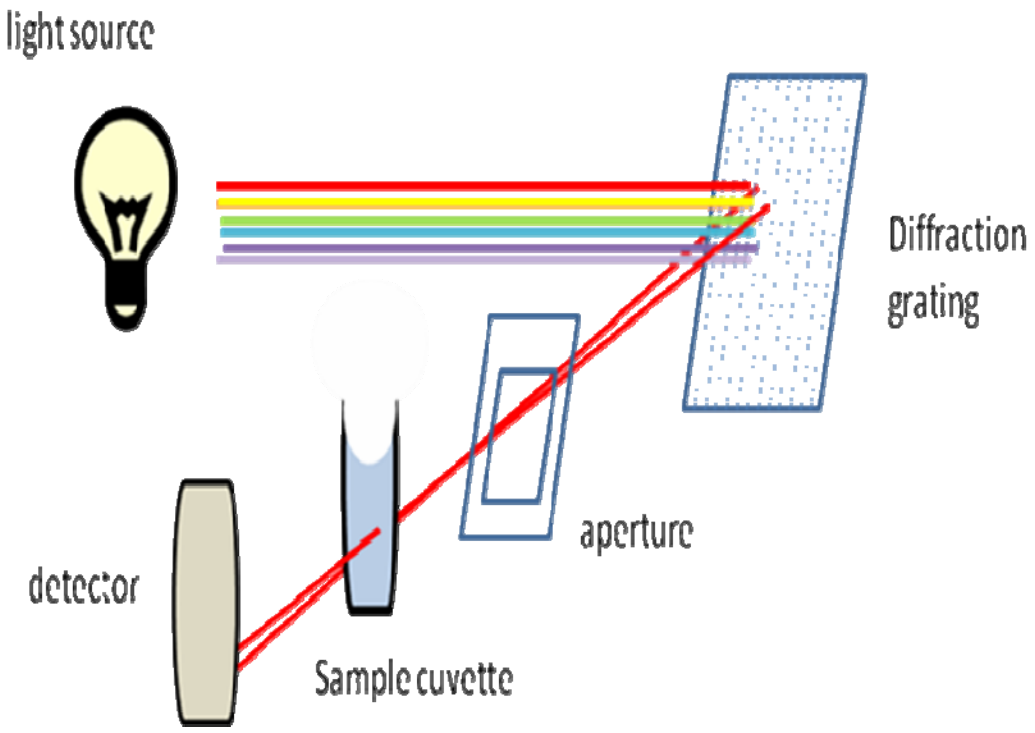

Figure 2-14: Schematic showing the main components of the UV-vis spectrophotometer. The visible light passes through the diffraction grating where the light is diffracted in different directions depending on the wavelength of light and the spacing of the grating. Then the light beam travels through the aperture, which is an opening that determines the cone angle of the light rays that comes to focus in the image plane. Finally the light passes through the sample before the materials absorption is detected.

Ultraviolet-visible (UV-vis) spectroscopy is used to measure the materials'

absorption in both the visible and ultraviolet region. This characterization method is used to measure the electronic transition from the ground state to the excited state of a certain sample after irradiating it with light with a wavelength that falls in the visible or the ultraviolet region of the electromagnetic spectrum. The electronic transition can be presented by one of these processes: σ to σ*, which is present in compounds containing single bonds. π to π*, which takes place in compounds that contain double bonds. n to σ* and π to π* transitions which happens in compounds containing lone-pair of electrons and a single or a double bond respectively. Also, d-d or f-f transitions which take place between a ground and an excited state of the d and f orbitals respectively. Finally, electronic transition can also happen in compounds that contain a mixed valence oxidation states of the same metal or different metals, Prussian blue for instance, has both Fe(II) and Fe(III) cations. This type of electronic transition is defined as a charge transfer process. Figure 2-14 shows the visible light passing through the diffraction grating where the light in different directions depending on the wavelength of light and the spacing of the grating. Then the light beam travels through the aperture, which is an opening that determines the cone angle of the light rays that comes to focus in the image plane. Finally the light passes through the sample before the materials absorption is detected.

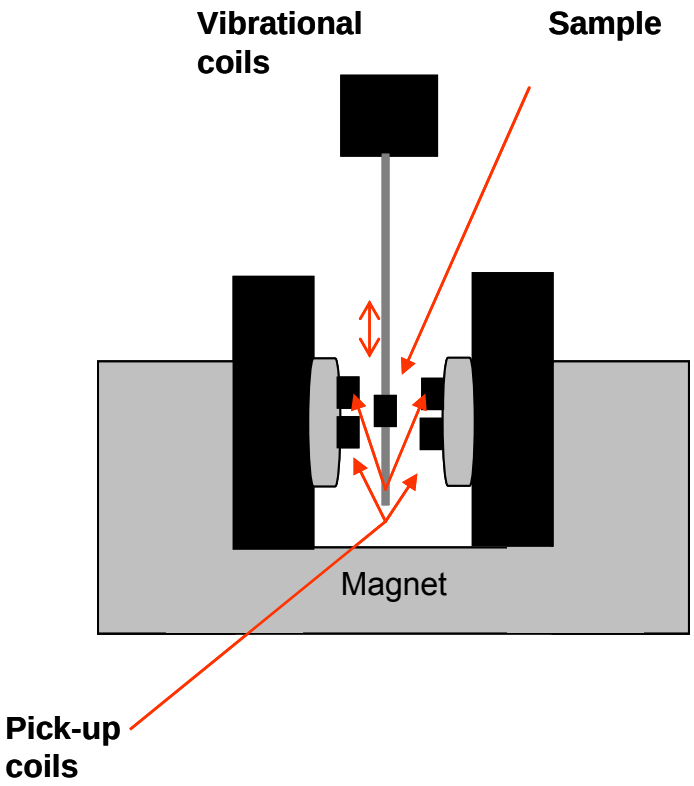

Figure 2-15: Schematic showing the main components of VSM . When an alternating magnetic field is applied, an electric field is produced in the pick up-coils. The produced current will then be amplified and using a computer interface, information about the magnetization of the sample and its dependence on the magnetic field could be obtained

Vibrating sample magnetometer (VSM) measures the magnetization of the magnetic material as a function of applied field's strength. VSM measurements are based on Faraday's law of induction which states that the change in the magnetic field will produce an electric field. Measuring the resulting electric field provides information about the changing magnetic field. As shown in Figure 2-15, when an alternating magnetic field is applied, an electric field is produced in the pick up-coil. It is worth noting that the greater the magnetization of the sample, the greater the induced current

will be. The produced current will be amplified and then using a computer interface that contains a specific software system, information about the magnetization of the sample and its dependence on the magnetic field could be obtained.[129]

V. Results and discussion

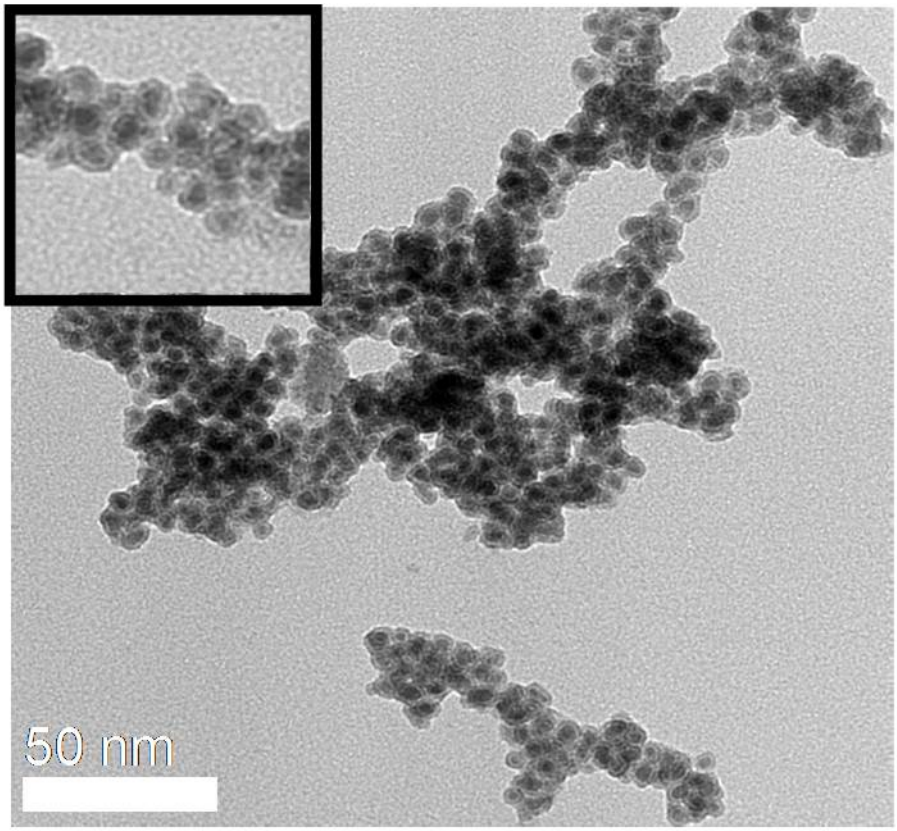

Figure 2-16: Transmission electron microscopy (TEM) image of APD coated FeOx nanoparticles

Figure 2-16 shows the TEM image of the APD coated Fe@FeOx nanoparticles. The image represents well defined core shell nanostructures with a size distribution in the range of 8 to 13 nm. The inner dark centers represent the metallic iron core and the outer light color rings represent the iron oxide shell. These results indicate that iron core shell nanoparticles are present.

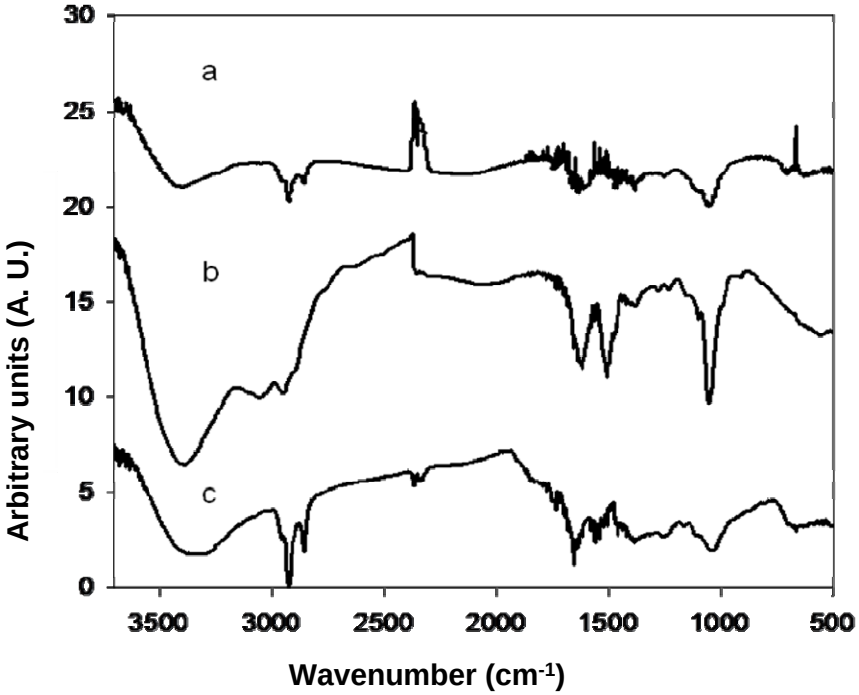

Figure 2-17: Fe@FeOx nanoparticles (a), APD coating (b) and APD coated Fe@FeOx nanoparticles (c). The shift in the OH stretch from 3430 cm^{-1} (a) to a lower energy at 3369 cm^{-1}(c) is indicative of the chelation of the hydroxyl oxygen of the APD to the surface of the particles

Figure 2-17 represent the Infrared spectra of the uncoated particles (a) as well as the APD coated particles (c) and the free APD coating (b). The transmission spectra of uncoated Fe@FeOx nanoparticles (a) reflect OH stretching and HOH bending at 3430 cm^{-1} and 1630 cm^{-1} respectively. These vibrational bands are characteristic of FeOx nanoparticles. The presence of FeOx nanoparticles was confirmed by the metal- oxygen stretching bands that fall in the transmission range of 580-620 cm^{-1}.[130] Figure 2-17 (c) represents a shift in the OH stretch from 3430 cm^{-1} (a) to a lower energy at 3369 cm^{-1}. This shift could be attributed to the interaction between the hydroxyl groups of APD with the iron in the FeOx shell. Figure 2-17 (c) also shows a broadening in the OH stretch which is indicative of the presence of an amino group on the surface of the particles since the vibration frequency of primary amines is at 3285 cm^{-1}.[131] The bands at 1662 cm^{-1} and 1556 cm^{-1} in the IR spectrum of the APD coated nanoparticles represent 1^0 amine and C-H bands coming from the APD as shown for Figure 2-17 (c). The peaks around 2340-2370 cm^{-1} in (a) and (c) are specific to the carbon dioxide band while peaks around 2930-2860 cm^{-1} for all three spectra are specific to alkanes and alkenes which come from the residual surfactant attached to the particles surface. Finally the peak around 1060 cm^{-1} in all three spectra are attributed to either the C-O stretch or the C-N stretch.

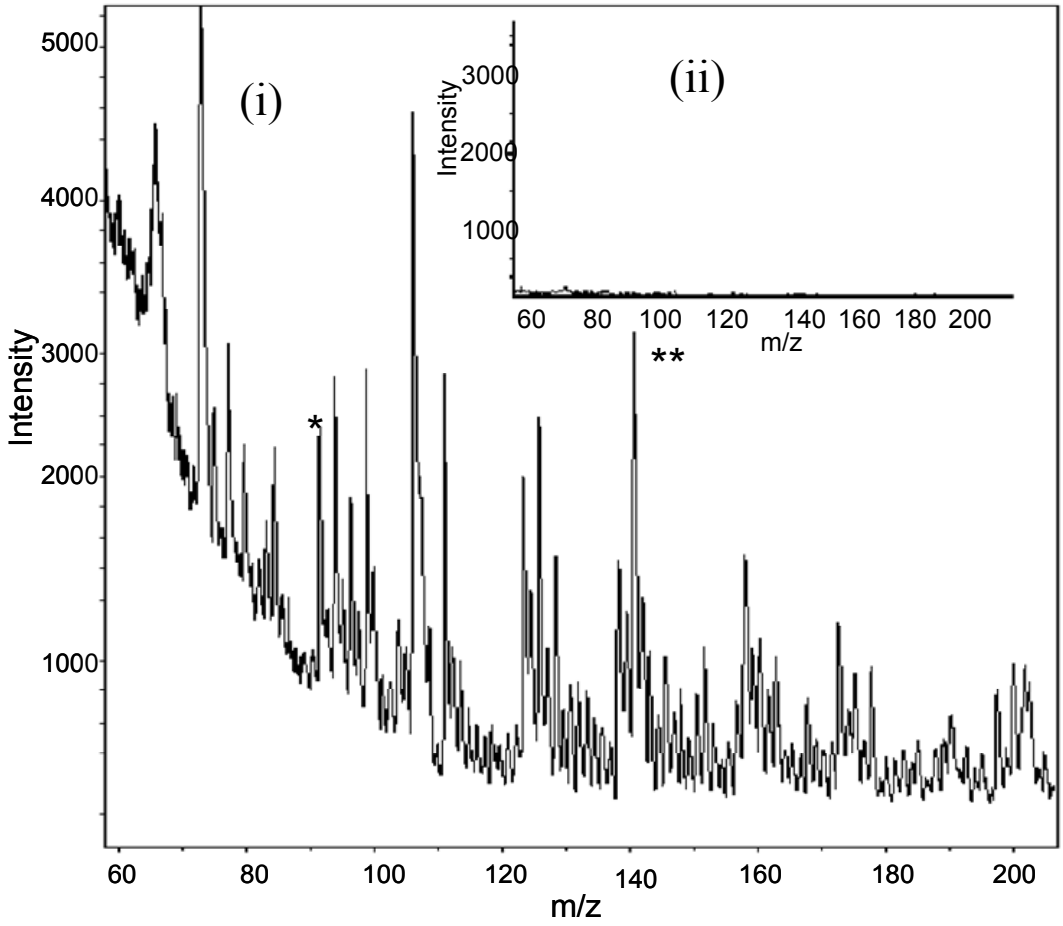

Figure 2-18: (i) First analysis of MALDI spectrum for the coated Fe-Ox, * and ** indicate m/z 91 and m/z 143 respectively. **(ii)** Hundredth analysis for MALDI spectrum for coated Fe-Ox, m/z 91 and m/z 143 are no longer present.

To further characterize the attachment of APD to the surface of the magnetic nanoparticles, a depth profiling experiment were conducted. The addition of matrix to the nanoparticles does not enhance their response to MALDI/TOF analysis, so no matrix was used.[132] Figure 2-18 compares the data collected from the from the first laser shot of

the outermost layer of the nanoparticles to the last laser shot of the depth profiling experiment. In the data from the outermost layer, the peaks at m/z 91 and m/z 143 represent free APD and APD coated FeOx, respectively. As layers are removed, these ions gradually reduce in intensity until they are no longer present (Figure 2-18(ii)). This is yet another indication of the presence of the APD ligand on the nanoparticles surface.

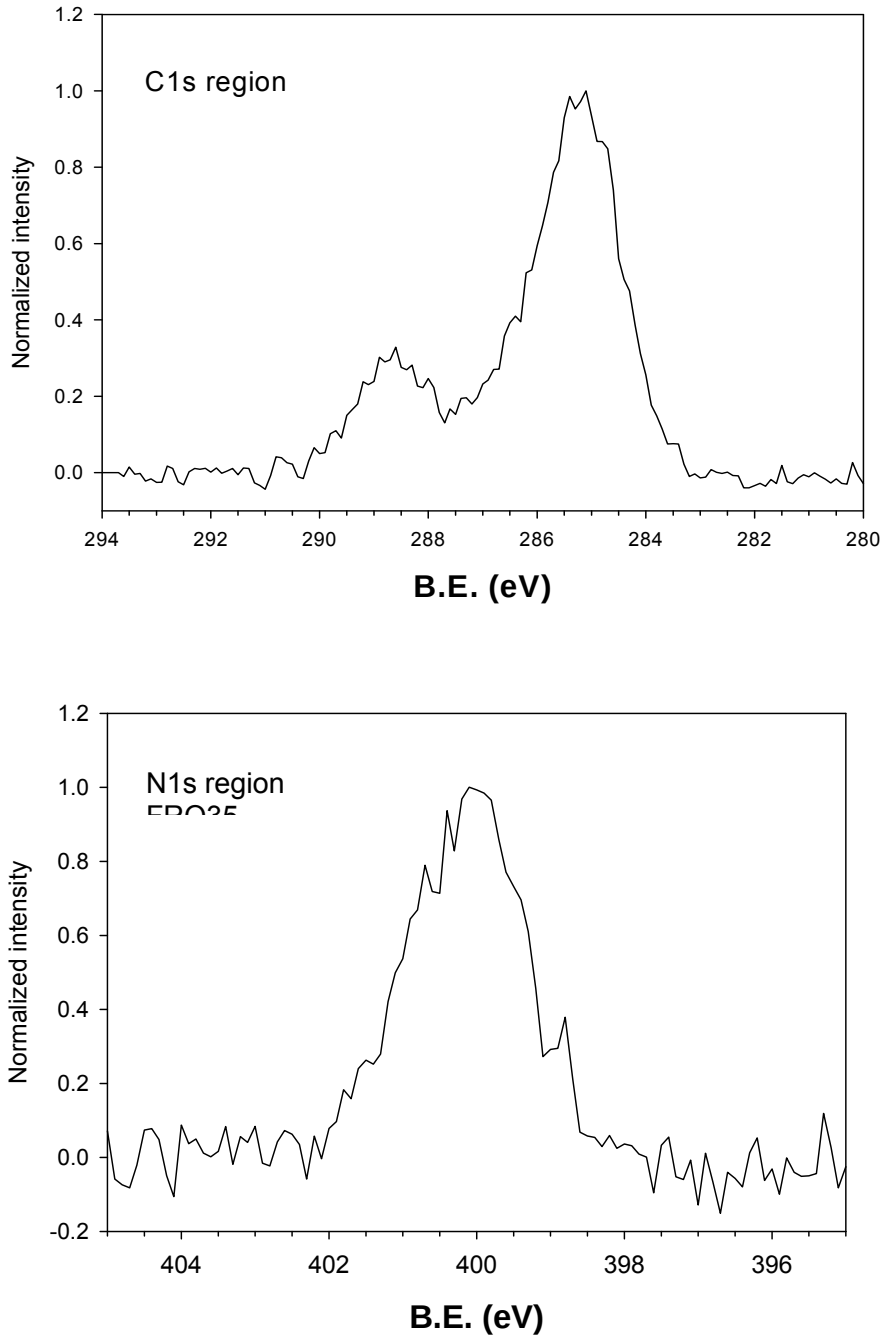

Figure 2-19: XPS spectrum of the C1s and N1s regions of the APD coated nanoparticles. Peaks at 285 eV and 288.5 eV in the C1s regional scan are attributed to C-C and the C=O single bond respectively. The peak at 400 eV in the N1s regional scan is consistent with APD

X-ray photoelectron spectroscopy was used to analyze the surface of the nanoparticles (Figure 2-19). The nanoparticles were placed on indium foil to obtain a thin deposit and then placed onto a sample holder. The C1s region scan (Figure 2-19) shows two peaks at 285 eV and 288.5 eV, which are both attributed to C-C and the C=O single bond respectively which are present on the particles' surface. The C-C can come from either the APD or the residual NP surfactant while the C=O comes from the surfactant. The C-N bond as described by Tao, is unlikely due to a carbon bonded to the FeOx surface, therefore it is most likely from the APD itself.[133] The N1s region scan shows one peak at 400 eV, which is consistent with free APD and attributed to the N-H binding energy.

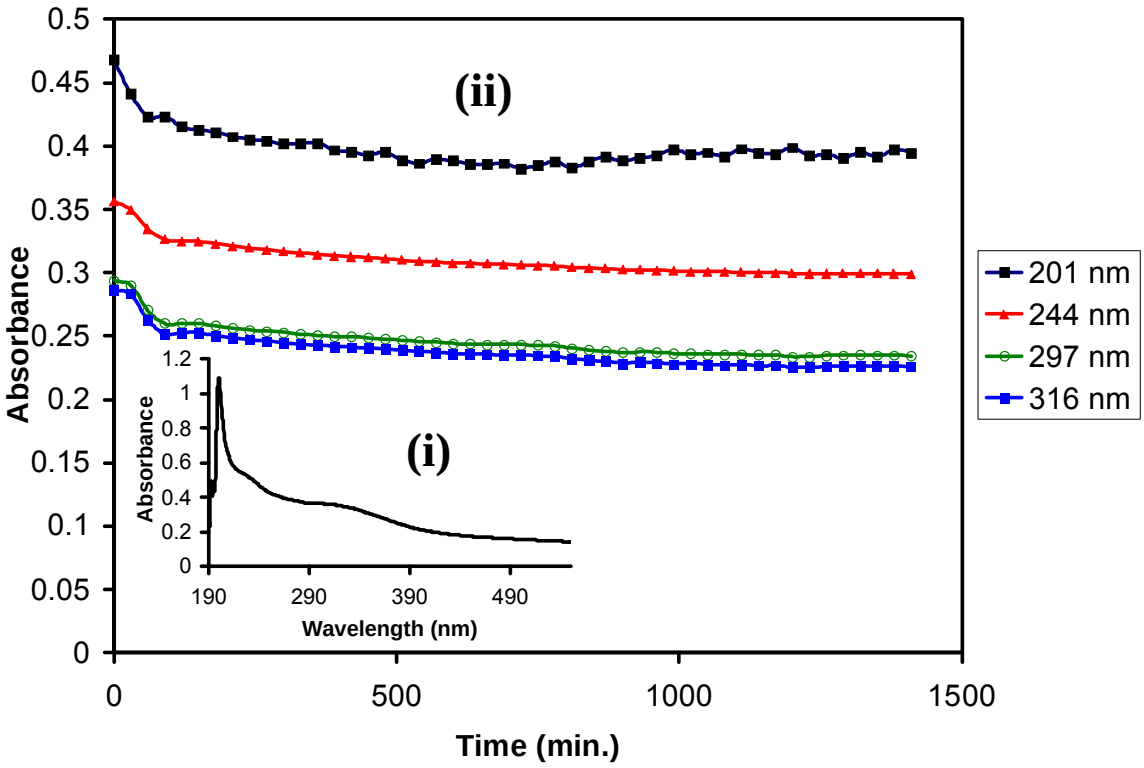

Figure 2-20: (i) UV-VIS absorbance spectrum of coated FeOx with 2-amino-1,3 propane diol (ii) Kinetics run for the coated FeOx nanoparticles over 24 hours

The stability of the coated nanoparticles over time was shown using UV-vis spectroscopy. Figure 2-20(i) shows the absorbance peaks of free APD and Figure 2-20 (ii) shows a kinetic plot of the APD coated nanoparticles using the absorbance peaks from (i) at 201, 244, 297 and 316 nm and they were plotted as a function of time. The samples for (i) and (ii) were prepared by dissolving about 1 mg of APD in 2-3 ml of methanol and 1 mg of the coated particles in 2-3 ml of methanol respectively. Quartz

cuvettes were used to measure the absorbance of the suspension. The kinetics run indicates that there was an initial change in the absorbance of the coated particles which could be attributed to the reaction of small amount of the coating with the iron present at the surface. However, after that initial point, no changes have occurred on the APD coated nanoparticles over 24 hours period.

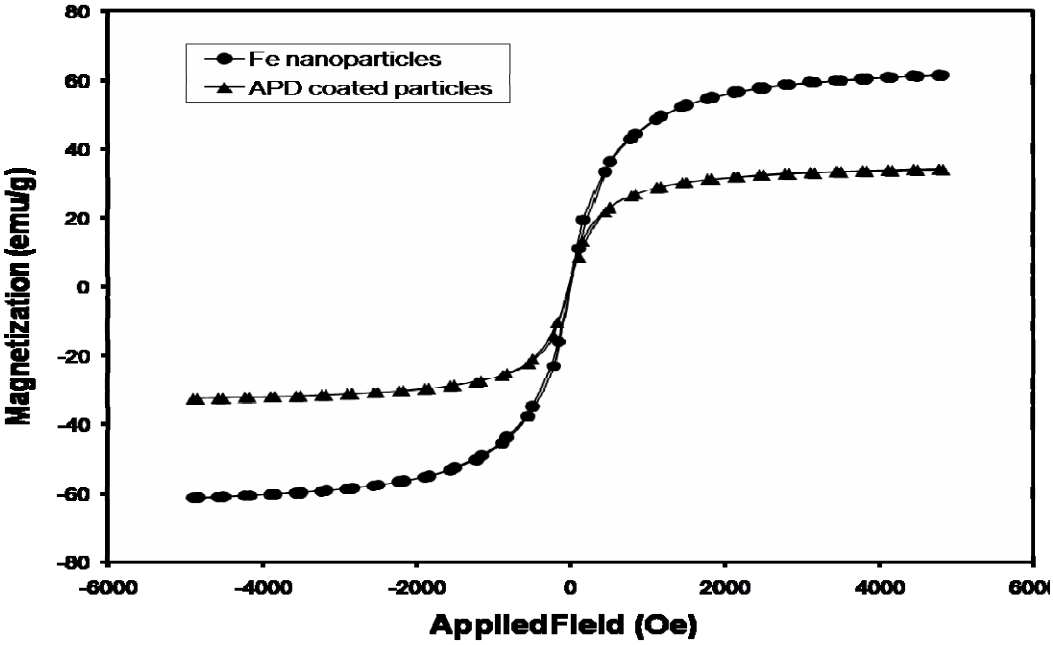

Figure 2-21: VSM spectrum of the uncoated nanoparticles and the APD coated nanoparticles. Before the particles were functionalized, the magnetization saturation reached 60 emu/g. However, after functionalization with APD, the magnetization dropped to 33 emu/ g.

The Vibrating sample magnetometer (VSM) data shown in Figure 2-21 presents the magnetization of the coated particles at room temperature. The magnetization of the unfuntionalized particles was 60 emu/g which is considered high since bulk magnetite has a magnetization saturation range of 92-100 emu/ g.[134] However, after functionalization the magnetization became 33 emu/g. The slight reduction magnetization was a result of the surface coating of APD.

VI. Conclusions

In conclusion, we have used APD as a robust anchor to functionalize our Fe@FeOx nanoparticles. The APD coated nanoparticles have been characterized using variety of methods to verify the attachment of APD to the surface of these particles. These methods included TEM, IR, XPS, MALDI/TOF, UV-vis and VSM, all of which collectively indicated the presence of APD on the surface of the nanoparticles. APD coated particles showed stability over 24 hours while maintaining their superparamagnetic behavior which is extremely important for biomedical applications. Based on our results, APD is a stable functionalizing ligand that has the potential of being an alternative to dopamine as a robust anchor to magnetic iron nanoparticles which will enable their use in a variety of biomedical applications.

The limitation of using organic dyes is illustrated in their large and bulky size which increases the overall size of the particles and decreases their magnetization saturation. The next step in this road is to find a stable optical probe with enhanced

fluorescence and smaller size to save the magnetic properties of the Fe@FeOx nanoparticles. Our next choice is to use semiconductor nanoparticles known as quantum dots (QDs) to fulfill the fluorescent part of our dual mode system.

Chapter 3: CdS coated iron nanoparticles

I.1 Overview

As concluded at the end of chapter two, magnetic Fe@FeOx nanoparticles were functionalized using APD. The organic ligand coating of the particles surface led to a reduction in their magnetization saturation. Since the underlying goal for the work presented in this dissertation is to prepare stable dual mode nanoparticle for in *vitro* optical imaging*;* stability, suitable size and magnetic properties are essential criteria. It is important to point out that the size of the functionalization ligand affect the magnetization of the particle. As the size of the ligand increases, the non-magnetic contribution increases resulting in an overall reduction in the particles magnetization.[135,136] This chapter provides a discussion of the next step in this journey that includes the optimization of both the magnetic and optical properties of the dual mode system.

Magnetic and optical enhancement

The stability and magnetization saturation of Fe@FeOx nanoparticles can be improved by modifying the previously used reverse micelles synthetic procedure. The surfactant mixture of nonylphenoxypoly(ethyleneoxy)ethanols, NP5/NP9, was used instead of the NP4/NP7 system because the chain length of the NP surfactant plays a major role in contributing to the stability of the particles.

NP5/NP9 system has more oxyethylene repeating units than the NP4/NP7 system and hence more hydrogen bonds can be formed between the surfactant head which stabilizes the particles and allow them to grow bigger.[137] In an anticipation to further stabilize the magnetic particles in aqueous media and keep the magnetization saturation at an optimal level, we decided to extend our search for an optical probe to semiconductors quantum dots (QDs).

Fluorescent probes used for imaging in a biological environment should have certain criteria including brightness, stability against photobleaching and it should be suitable for multi-detection.[138] Though traditional fluorophores such as organic dyes and fluorescent proteins have some of these properties, they lack photostability and their multiplexing properties are complicated.[139] Moreover, the large and bulky structures will cause magnetic dilution of the particles. Accordingly, quantum dots (QDs) attracted our interest because of their outstanding optical characteristics that far exceed those of traditional flourophores.

Quantum Dots are spherical semiconductor particles that have all three dimensions confined to the size range of 1-10 nm.[23,140] They are inorganic particles made of periodic groups II-VI, III-V or IV-VI such as (CdTe, ZnS and CdS), (GaAs and InP) and (PbTe and SnTe) respectively.[141,142] QDs have been the center of researchers' attention for the past decade owing to their exceptional optical properties that could be utilized in a variety of biomedical applications.[143] As discussed in chapter one, when bulk materials are reduced in size to the nanoscale distinct optical, magnetic, and electronic properties emerges. The focus of this section is to discuss the origin of the optical

properties in semiconductor nanoparticles. QDs possess all the previously listed criteria of an ideal fluorescent probe in addition to their high selectivity, high sensitivity and size and composition dependent emission.[144,145] This dependence is best explained by the quantum confinement effect which influences the properties of semiconductor materials as their size is reduced to the nanoscale. There is a qualitative and a quantitative way to define and discuss the quantum confinement effect but for our purposes a qualitative discussion will be carried out in the following section.

I.2 Optical properties of bulk semiconductors

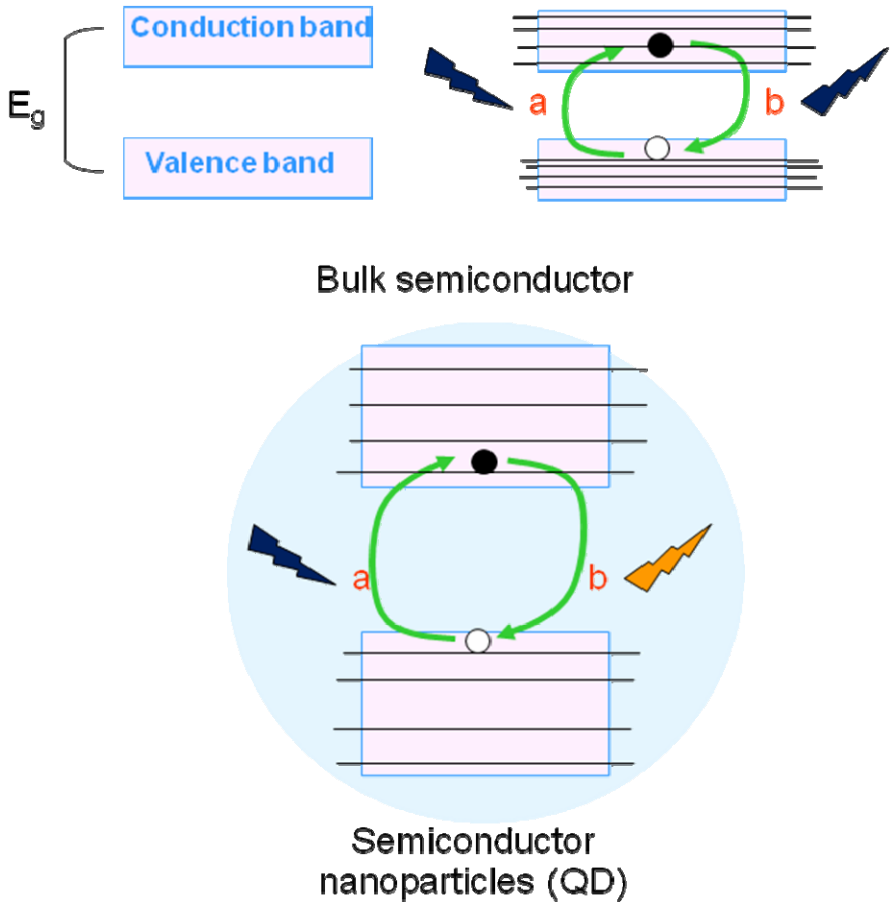

Figure 3-1: Schematic representing the band gap energy in bulk semiconductors and in semiconductors nanoparticles. The production of an electron-hole pair (a) and their radiative recombination (b) are also presented.

Figure 3-1 compares the emission process of semiconductor materials in the bulk phase and at the nanoscale. In general semiconductors have a valence band (the highest occupied electronic energy level at room temperature) and a conduction band (the highest unoccupied electronic energy level at room temperature).[23] The energy difference between these two bands is called the band gap (E_g) and it plays a major role in determining the wavelength of the emitted light. When a bulk semiconductor material absorbs enough light or thermal energy (equal or larger than E_g) an electron from the valence band gets promoted to the conduction band.[23] The vacancy left in the valence band after an electron is promoted is called a hole as shown in process (a) in Figure (3-I). The electron-hole pair is called an exciton and it is held together by coulombic interactions since they are oppositely charged. When the excited electron in the conduction band relaxes back to the valence band, it recombines with the hole emitting a photon with same energy as the band gap.[23,146] It is worth noting that the electronic energy levels of both bands in bulk semiconductors are close in energy and are described as continuous.[23] Therefore, the emission energy for semiconductors of the same composition in the bulk phase is fixed.

1.3 Optical properties of Quantum Dots

Just like bulk semiconductors, QDs have both conduction and valence bands that are separated by the band gap. However, the band's electronic energy levels are not continuous; in fact, they are quantized and separated with distinct energy from each other.[23,142,146] This is due to the quantum confinement effect that occurs as the size of the particle becomes comparable to the exciton Bohr radius. At that point, the band gap becomes greatly altered by the QDs size leading to a discrete emission wavelength that is dependent on the size of a single quantum dot.[142] Consequently, quantum dots of the same composition but different sizes can emit light with different wavelengths.

The qualitative part describes the quantization of the electronic energy levels of QDs using the "particle in a box" model which treats the electron and the hole as two particles in a spherical box.[23] As the dimensions of bulk semiconductors decrease to the nanoscale, the position of the electron and the hole becomes restricted inside the spherical box with zero probability for these particles to exist outside the box. Thus, the kinetic energy should increase to satisfy the Heisenberg uncertainty principle which indicates that if the position of the particle was defined then the momentum cannot be zero, therefore the kinetic energy cannot be zero. It is important to note that as the restriction of the particle's position increases (size decreases), the kinetic energy increases to balance out that restriction.[23] Fig 3-1 shows that the band gap energy increases as the size of the particles decreases, therefore, higher energy is needed to generate the electron-hole pair. A higher energy wavelength is also emitted upon recombination. It can be concluded from the above discussion that the band gap becomes dependent on the size of the QDs as a result of the quantum confinement effect originating from the size restrictions in QDs.

I.4 Biomedical applications of QDs

As a result of the quantum confinement effect, QDs provides enhanced optical properties. These properties made QDs strong potential candidates for many biomedical applications including their use as biomarkers in cell labeling and in the detection of biomolecules.[145,147] They can also be used in molecular diagnostics, immunoassays, and photodynamic therapies.[148-152] In this section, the optical properties of QDs will be highlighted along side with the corresponding applications.

I.4. 1 Imaging

Single color imaging

The enhanced optical sensitivity, biostability and bright fluorescence of QDs nanocrystals facilitated their use for *in vivo* imaging as well as cellular targeting. Several reviews addressed the significant role of QDs in real-time imaging of protein receptors on cell surfaces.[153-155] For example, it was reported in the review by Xing et al. that QDs provided a stable fluorescence over extended periods of time when used in real-time imaging of the embryonic development of a single cell cytoplasm in a frog embryo.[156]

Multi color imaging

QDs can be used in multi-detection for biological applications due to their multiplexing property.[23,157] Since their emission wavelength is dependent on the size of

the band gap, different colored emission could be obtained by changing the size and composition of these materials. On the contrary to traditional fluorophores, QDs have broad excitation spectra and narrow emission peaks which enables the excitation of different sized of QDs at the same time using a single excitation source. The emitted wavelengths of different QDs sizes can span the electromagnetic spectrum from the near ultraviolet to the near-infrared range without spectral interferences. Therefore, QDs make the perfect candidate for multi-detection applications including nucleic acid detection and genomic analysis.

I.4.2 Immunoassay

QDs could also be used in immunoassay for immediate detection of toxins or multiple analytes due to their stability under harsh environmental conditions and high quantum efficiency.[158,159] For example, CdSe-ZnS core-shell QDs coated with dihydrolipoic acid (DHLA) was used for the simultaneous detection of toxins in the environment, water and food supplies by conjugating relevant antibodies to QDs of different sizes.[160,161]

I. 5 Synthetic routes for quantum dots

There are several techniques to prepare QDs including electrochemical deposition, organometallic thermolysis and reverse micelles. For our purposes a brief overview of thermolysis and reverse micelles technique will be provided.

I.5.1 Organometallic thermolysis

High temperature synthesis using coordinating organic solvents such as a mixture of trioctylphosphine oxide (TOPO) and trioctylphosphine (TOP), hexadecylamine (HDA)

and octadecane (ODE). This reaction includes the decomposition of metal-organic or organometallic precursors such as dimethylcadmium or cadmium oxide for the formation of CdX (X= S, Se). These reactions are typically carried at elevated temperature in the range 180-310 ^{o}C. Even though this synthesis produces monodispersed and highly crystalline QDs, their surfaces are covered with hydrophobic ligands and they need to be water soluble for the use in biomedical applications. For this reason many researchers became interested in the surface functionalization of QDs.

Surface functionalization

As described in chapter 1, the surface of nanoparticles can be functionalized either by ligand exchange reaction or by surface capping. Ligand exchange reaction includes replacing the hydrophilic ligand on the surface of the as prepared quantum dots with a hydrophilic one. Most commonly used ligands are mercaptocarbonic acid, thiols, dithiols, thiolated poly(ethylene glycol) polymers, branched poly (ethyleneimine) and much more.[23,142,159] Though, the ligand exchange method maintains the small size of the QDs, it affects their physiochemical and photophysical stability which leads to poor quantum yields in buffered solutions.[162]

Surface capping

Surface capping takes place by using di- and tri- block copolymers or amphiphilic polymers such as octylamine- modified polyacrylic acid and poly(maleic anhydride-alt-1-tetradecene).[23,142] These amphiphilic polymers intercalate between the aliphatic chains covering the surface of the as prepared QDs while the original ligand remains in place. The drawback of this method is highlighted in the increase of the original QDs size by

three or four times. [162] For these reasons a better surface functionalization became indispensable. This guided our attention to the reverse micelles methods for QDs preparation especially that our Fe@FeOx nanoparticles are prepared using this technique.

I.5.2 Reverse micelles Synthesis

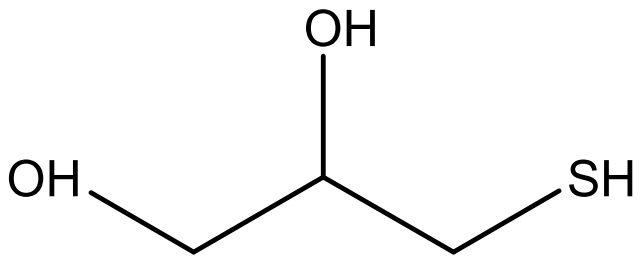

Figure 3-2: Thioglycerol

This technique is based on water-in-oil mixture resulting from the addition of the aqueous precursor to a surfactant solution. Merkoci et al. reported the synthesis of CdS quantum dots with the size range of 3-4 nm via reverse micelles synthesis.[139] In their work, they have used sodium dioctyl sulfosuccinate (AOT) as the surfactant and heptane as the oil phase. Briefly, two surfactant solutions containing cadmium perchlorate and sodium sulfide respectively were mixed under nitrogen and left to react for an hour. The resulting CdS quantum dots had a hydrophobic surface and it needed to be converted to a hydrophilic one. The ligand exchange method was used and thioglycerol (shown in

Figure 3-2) was added to the reaction mixture and left to react over night. Thioglycerol was added to stabilize the surface of the CdS QDs.

Since our Fe@FeOx nanoparticles are prepared using reverse micelles synthesis, we have envisioned creating a quantum dot shell around the magnetic iron nanoparticles. Combining the magnetic properties of magnetic nanoparticles and fluorescent quantum dots is not entirely new. Thakur et al. have reported the preparation of CdS-iron oxide nanocomposites by cross linking mercaptopropoinic acid (MPA) coated CdS QDs with iron oxide nanoparticles for the use in pH sensitive detection and biosensing.[163] The smallest particle size in these composites was 50 nm. Yu et al. also demonstrated the preparation of Fe_3O_4@ZnS for potential applications in drug targeting and bioseparation.[164]

We choose CdS is to be our fluorescent probe to coat the surface of the iron nanoparticles. CdS is the most frequently used of the QDs out of the II-VI element groups. It is known for its good optical transmittance and wide band gap of 2.4 eV.[27] CdS is also recognized for its color purity and wide emission wavelength range.[165]

II. Reverse Micelles synthesis of CdS@Fe nanoparticles

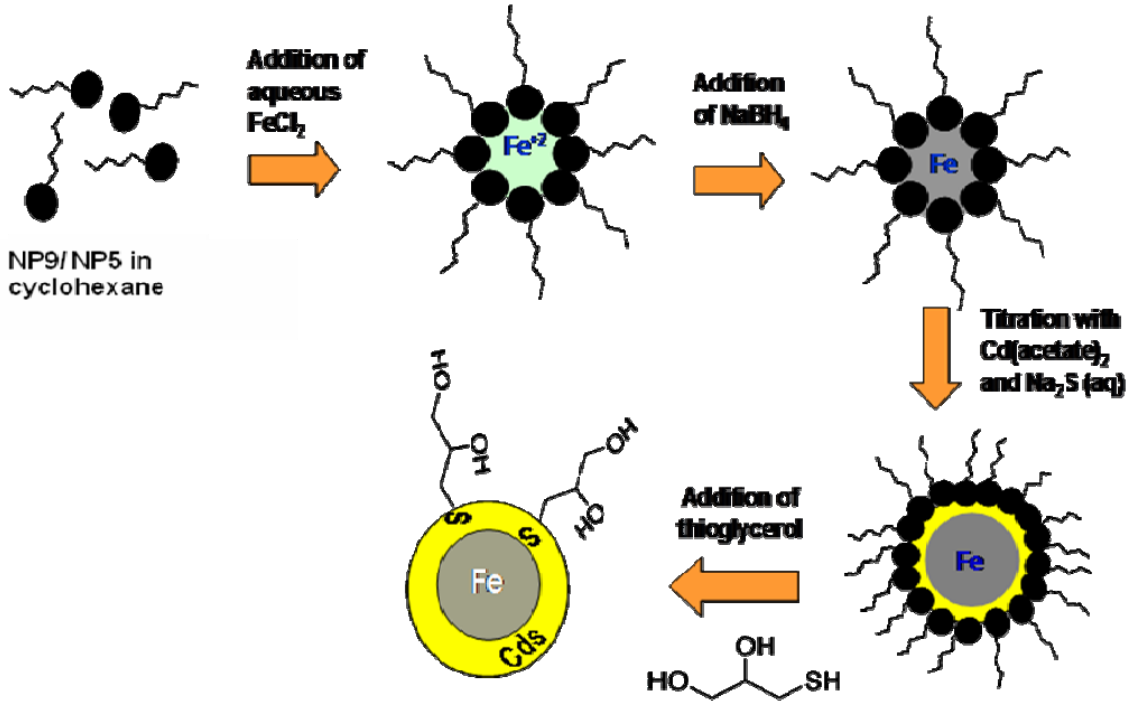

Figure 3-3: Schematic showing the reverse micelles synthesis of thioglycerol CdS@Fe nanoparticles

Iron nanoparticles and CdS quantum dots were synthesized using a modified reverse micelles method.[139,166] Both synthesis were modified and combined to synthesize cadmium sulfide coated iron nanoparticles as shown in Figure 3-3.[167] Three micelle systems were mixed under nitrogen, each system contained 3:1 ratio of nonylphenoxy poly(ethyleneoxy)ethanols (NP5) for a chain length of five and (NP9) for a chain length of nine, receptively, in cyclohexane. To the first solution, aqueous 0.693 M $FeCl_2$. $4H_2O$ was added, and reverse micelles were formed. Once, a transparent green micelle solution was obtained, 0.184 g of solid $NaBH_4$ was added to reduce the metal precursor. Almost instantaneously, the reaction mixture turned black due to the formation of metallic iron.[166] The magnetic nanoparticles act as the core while the other two micelles systems, one containing 0.347 M of aqueous $Cd(CH_3COO)_2$. $2H_2O$ and the other contained 0.352 M aqueous NaS. $9H_2O$ were added in stepwise fashion. The reaction mixture was then left to react for 1 hour before 0.414 ml of thioglycerol was added to stabilize the CdS shell of iron nanoparticles and left to react overnight. The produced particles were magnetically extracted and washed with pyridine, acetone and methanol, respectively, and then were dried under vacuum. The surfactant solution containing aqueous nickel chloride was eliminated from this synthesis in attempt of improve the magnetization saturation by having only metallic iron core without the oxide shell.

III. Experimental

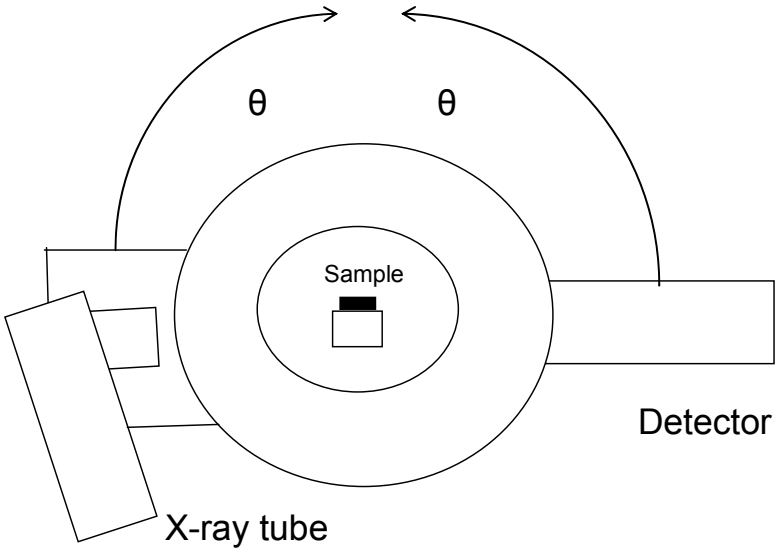

Figure 3-4: X-rays are generated from an x-ray tube under vacuum. The number of electrons emitted from the filament directly related to the amount (voltage) of the applied current. The high voltage accelerates the electrons towards a target, typically made of copper. These X-rays are directed towards the finely ground sample. Finally, the detector detects the signal which will be processed either electronically or by microprocessor to a count rate.

X-ray powder diffraction (XRD) is an instrumental technique that is used to identify crystalline materials and it is a fast and a reliable tool for material identification. As shown in figure 3-4 the XRD data is obtained by first the interaction of an X-ray beam with the material of interest, part of the beam is transmitted, part is absorbed, part is scattered and part is diffracted. X-rays are diffracted from different materials differently which depends on the composition and the arrangement of atoms in the crystal lattice. First X-rays are generated from and X-ray tube under vacuum when the filament within the tube is heated by the application of a current. The number of electrons emitted from the filament directly related to the amount (voltage) of the applied current. The high voltage accelerates the electrons towards a target, typically made of copper; the wavelength of the X-ray is dependent on the type of the target. Next, these x-rays are directed towards the finely ground sample. Finally, the detector detects the signal which will be processed either electronically or by microprocessor to a count rate. The distance between the atoms that constitute the sample could be measured by using Bragg's Law which is

$$n\lambda = 2d\sin\theta \qquad (1)$$

where the integer n is the order of the diffracted beam, λ is the wavelength of the incident X-ray beam, d is the distance between the adjacent planes of atoms (d-spacing) and θ is the angle of incidence of the X-ray beam. It is worthy of mentioning that the d-spacing provides a unique fingerprint of the sample's material, these data could be compared to a

standard reference pattern of that material which helps in its identification. For the purposes of this work, powder X-ray diffraction (XRD) was taken on a PANalytical X'pert pro diffractometer at a scanning step of 0.400°, in a 2θ range from 20° to 80° with monochromated Cu-Kα radiation. Powder samples were prepared by grinding using a mortar and pestle and then placing them on low background sample holder.

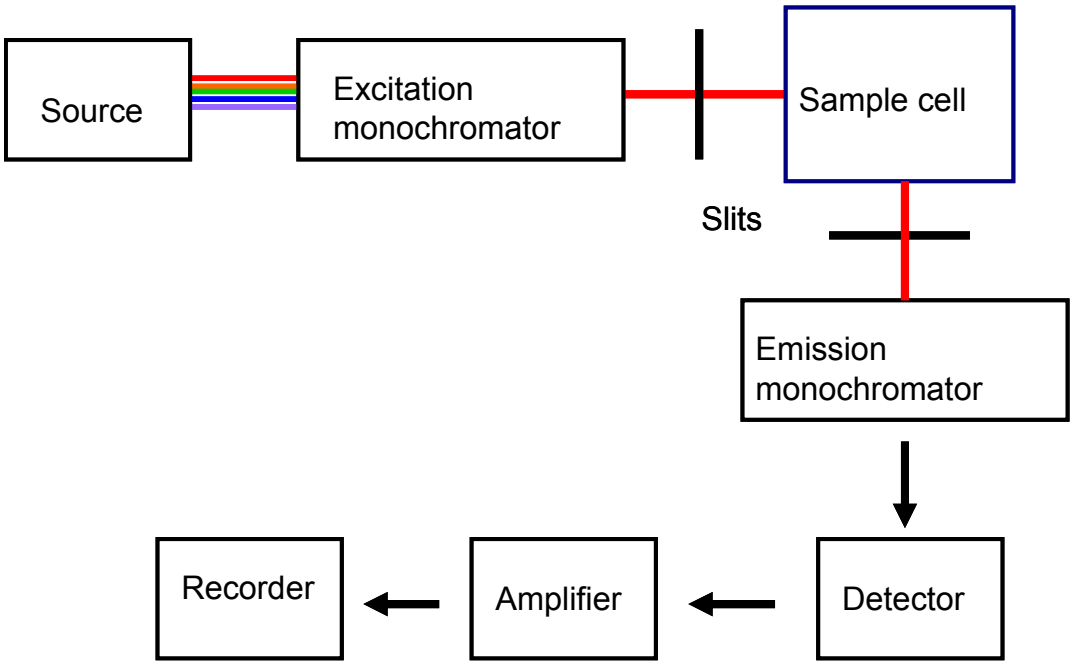

Figure 3-5: The sample is excited by a UV light. The light passes first through the excitation monochromator which only allows for the passage of a selected excitation wavelength through sample resulting in the electronic transition to an excited state which provides the excitation spectrum. The fluorescence monochromator allows for the passage emitted light which is detected by a photomultiplier tube which provide the emission spectrum.

Fluorescence spectroscopy is used to measure the wavelength of the emitted light as a result from the electronic relaxation from a singlet excited to a singlet ground state. The wavelength and therefore of the energy of emitted light is dependent on the band gap between the ground and the excited state of the material of interest. Fluorescence occurs when an electron in the ground state of a certain material absorb enough energy to allow its promotion from a singlet ground state to a singlet excited state. Then when the electron relaxes back to the ground state, the previously absorbed energy is emitted as light of a certain wavelength and it is characteristic to the band gap energy of the sample.

As shown in Figure 3-5, the sample is excited by a UV light and the source is typically a deuterium of a xenon lamp. The light passes first through the excitation monochromator which only allows for the passage of a selected excitation wavelength through sample resulting in the electronic transition to an excited state which provides the excitation spectrum. On the other hand, the fluorescence monochromator allows for the passage emitted light which is detected by a photomultiplier tube which provide the emission spectrum. In our work, Fluorescence measurements were obtained using Cary Eclipsed fluorometer to measure the emission wavelength of the plain thioglycerol coated CdS quantum dots and the CdS coated nanoparticles.

IV. Results and discussion

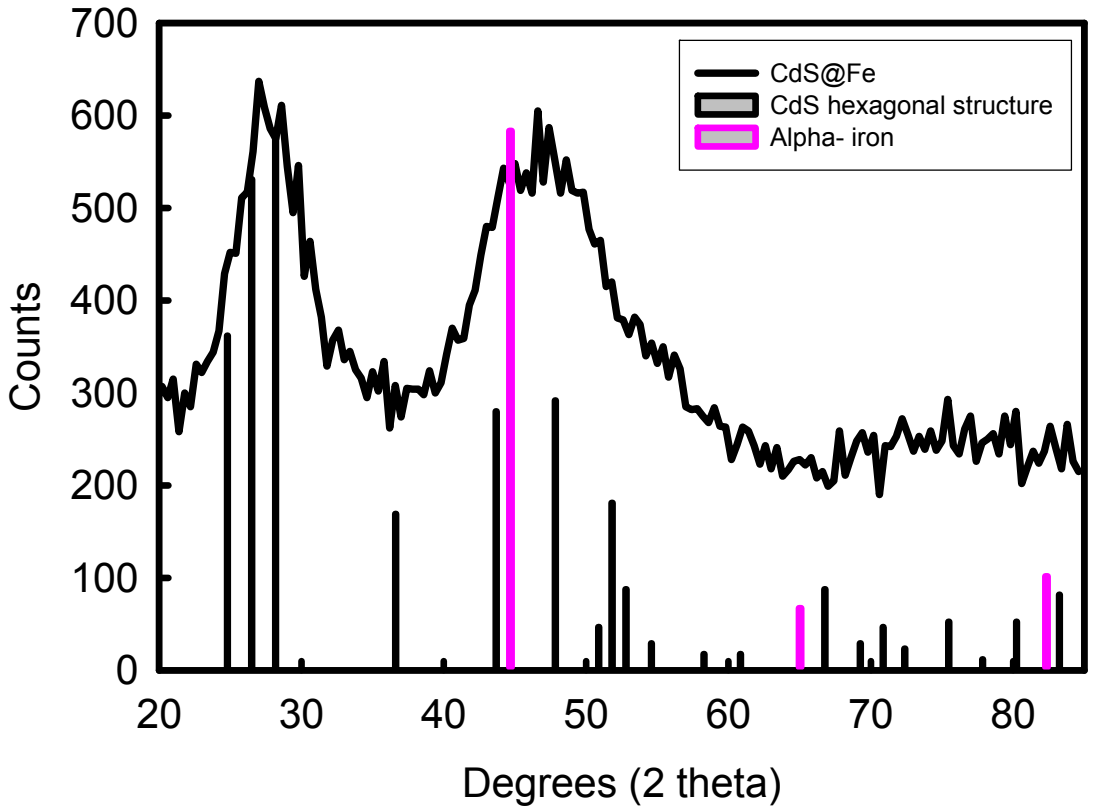

Figure 3-6: XRD patterns CdS@Fe nanoparticles. The colored vertical lines represent JCPDS reference profiles of both crystal lattice structures of cadmium sulfide and Fe Bragg diffraction peak intensities as shown in the legend

Figure 3-6 presents a diffraction pattern of the CdS coated nanoparticles. In the figure, the raw data collected is depicted with an overlay of data obtained from JCPDS reference powder diffraction files of the hexagonal (41-1049) lattice structures of cadmium sulfide, and α-Fe (87-0721) in which the intensity and position of each diffraction peak is represented by a vertical line. The most intense peaks at 26.5º, 30.81º, 43.96º and 52.13º 2θ, corresponds to the (111), (200), (311) and (220) planes in the cubic CdS crystal network, respectively. The most intense peaks of the hexagonal CdS crystal lattice overlaps with those of the cubic lattice only at 26.51°, 24.81º and 28.18º corresponds to the (002), (100) and (101) planes, respectively. The diffraction pattern shows a broadening of the (110) peak of α-Fe and an absence of the 100% (311) plane of magnetite. From this it can be concluded that the core mainly consists small crystallites of α-Fe. The broadening of the CdS diffraction pattern is due to the small shell thickness size of the coated particles.[27] As the size of the QDs increases, they become more crystalline and the broadened peaks resolve and become apparent as shown in literature.

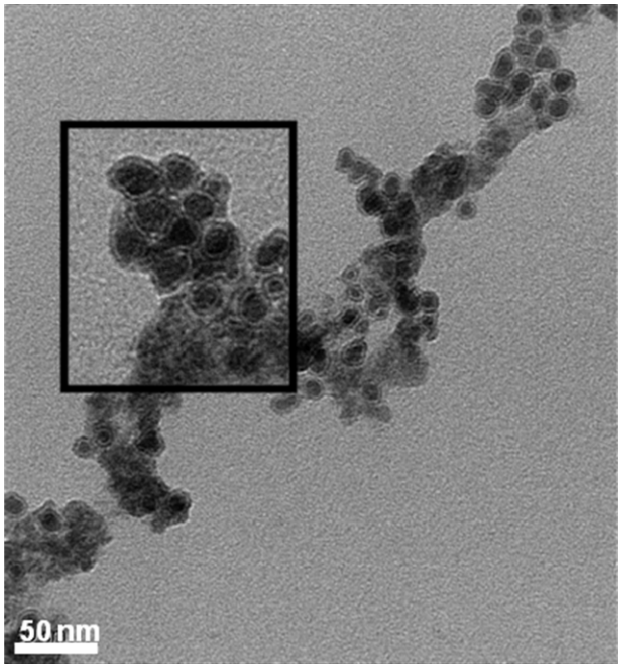

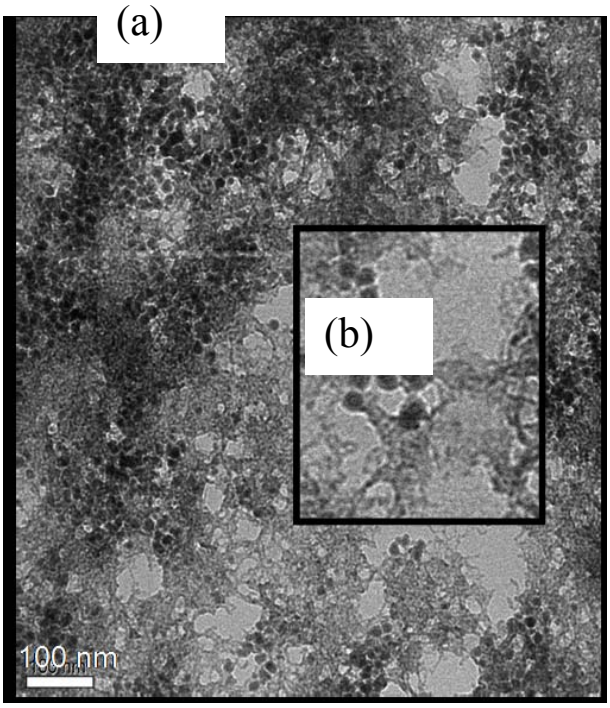

Figure 3-7: TEM of CdS@Fe nanoparticles before coating with thioglycerol (top) and thioglycerol coated CdS@Fe nanoparticles (bottom). The image shows core shell morphology of iron coated with CdS. Thioglycerol is represented by the grey area around the core shell particles.

As illustrated in Figure 3-7 transmission electron microscopy shows aggregated CdS@Fe (top), while the inset of the figure shows an enlarged portion of the image presents core shell morphology of these particles. The dark core represents the iron and the lighter shell represents CdS. More isolated particles are present in Figure 3-7 (bottom) for CdS@Fe nanoparticles after coating with thioglycerol which is represented by the grey area around the particles. The approximate size of the thioglycerol coated nanoparticles is 14 +/- 3 nm.

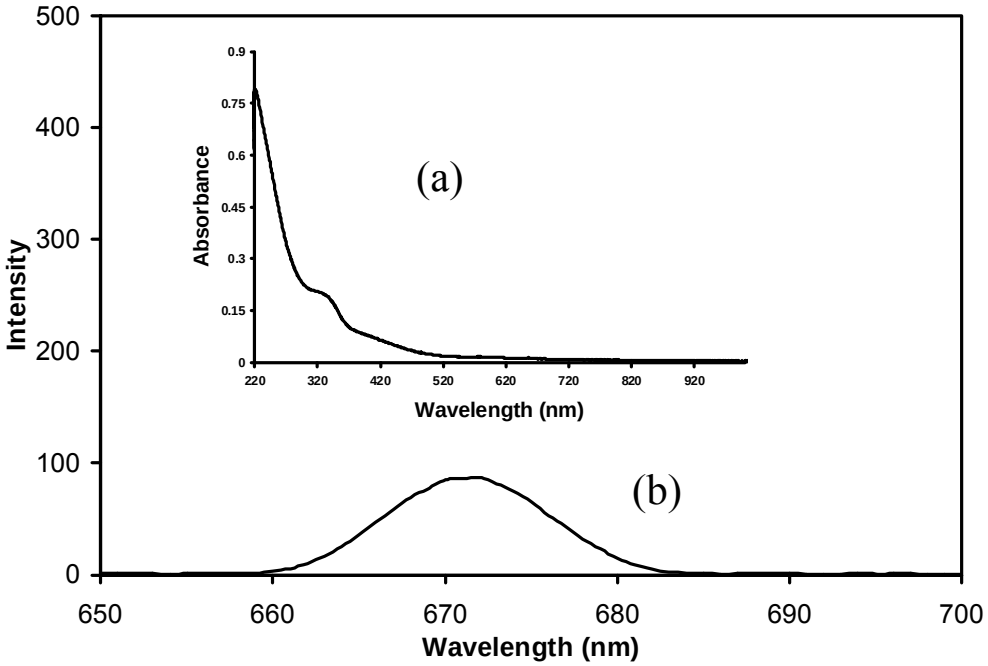

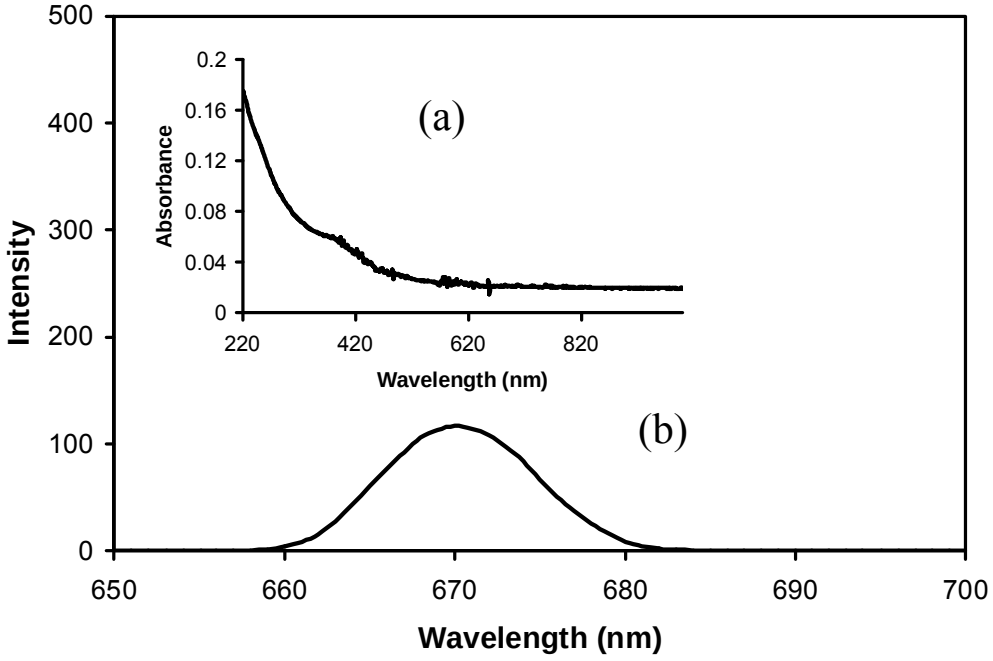

Figure 3-8: Absorption (a) and emission (b) spectra of thioglycerol coated CdS QDs (top) and thioglycerol coated CdS@Fe nanoparticles

Frigure 3-8 thioglycerol coated CdS quantum dots have an absorbance peak in the range of 290 and 360 nm (Top). This peak was broadened and shifted to a higher wavelength for the thioglycerol coated CdS@Fe nanoparticles (bottom). Using the maximum point in the absorption spectra, both CdS quantum dots and the coated particles were excited using 335 nm as the excitation wavelength. Fluorescence measurements of both types of particles are present in Figure 3-8. Emission wavelengths of 672 nm and 670 nm was observed for the CdS coated Fe nanoparticle which is in agreement with literature values of thioglycerol coated CdS quantum dots.[168] It is worth noting that the CdS quantum dots that compose the shell around the iron naoparticles is 2 nm which is the same size as the free CdS quantum dots measure in Figure 3-9. This is apparent in

similarity of the absorbance and fluorescence values measured for CdS quantum dots and CdS@Fe nanoparticles.

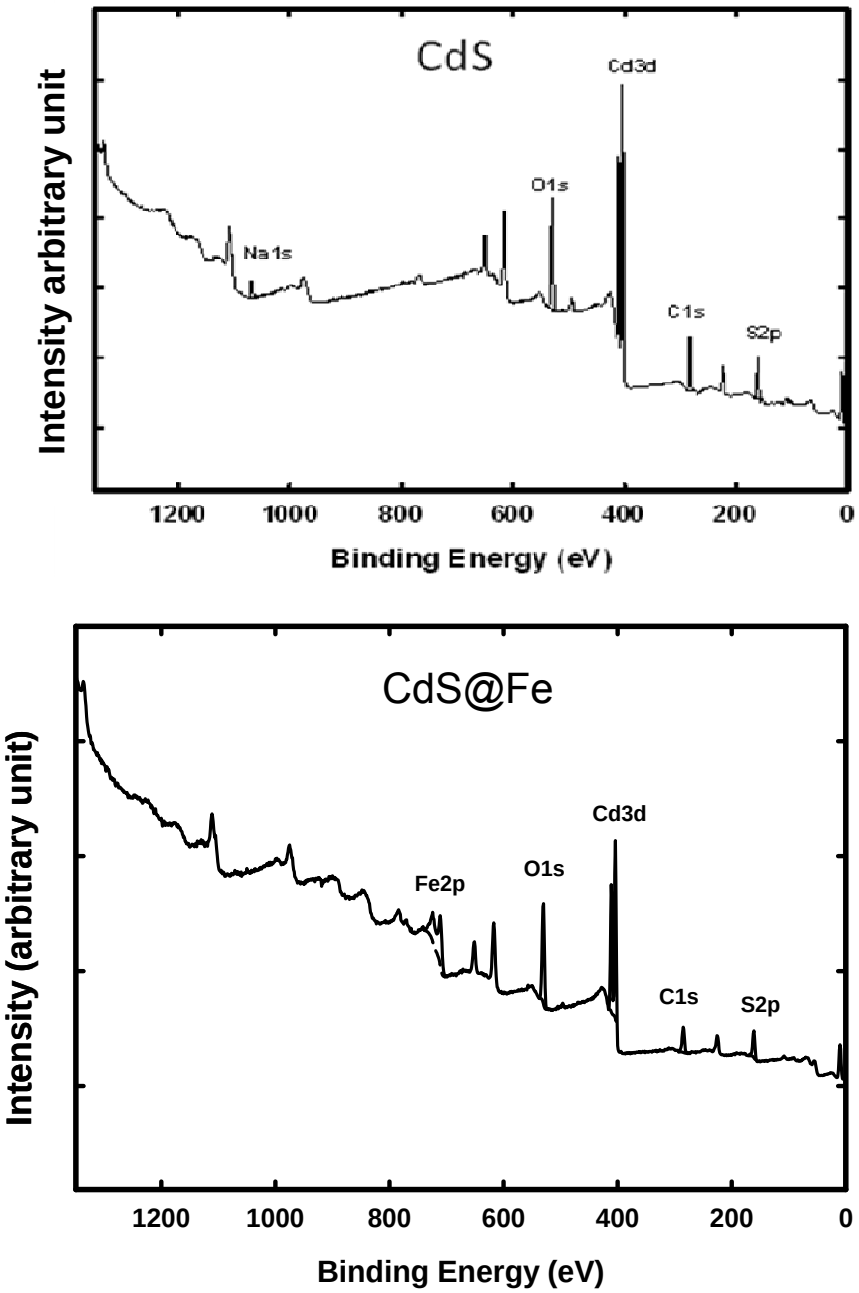

Figure 3-9: XPS survey scans of CdS quantum dots (top) and CdS@Fe nanoparticles (bottom)

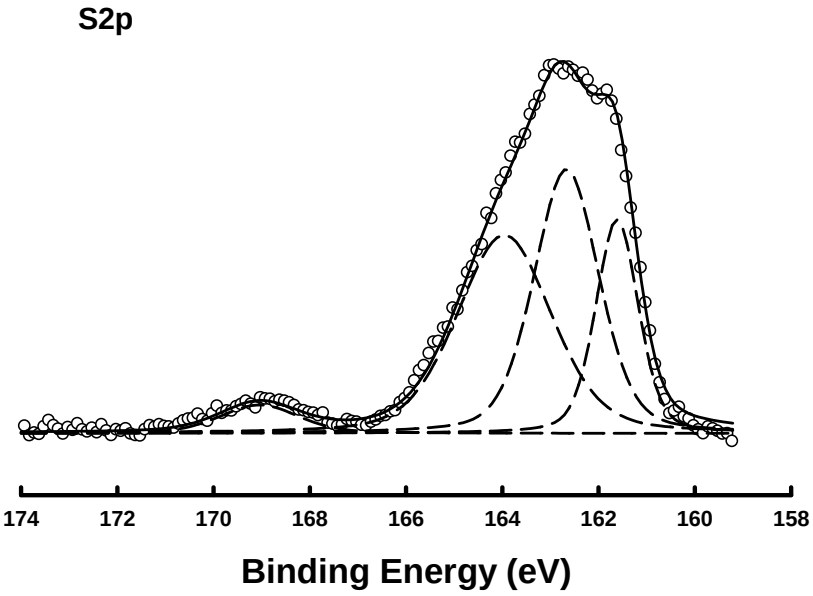

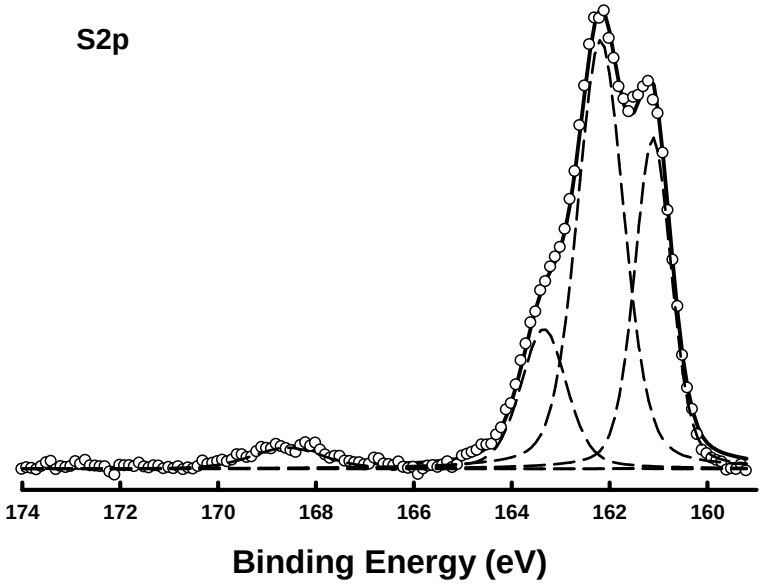

Figure 3-10: XPS S2p region scans for CdS (top) and CdS@Fe (bottom) nanoparticles, the raw data are represented by a dots, the fitted peaks are represented by the dashed line and the horizontal solid line is the baseline

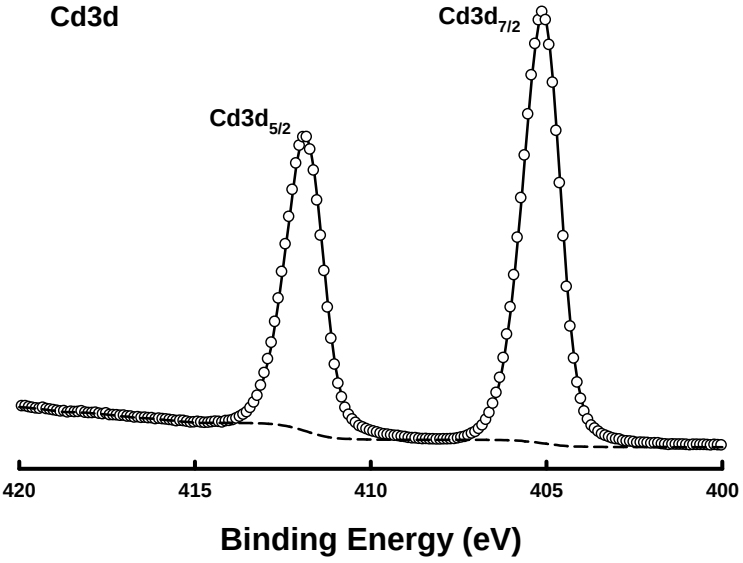

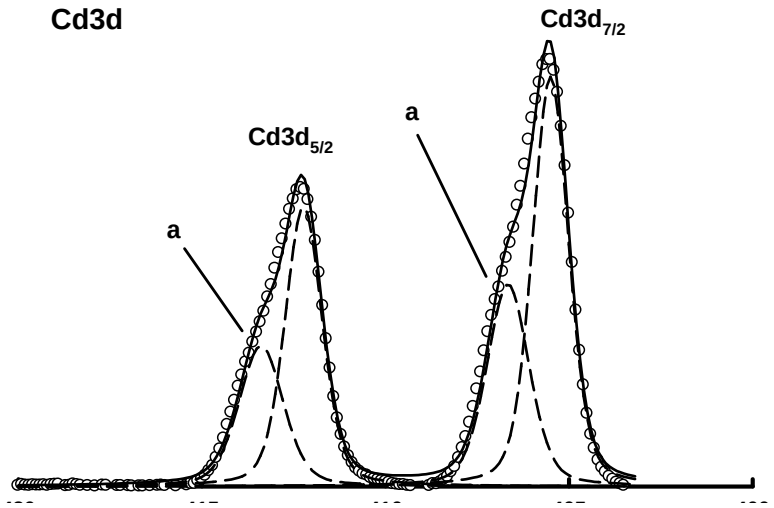

Figure 3-11: XPS Cd3d region scans for CdS (top) and CdS@Fe (bottom) nanoparticles. the raw data are represented by a dots, the fitted peaks are represented by the dashed line and the horizontal solid line is the baseline. The symbol (a) represents the presence of an extra peak in the regional scan of CdS coated particles when compared to the regional scan of the free QDs

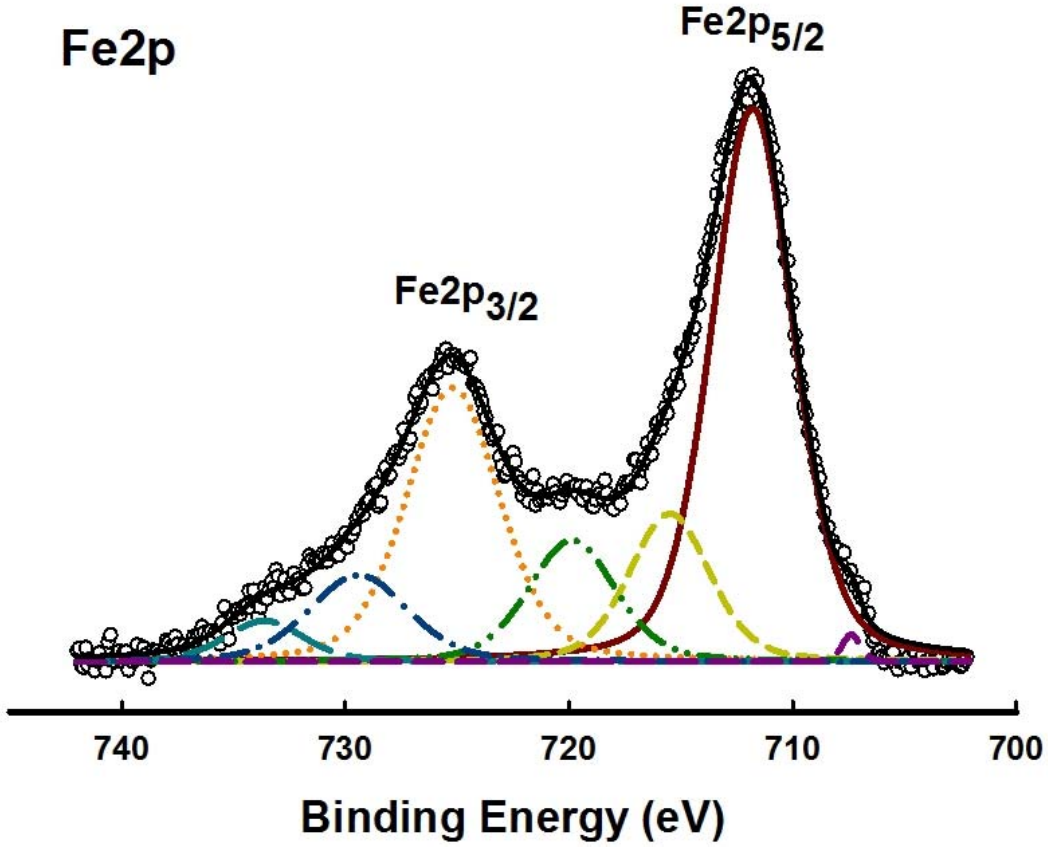

Figure 3-12: XPS Fe2p region scans for CdS@Fe nanoparticles. The peaks locations indicate the presence of iron(II) on the surface of the CdS@Fe nanoparticles, which can be explained by the adsorption of unreacted Fe which formed a thin oxide layer. It also shows the presence of iron represented by the small peak at 708 eV. the raw data are represented by a dots, the fitted peaks are represented by the dashed line and the horizontal solid line is the baseline

To evaluate the surface chemistry of the CdS and CdS@Fe nanoparticles, XPS measurements have been collected. Survey scans determined that Na, S, O, Cd, Cl and, in the case of the CdS@Fe, Fe were on the surface of each sample as illustrated in Figure 3-9. The binding energies of the Cd $3d_{5/2}$ peak for the CdS and CdS@Fe nanoparticles were 405.18 eV and 405.2 eV, which is consistent with literature (Figure 3-11).[169-173] An extra peak is shown for the CdS@Fe nanoparticles which is consistent with adsorbed un-reacted $CdCl_2$ in the sample.[174] The S2p spectra indicate the presence of 3 peaks at 161.71, 163.84, and 168.98 eV as shown in Figure 3-8. These peaks can be attributed to a cadmium sulfide, thioglycerol, and sodium sulfate, respectively.[175,176] The sodium sulfate is thought to be an impurity from the sodium sulfide precursor. The Fe2p spectra (Figure 3-12) indicates the presence of iron(II) on the surface of the CdS@Fe nanoparticles, which can be explained by the adsorption of unreacted Fe which formed a thin oxide layer. In addition, the small intensity peak around 708 eV is represents metallic iron. The other peaks present in the regional scans are attributed to shake-up peaks.

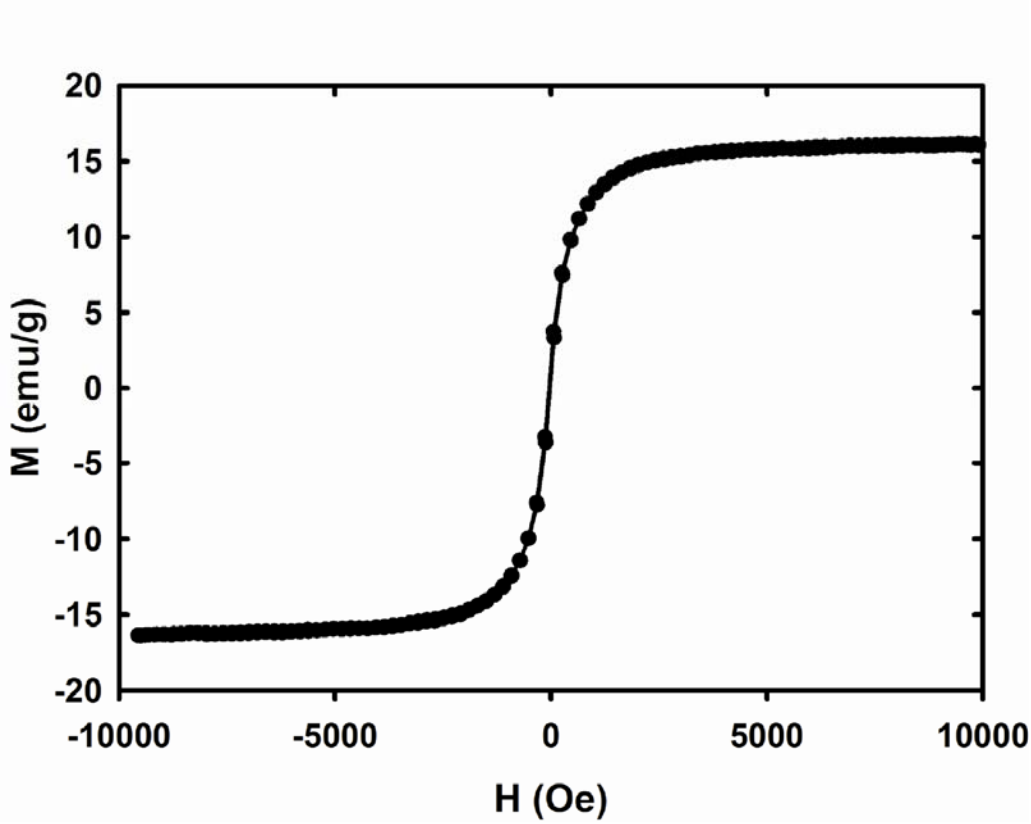

Figure 3-13: VSM measurements of thioglycerol coated CdS@Fe nanoparticles

The magnetic properties of the coated particles were also measured at room temperature using vibrating sample magnetometer. As illustrated in Figure 3-13 the particles showed a superparamagnetic behavior with a magnetization of 16 emu/ g with coercivity below 20 Oe. The low magnetization could be mostly due magnetic dilution from the CdS shell and the thioglycerol coating.

V. Conclusion

In conclusion, magnetic nanoparticles coated with fluorescent cadmium sulfide were synthesized via reverse micelles methods. TEM images showed core-shell morphology of the produced particles. Their combined magnetic and optical properties were illustrated by vibrating sample magnetometer and fluorescence spectroscopy. They were also functionalized with the organic ligand thioglycerol which enable their dispersion in water. Although cadmium sulfide quantum dots have extraordinary optical properties, the issue of magnetization reduction as a result of coating remains. At this point, our search continued once again for an optical ligand that saves the magnetization saturation of the magnetic core. Our attention was directed to the optical organometallic coordination compound. The mixed valence Prussian blue compound was our next candidate due to its exceptional properties which will be discussed at length in chapter 4.

Chapter 4: Prussian Blue Coated Iron Nanoparticles for Biomedical Applications

I.Overview

As concluded at the end of chapter three, magnetic iron nanoparticles were functionalized using cadmium sulfide shell. The magnetization saturation was reduced as a result of the coating. In this chapter, we aim to find a stable optical probe to coat the surface of iron nanoparticles without affecting their magnetization. Our search for a new functionalization ligand lead us to the inorganic pigment, Prussian blue (PB) or ferric ferrocyanide, $Fe^{III}_4(Fe^{II}(CN)_6).xH_2O$. PB has unique optical properties including its intense blue absorption; these properties are advantageous for variety of applications. PB is smaller and less bulky than organic fluorophores, it is also very stable because the cyanide group is a strong field ligand and it is held tightly to the iron.[177]

Prussian blue was first reported in the eighteenth century as one of the oldest synthetic coordination compounds.[178,179] In the early 1700s, PB was discovered and used as pigment for the first time in Berlin and therefore it is also known as Berlin blue.[180] The initial preparation of Prussian blue came about by chance. The story begins when the artists' colormaker Heinrich Diesbach attempted to prepare crimson color. He needed iron sulfate and potash (potassium carbonate) and he did not have the latter. In an effort to be cost-effective, Diesbach bought potash that was contaminated with animal oil.

This elixir contains a malodorous distillate of animal carcasses- blood, bones, and offal.[181] To his surprise, instead of making crimson color, he ended up introducing a new pigment for painters and a unique synthetic coordination compound to the field of chemistry.[181] This coincident happened because animal oil contaminated potash included nitrogenous organic bases and a mixture of compounds that contained C-N bonds resulting from the thermal degradation of molecules such as hemoglobin.[181]

Since Prussian blue pigment was generated by chance, the actual preparation methods that is known today did not unfold until the earlier years of the 19th centuary.[181] At that point scientist were amazed by the ease and simplicity of this reaction which includes the mixing of the aqueous solutions of ferri and ferrocyanide salts.[182,183] The breakthrough of this finding was commemorated by showing this reaction in a painting presented in the stock-in-trade for the public lecture-demonstration of celebrated 19th centaury chemists.[181]

Although Prussian blue pigment was discovered and used since the eighteenth century, its crystal structure and analytical composition was not understood until recently. Keggin and Miles were the first to discuss the crystal structure of PB on the basis of powder diffraction patterns.[182] They were then followed by Ludi and co-workers who reported further comprehensive investigations using single crystal analysis of PB by the means of electron and neutron diffraction.[184] From their studies it was established that Prussian blue packs into a simple cubic crystal generating a three dimensional polymeric network. Fe(II) and Fe(III) ions interchange position on a face centered cubic (FCC)

lattice in a way that Fe(III) ions are enclosed octahedrally by the nitrogen atoms while Fe(II) ions are surrounded by the carbon atoms.[181,183] Prussian blue has unique optical, electrochemical and magnetic properties due to the interaction between the mixed valence iron ions present in its lattice structure.

I.1 Optical Properties

Prussian blue has an intense blue color derived from the absorbance of visible light around 700 nm. This absorbance causes the transfer of an electron from the low spin Fe(II) ion to the high spin Fe(III) ion over the cyanide bridge.[183] The optical properties of Prussian blue were the reason behind its use in many biomedical applications. Prussian blue staining is well known and widely used in histochemistry analysis; it was used to detect the accumulation of superparamagnetic FeOx nanoparticles in cells for the use as contrast agents for MRI imaging.[185-187] Koncki et al. have reported that PB can also be used as stable optical pH sensor.[188] Prussian blue has optical characteristics beyond its notable absorbance in the visible range such as its interesting optical redox properties. Everitt's salt or Prussian white, $K_2Fe^{II}Fe^{II}(CN)_6$, is the reduced form of PB and it is colorless.[189] Berlin green or Prussian yellow, $Fe^{III}Fe^{III}(CN)_6$, is the oxidized form of Prussian blue and it has a green color.[189] The color of PB changes upon reduction and oxidation, for this reason PB is considered to be an electrochromic material which is suitable for various digital displays devices.[190,191]

I.2 Electrochemical Properties

The uniqueness of the Prussian blue structure is not limited to its attractive mixed valence nature. The crystal lattice of PB is described as zeolitic with cubic unit cell length of 10.2°A and channel diameters of about 3.2°.[192,193] Accordingly, the PB crystal lattice is spacious and contains pores and tunnels in all three dimensions.[181] The porous structure of PB opened new possibilities for its use in electrochemical and medical applications. Recently, PB modified electrodes were used as oxidase-enzyme biosensors by detecting the generation of hydrogen peroxide resulting from enzyme substrate oxidation.[181,194,195] The cavities present in the PB crystal lattice served as ion traps to lock in such toxins, PB was orally administered by affected patients because it is tasteless, non-toxic and stable.[196]

1.3 Magnetic properties

The mixed valence Fe(II)/ Fe(III) ions in the crystal lattice of PB also produces remarkable magnetic properties. The NC--Fe(II)--CN bridge with a distance of 10 Å allows for a week superexchange interaction between the paramagnetic Fe(III) ions.[196] Below Curie temperature Tc= 5.5K, the electron spins of Fe(III) switch from a random state to an ordered one where the spins align with the applied field.[196,197] Even though the ability to switch PB magnetism is appealing, a higher Curie temperature is needed for technological applications such as data storage and molecular electronics.[198-201] This issue opened the door into introducing a new class of Prussian blue compounds, Prussian

blue analogues such as Co^{II}_3 $[Fe^{III}(CN)_6]_2$, $Ni_3[Fe(CN)_6]_2$, $Mn_3[Fe(CN)_6]_2$, and $Cu_3[Fe(CN)_6]_2$ are few examples.[198-201] Changing the metal ions can have an effect on the nature of the interaction between these metals which affects the ordering temperature and accordingly the magnetism of the compound.[200,201] For instant, paramagnetic Co(III) ions in Co^{III}_3 $[Fe^{II}(CN)_6]$ can switch from between the paramagnetic and diamagnetic and vice versa by light irradiation of different wavelength.[202,203]

PB is easy to prepare, safe to handle, very stable, electrochemically active, known for its selectivity and sensitivity, it has high storage stability, low cost and ease of electrode surface modification.[91] For this reason PB was the chosen candidate for the use as an optical probe bonded to the surface of Fe nanoparticles. We propose a novel synthesis for preparation of Prussian blue coated iron oxide (PB@Fe) nanoparticles utilizing a reverse micelle approach. The idea of combining the unique properties of both superparamagnetic Fe@FeOx nanoparticles and Prussian blue optical probe seemed very attractive for optical imaging in *vitro*.

II. Synthesis of PB coated nanoparticles

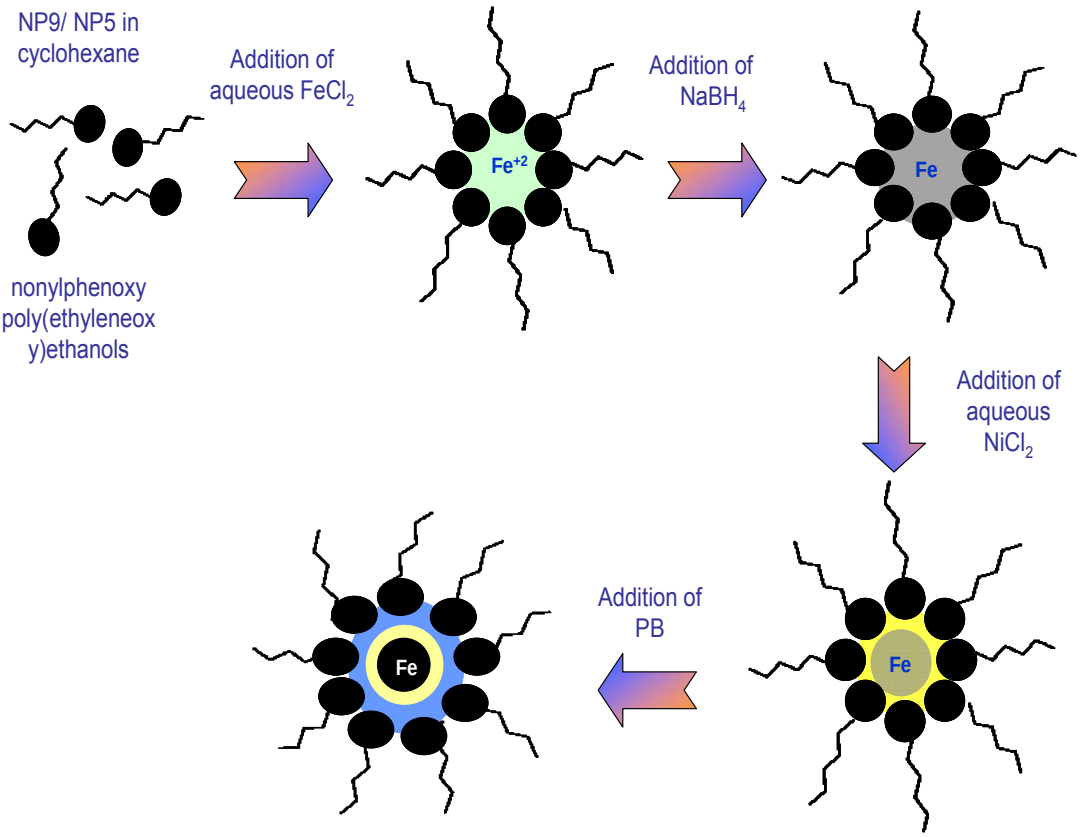

Figure 4-1: Reverse micelles synthesis for the preparation of Prussian blue coated Fe@FeOx nanoparticles

Iron nanoparticles were synthesized using a previously described reverse micelles method.[177] Unlike the functionalization procedure described in the last chapter, the functionalization step for this reaction was carried out during the synthesis. To do this, three surfactant solutions were prepared, each contained 1:4 mass ratio of nonylphenoxypoly(ethyleneoxy)ethanols (NP5) for a chain length of five and (NP9) for a

chain length of nine receptively in cyclohexane. As shown in Figure 4-1, 0.699 M of aqueous $FeCl_2.4H_2O$ was added to the first solution, and reverse micelles were formed. Once, a transparent green micelle solution was obtained, 0.366 g solid $NaBH_4$ was added to reduce the metal precursor. Almost instantaneously, the reaction mixture turned black due to the formation of metallic iron nanoparticles. In 20 minutes, the second surfactant solution containing 0.353 M of aqueous $NiCl_2.6H_2O$ was added to the reaction vessel in order to passivate the iron nanoparticles and protect them against further oxidation. In 4 minutes, the third surfactant solution containing 0.00933 M of aqueous PB was added and left to react for 30 minutes. Finally, the reaction was quenched using 2:1 ratio of methanol and chloroform solution. The resulting PB coated nanoparticles were washed and collected in methanol by magnetic extraction and then left to dry under vacuum. Prussian blue coordinated to the iron present in the surface of the nanoparticles through the nitrogen of the cyanide group.

III. Experimental

Thermogravimetic analysis (TGA) is a thermal characterization method that measures the weight loss or gain as a function of temperature. The weight loss or gain can result from any one or more of these reasons: drying, gas evolution as a result of chemical reaction during the measurement, the materials reaction with the atmosphere in the chemical environment.[204] The sample is positioned on an aluminum cup that is supported on an analytical balance which located outside the furnace chamber. After the balanced is zeroed, the sample is heated and the weight signal is stored as well as the sample temperature and the elapsed time. The TGA curve represents the percent weight change versus the materials temperature.[204]

Differencial scanning calorimetry (DSC) is also a thermal analysis technique, it measurers the effects of heat that is associated with phase transition and chemical reaction as a function of temperature. In the DSC measurements, a reference which cosistes of an inert material or simple an empty aluminum pan is used.[205] The difference of the heat flow to the sample and the reference is recorded at a certain temperature.[205]

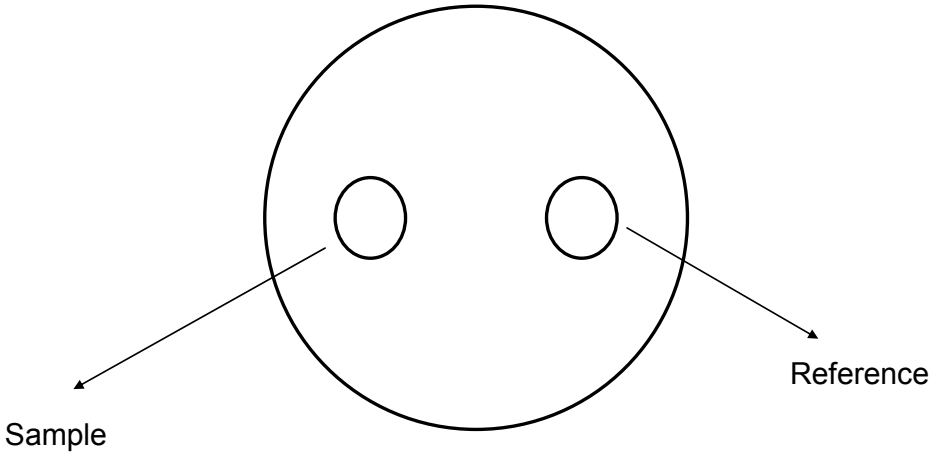

Figure 4-2: Top view of the furnas with the cover off (DSC) for both the reference and the sample holders are made of platinum to allow for the carrying out the measurements at higher temperature. Resistant heater and temperature sensor are located under each holder

Figure 4-2 shows a top view of the furnace with the cover off, both the reference and the sample holders are made of platinum to allow for the carrying out the measurements at higher temperature. Resistant heater and temperature sensor are located under each holder. When current is applied to both heaters, the temperature is increased at a certain rate. The measurements are carried in a nitrogen gas environment to provide a dry environment and prevent oxidation at high temperature. Both the reference and the sample are sealed, the reference is usually an empty pan and a cover.

For our purposes, Thermogravimetric analysis (TGA) and differential scanning calorimetry (DSC) were done using a Q5000 TGA and a Q200 DSC, respectively. Both of these measurements were carried out in a nitrogen atmosphere.

IV. Results and discussion

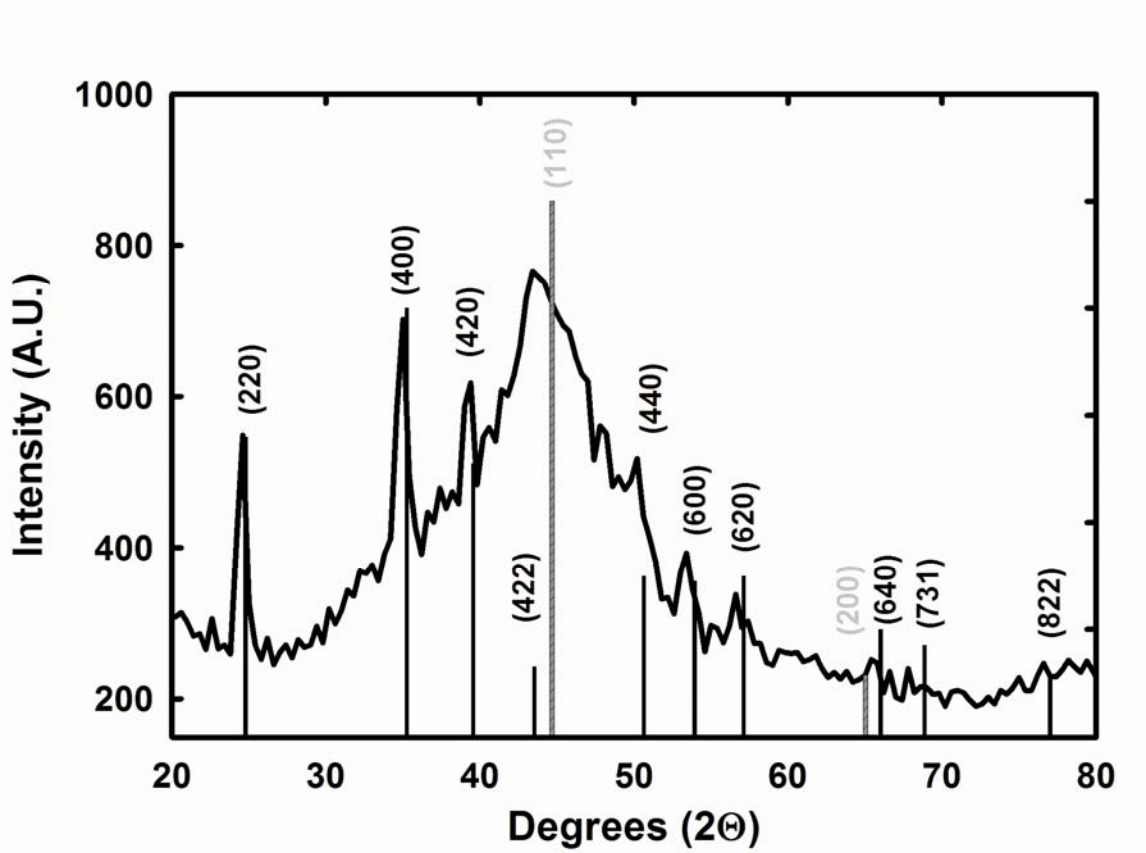

Figure 4-3: XRD pattern of PB@Fe nanoparticles. The black and grey lines represent JCPDS reference profiles of Prussian blue and Fe Bragg diffraction peak intensities, respectively

Figure 4-3 presents the X-ray powder diffraction pattern of the PB coated nanoparticles. The raw data collected is depicted with an overlay of data obtained from JCPDS reference powder diffraction files of Prussian blue (52-1907) and α-Fe (87-0721) in which the intensity and position of each diffraction peak is represented by a vertical line. By comparing the reference diffraction peaks to the collected data, it is clear that the raw data is a representation of both PB and α-Fe. The most intense peaks at 24.6º, 35.0º and 39.4º 2θ, corresponds to the (220), (400), and (420) planes in the PB crystal network, respectively. It is important to point out that the diffraction angles of the collected data is shifted to lower angles when compared to the reference diffraction patterns. This could be due the change in the spacing between the planes of the CdS crystal lattice as a result of alloying with the iron lattice. The diffraction pattern shows a broadening of the (110) peak of α-Fe which can be explained by the amorphous contribution from the small size. It is worthy of mentioning that the (422) peak of PB overlaps the (110) peak of α-Fe in the 40-50º 2θ diffraction pattern region of the collected data, which can also have a part in the peak broadening in that area. In addition, the XRD data revealed that the 100% (311) plane of magnetite shell is absent which lead us to conclude that the core of the particles mainly consists small crystallites of α-Fe. The FeOx shell of the produced particles contains water and hydroxide ligands adsorbed to the surface of these particles. Nitrile ligands of the PB compound are stronger field ligands than the water, hydroxide, and oxide that are present in the shell. When the particles are coated with PB, the ligands present on the surface are replaced with the nitrile ligands via ligand exchange

reaction.[191,206] As a result, the magnetite diffraction patterns are not present in the XRD data presented in Figure 4-3

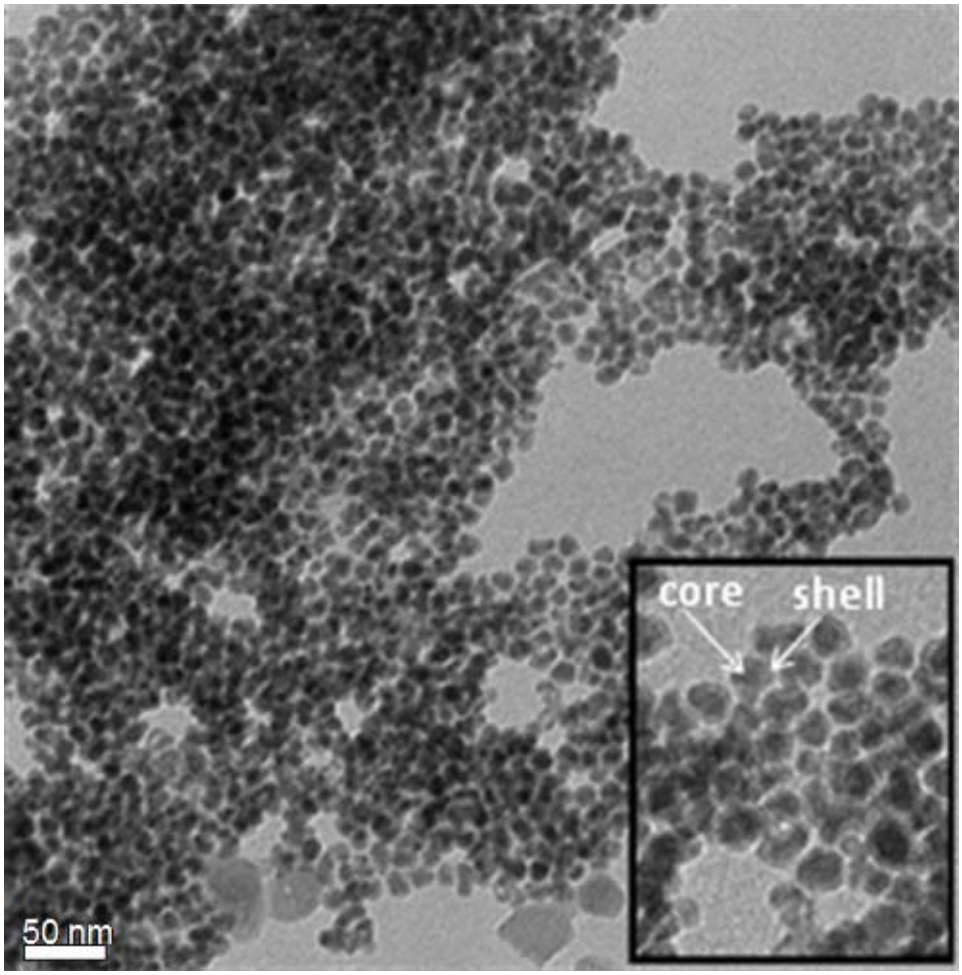

Figure 4-4: Transmission Electron Microscope image of PB coated nanoparticles

Transmission electron microscopy shows the PB@Fe nanoparticles with an average size of 11 ± 2 nm. The inset of Figure 4-4 shows an enlarged portion of the image which clearly presents defined core-shell morphology. The dark colored core is attributed to the iron and the lighter colored shell represents the PB coating.

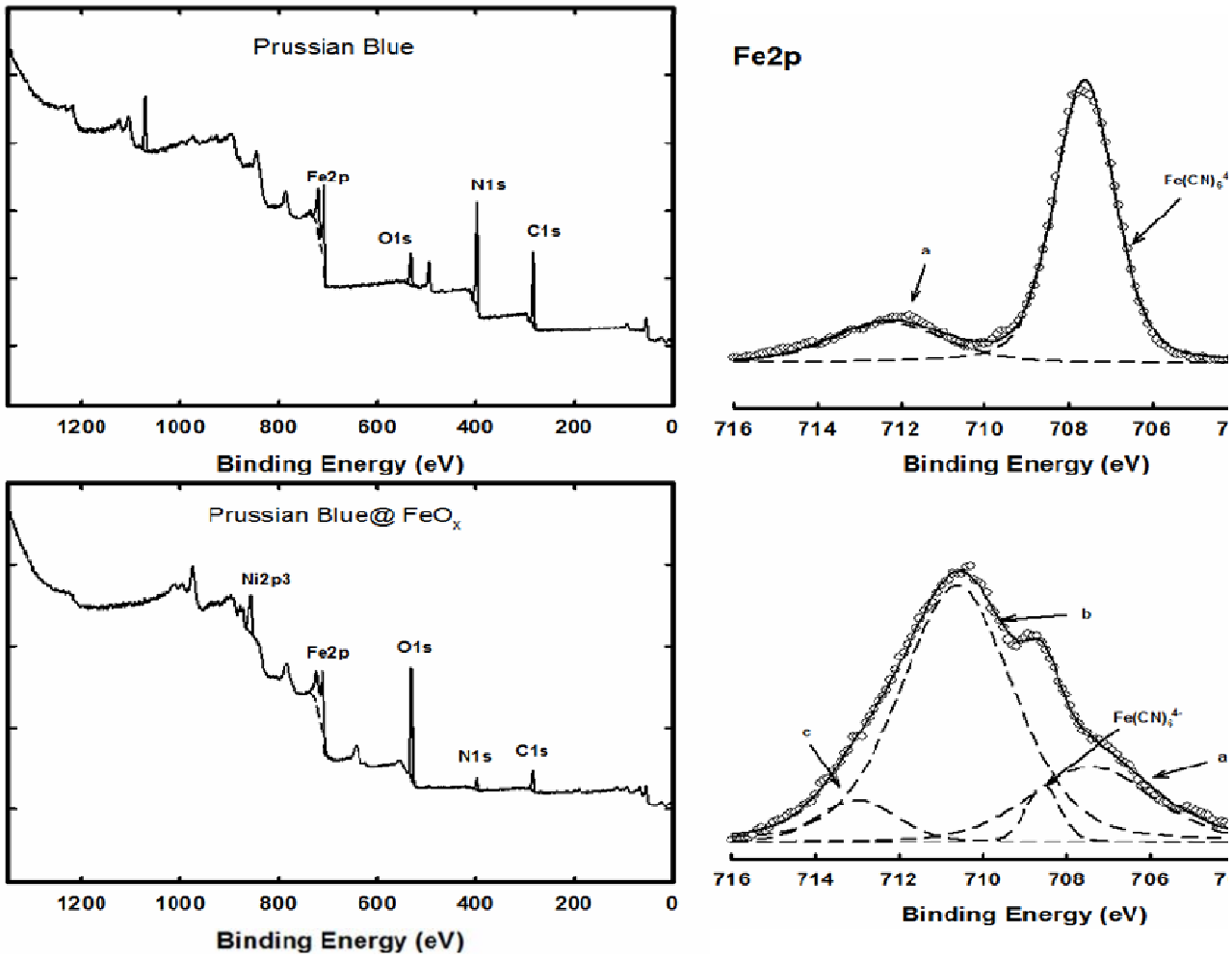

Figure 4-5: XPS region scan of the Prussian blue coated iron oxide nanoparticles showing Ni, Fe, O, N, C elements on the surface of the nanoparticles.

(a)

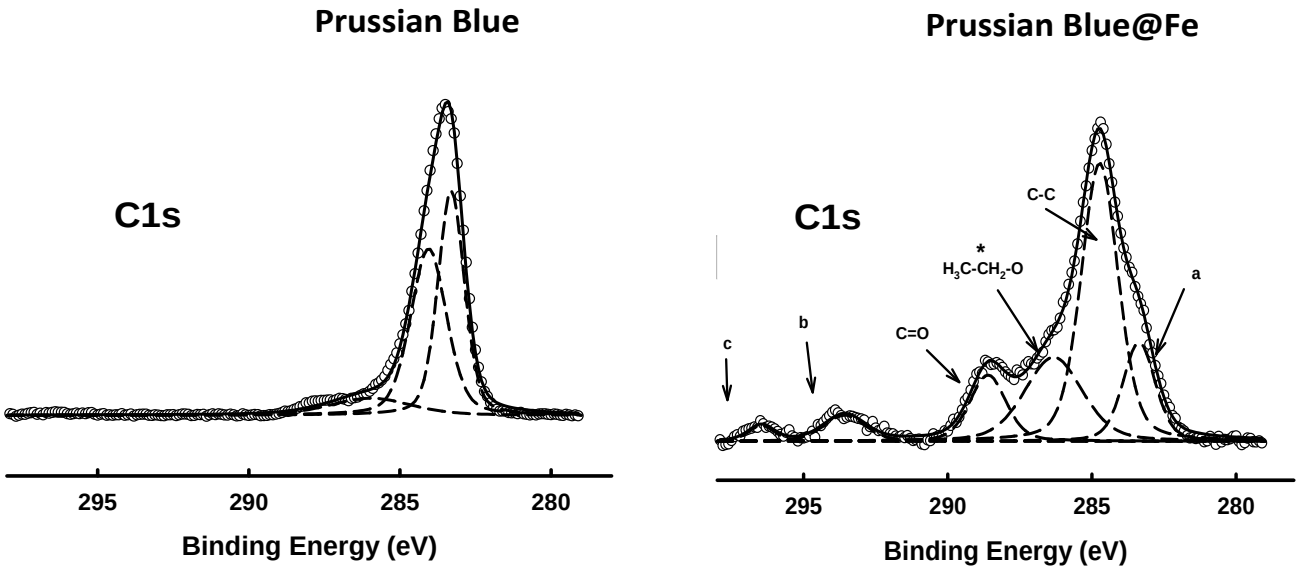

Figure 4-6: XPS regional scan of the C1s region of Prussian blue and Prussian blue coated nanoparticles. The horizontal solid line represents the base-line, the circles represents the raw data and the dashed lined represents the fitted peaks. The symbols a, b and c represents the extra peaks in the regional scan of PB coated nanoparticles when compared to the free PB.

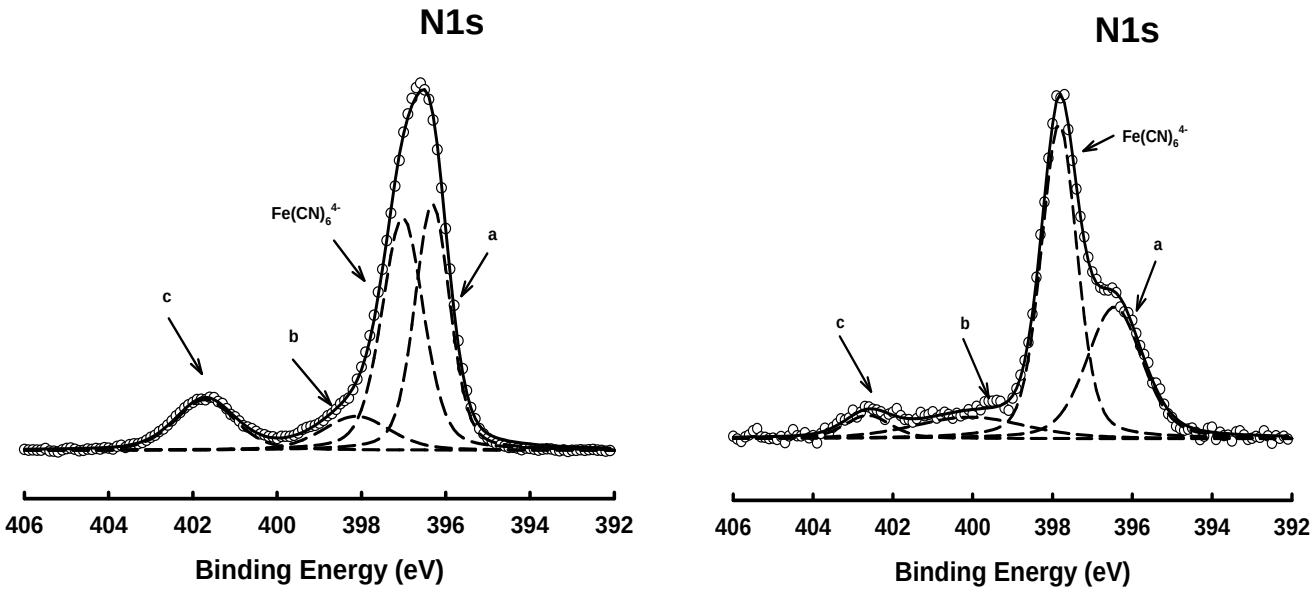

Figure 4-7: XPS regional scan of the the N1s region of Prussian blue and Prussian blue coated nanoparticles. The horizontal solid line represents the base-line, the circles represents the raw data and the dashed lined represents the fitted peaks. The symbols a, b and c represents the extra peaks in the regional scan of PB coated nanoparticles when compared to the free PB.

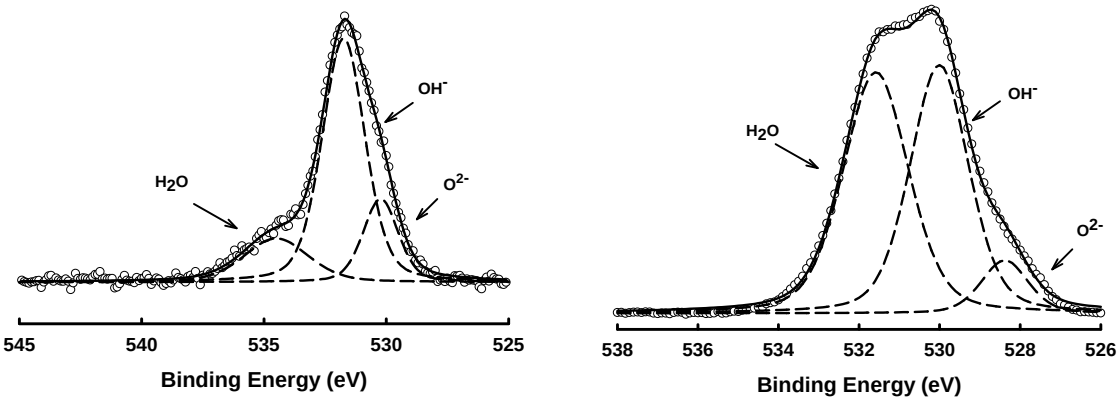

Figure 4-8: XPS regional scan of the the O1s region of Prussian blue (left) and Prussian blue coated nanoparticles (right). The horizontal solid line represents the base-line, the circles represents the raw data and the dashed lined represents the fitted peaks. The symbols a, b and c represents the extra peaks in the regional scan of PB coated nanoparticles when compared to the free PB.

An XPS survey scan in the binding energy range from 0 to 1350 eV was carried out to determine the chemical composition of the surface of the PB and PB@Fe as shown in Figure 4-5. It was found that the coated particles were consistent with pure Prussian blue and consisted of Ni, Fe, C, N, and O elements. The nickel present in the PB@Fe nanoparticles is due to the use of nickel as a passivation layer for stabilization of the iron core. The excess nickel which is seen on the surface is most likely from unreacted Ni(II) adsorbed onto the surface of the particles during the wash steps. The main differences between the PB and the PB@Fe nanoparticles are apparent in the $Fe2p_{3/2}$ spectra (see Figure 4-5). For the PB sample the most intense peak is located at 708 eV with a much smaller peak at 712 eV. For the PB@Fe sample the most intense peak is located at 711 eV with less intense peaks at 707 eV, 709 eV, and 713 eV. The 709 eV peak represent iron(II) ions coordinated by carbon atoms in $Fe^{II}(CN)_6$ groups in PB as is consistent with the literature.[191,206] An explanation of the smaller binding energy peaks is much more complicated because they could come either from nitrogen- coordinated Fe(III) ions or from unreacted iron(II/III) which adsorbed onto the surface of the PB. The binding energy at 710 eV, was reported to be from Fe(III)PB.[207-212] Fe(II) ions and iron metal range between 709-710 eV.[213] Figure 4-7 compares the regional scans of C1s, N1s and O1s of PB and PB@Fe particles. In the case of the C1s region for the coated particles, there is an extra source of carbon present such as oxyethylene and carbonyls coming from the NP surfactant. The C1s spectrum (Figure 4-6) is hard to examine due to hydrocarbons ubiquitous contamination which can come from different sources. The PB@Fe has more than just hydrocarbons on the surface. The low count rate is illustrates the presence of a

monolayer or less of impurities. The N1s spectrum for both Prussian blue and PB@Fe (Figure 4-7) have similar spectra and the respective binding energies at 397 eV and 397.82 eV correspond to $Fe(CN)_6^{4-}$.[214-216] The O1s spectra for both samples (Figure 4-8) contain 3 signals coming from O^{2-} and OH^- as well as oxygen coming from H_2O, all three species can come from surface oxides/hydroxides.[207-211,217,218] Water is also a component of PB.[214-216] The intensity difference between the two samples could be due to the synthesis and the wash steps with reverse micelles. The reaction is aqueous and the samples are washed with methanol, this could contribute to surface methanol and water. The amount of O^{2-} seems to remain constant and it is due to the surface oxide. The O^{2-}, OH^-, and H_2O binding energies at 530 eV, 532 eV, and 535 eV are in good agreement with the literature. [219]

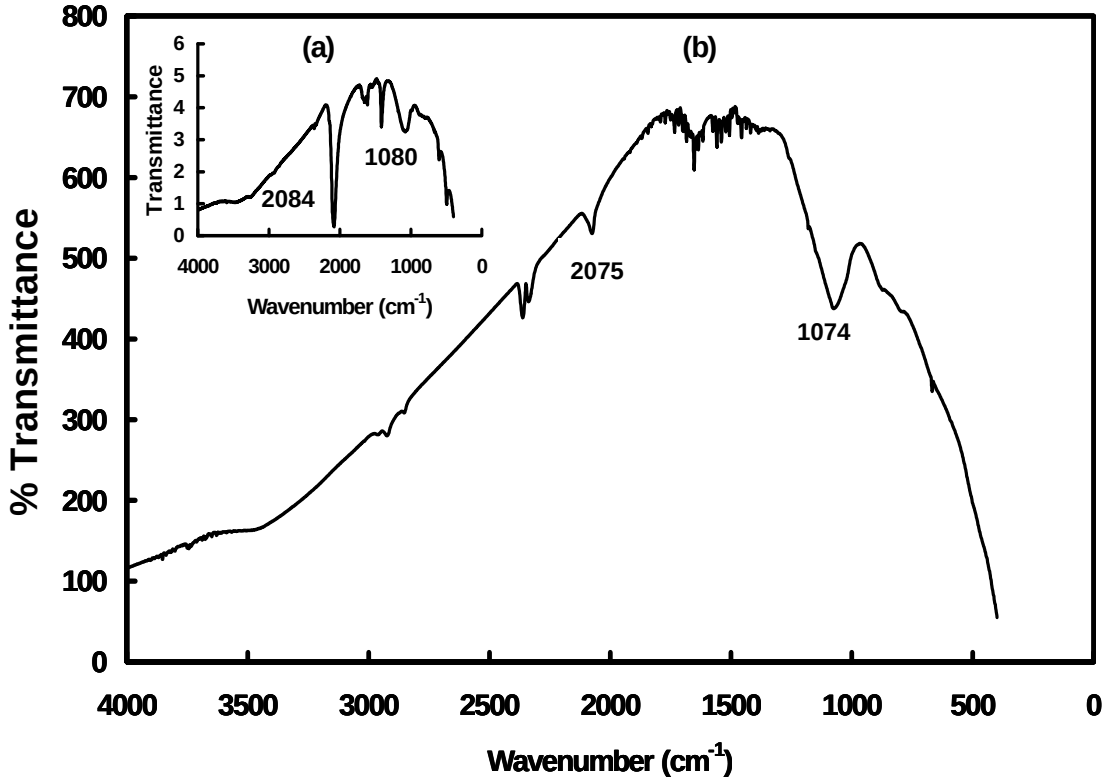

Figure 4-9: Infrared spectra of free Prussian blue (a) and Prussian blue coated iron nanoparticles (b).

Infrared spectroscopy samples were prepared by combining the PB@Fe coated nanoparticles with potassium chloride, and then grinding until uniform. Figure 4-9 compares the IR spectra of PB and of the PB coated nanoparticles, the terminal cyanide vibration frequency present at 2084 cm^{-1} for free PB, was shifted to a lower frequency at 2075 cm^{-1} for the coated particles.[220,221] In addition, the C-N stretch frequency that is at 1080 cm^{-1} present in Figure (a) was also shifted to 1074 cm^{-1} in Figure (b) and it changed from a symmetrical peak to asymmetrical one as shown in Figure (b). This shift is

attributed to the change in dipole moment of the cyanide group due to the interaction between the nitrogen in the free PB and the iron surface in the coated nanoparticles.

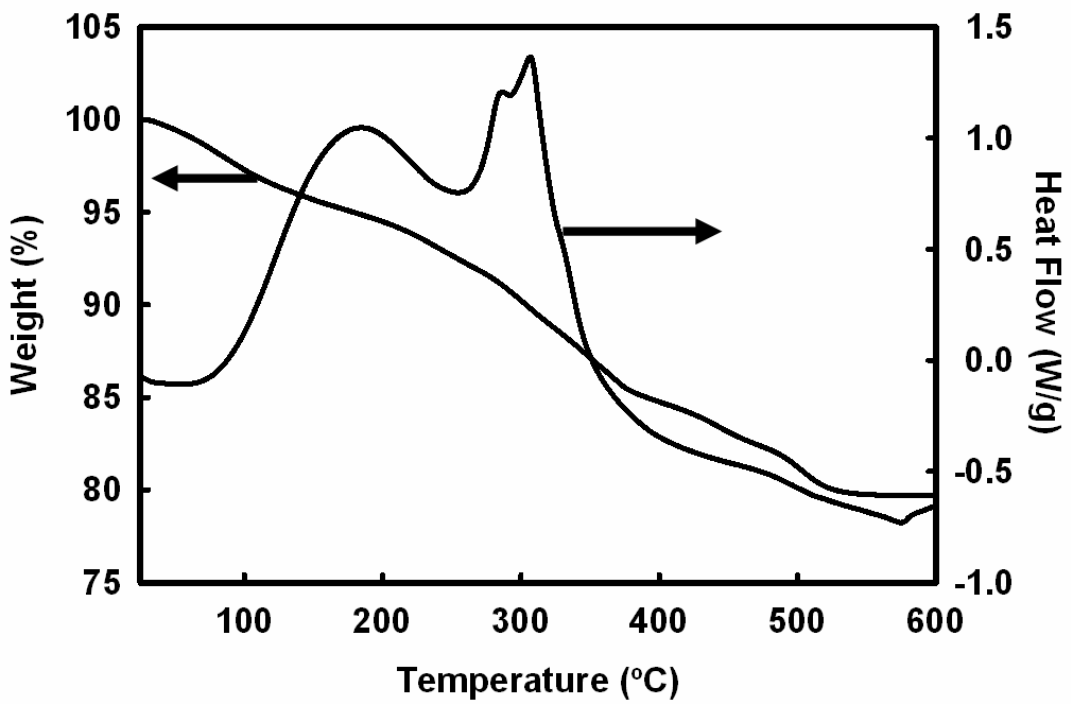

Figure 4-10: TGA-DSC data of Prussian blue coated iron nanoparticles

Figure 4-10 represents an overlay of the TGA and DSC data for the PB coated nanoparticles. The TGA measurements show four weight loss regions, the first region started at 30 °C and continued to 155°C. This temperature range is characteristic for the evaporation of water at different positions in the PB crystal structure, including zeolitic, lattice, and bounded water molecules.[222,223] The second region ranges from 230 to 373 °C, which is specific to the cyanide decomposition as reported in literature. The last two weight loss regions are less intense and take place above 400 °C. These regions could be due to the decomposition of sample impurities like hydroxide groups adsorbed to the surface of the coated nanoparticles. The DSC measurements illustrated in Figure 4-10 show two endotherms at 160 and 289 °C which correspond to the TGA decomposition temperatures of water and cyanide groups, respectively. The exotherm present above 400 °C represents crystallization event as a result of the adsorption of the hydroxide to the surface of the particles and the formation of iron oxide.

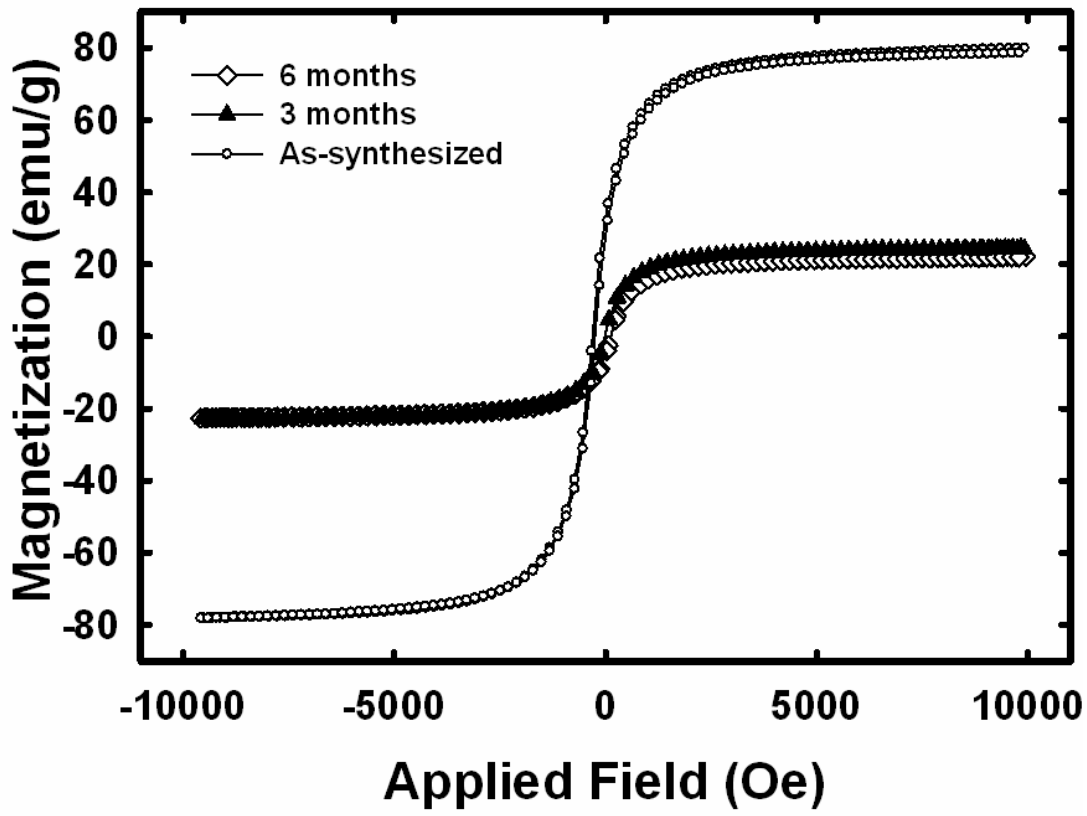

Figure 4-11: The VSM data shows the hysteresis loop curves for the as-synthesized PB coated nanoparticles. The sample was then analyzed after 3-months, and then after 6-months.

Figure 4-11 represents hysteresis loop curves for the PB coated nanoparticles at room temperature for different time periods. The saturation magnetization of the coated particles is 80 emu/ g and coercivity below 100 Oe for the as-synthesized nanoparticles. The magnetization of the coated particles dropped to 22 emu/g after three months and it remained the same after six months. This reduction in magnetization could be attributed to the oxidation of the iron core and can be explained by not have fully coated Fe nanoparticles.

V. Conclusion

In conclusion, iron nanoparticles functionalized with Prussian blue ligand was synthesized via reverse micelles method. The coated particles possess core shell morphology and are monodispersed with a narrow size distribution. The PB functionalized iron nanoparticles have both magnetic and optical properties, which make them strong potential candidates for the use in a variety of biomedical applications. Finally, it is worth mentioning that the PB@Fe nanoparticles have the highest magnetization saturation value when compared to the two previous dual mode systems.

Chapter 5: Conclusions and Future Work

I. Conclusions

Three different approaches were used to prepare dual mode nanoparticles using a previously described reverse micelle technique. Superparamagnetic Fe@FeOx core shell nanoparticles were chosen to be the magnetic component for all three dual mode systems. In the first system, 2- amino-1,3- propane diol (APD) was used as a functionalization ligand to stabilize the surface of the particles while its amino group provided a binding site for the attachment of a fluorescent probe. The functionalization reaction was carried out by dispersing the as prepared Fe@FeOx nanoparticles in ethanol and adding APD to the reaction mixture followed by sonication. The APD ligand is multifunctional and was bonded to the iron in the FeOx shell via its diol oxygen. The APD ligand can also be further functionalized by attaching a fluorescent probe such as dicarboxyl fluorescein through the formation of an amide bond with the free amino group. The stability of the APD coated particles over time was confirmed using an absorption kinetic run over 24 hours time period. The coated particles showed core shell morphology with a size range of 8-13 nm. The interaction between the hydroxyl groups of APD and the iron in the FeOx shell was verified using Infrared spectroscopy analysis (IR). In addition, matrix assisted laser desorption/ ionization time of flight (MALDI-TOF) alongside with x-ray photoelectron spectroscopy (XPS) were also used to confirm the presence of APD on the

surface of the particles. Vibrating sample magnetometer (VSM) data showed that the particles remained magnetic even after functionalization. The reduction in magnetization was a result of the organic surface coating of APD. At this point, we realized that attaching a bulky organic fluorescent probe will cause the particles' magnetization to further decrease. Therefore, our attention was directed towards inorganic semiconductor nanoparticles to be used as the optical component of the dual mode particles.

For the second system, we choose cadmium sulfide nanoparticles to be used as a fluorescent probe in an attempt to improve the optical and magnetic properties of the system. Cadmium sulfide was used to coat the iron nanoparticles by generating a shell around the metallic core. The reverse micelles synthesis was modified to incorporate the quantum dots. Two additional surfactant solutions were added to the synthesis containing aqueous cadmium acetate and sodium sulfide which were alternately added to the reaction mixture. The TEM images of the coated particles showed core shell morphology, the core consisted of alpha iron while the shell represented the CdS coating. The size of the produced CdS@Fe nanoparticles was 14 ± 3 nm. The diffraction patterns of the coated particles were in agreement with the reference diffraction patterns of alpha iron and CdS. The optical measurements were obtained using absorption and fluorescence spectroscopy. The coated particles had an emission peak at 670 nm using the excitation wavelength of 335 nm. Surface measurements using XPS confirmed the presence of the CdS shell around the magnetic iron core. Magnetic measurements using VSM showed magnetic behavior of the particles with magnetization of 16 emu/ g with coercivity below 20 Oe. The low magnetization could be do to the magnetic dilution from the CdS shell

and the thioglycerol coating CdS coated nanoparticles resulted in more reduction in the magnetization of the particles. To solve this issue, we decided to search for a suitable inorganic optical probe that is smaller in an anticipation of saving the magnetization of the particle.

Prussian blue (PB) optical probe was chosen to functionalize the surface of Fe@FeOx nanoparticles. PB was chosen for its exceptional optical properties especially its intense absorption, which eliminates the need for further functionalization with bulky optical fluorophores. PB is also very stable due to the strong field ligand present in the ferrocyanide anion of the compound. The reverse micelles technique used to prepare Fe@FeOx nanoparticles was also modified to include an additional surfactant solution containing aqueous PB. Prussian blue binds to the surface of the particles via the nitrogen of the cyanide groups resulting in stable and water dispersible particles.

Similarly to the two previous systems, variety of characterization methods was used to characterize the coated particles. X-ray powder diffraction (XRD) data showed that the diffraction patterns of the coated particles are in agreement with the reference diffraction patterns of the PB and alpha iron crystal lattice. Transmission electron microscopy (TEM) reviled particles with core shell morphology with a size of 11 ± 2 nm. The attachment of PB to the surface of the particles was confirmed using IR and XPS measurements. The TGA data presented four weight loss regions; evaporation of water at different positions in the PB crystal structure. The second region is specific to the cyanide decomposition. The last two weight loss regions are less intense and take place above 400 °C. These regions could be due to the decomposition of sample impurities such as the

hydroxide groups adsorbed on the surface of the particles. The DSC measurements showed two endotherms which correspond to the TGA decomposition temperatures of water and cyanide groups, respectively. The exotherm present above 400 °C events representing the adsorption of the hydroxide and crystallization of oxide on the surface of the particles. Finally, the magnetization saturation of the coated particles is 80 emu/ g and the coercivity is below 100 Oe. This magnetization saturation value of the PB coated particles is the highest when compared to the first two systems.

II. Future work

II.1 Ultimate potential application - In vitro and in vivo applications of all three dual mode systems

Current scientific investigations regarding the improvement of the detection methods of cancerous cells are of great importance. Conventional treatments techniques such radiation, surgery and chemotherapy have certain limitations. These drawbacks include early diagnosis, nonspecific drug distribution, suitable drug concentration in the tumor area, and the lack of capacity to observe therapeutic responses in real time.[224] In addition, present imaging systems use contrast agents that are nonspecific, highly toxic such as iodine based agents and the use radioisotopes for nuclear imaging which provide low resolution and represent a health hazard to patients and workers.[225]

For these reasons the preparation of dual mode system became a crucial part of cancer research. One example of such system was coupling paramagnetic gadolinium based contrast agent with quantum dots to enhance spatial resolution for magnetic resonance imaging (MRI).[226] In our work, we have improved such dual mode system by replacing paramagnetic gadolinium with superparamagnetic nanoparticles. High magnetization saturation is essential in guiding the biomarkers or drug to the target sites by external magnetic field. Furthermore, the system must have the ability to establish a magnetic gradient that enhances proton relaxation properties for the use in MRI imaging.[227] The large surface area of nanoparticles makes it possible to functionalize them with multiple ligands that allows for their attachment to the targeted sites of cells. We have also used three different optical probes as discussed earlier, in an attempt to address the current limitation of the conventional treatment methods of cancer.

Once the stability and magnetization measurements of our dual mode system are established, the next step is the conduction of in *vitro* experiments. Many variables need to be measured including toxicity of the particles, cell penetration, aggregation and agglomeration, optical and magnetic properties. All these parameters are important to study to ensure that the properties of the dual mode particles are still present when moved from the lab bench to the petri dish and eventually inside of live cells. For in *vitro* applications, confocal light microscopy is a good tool to show the particles fluorescence as well as their ability to penetrate inside of the cells.

In *vitro* measurements give initial indication about the dual mode systems, biocompatibility and toxicity by studying observing the cells before and after the

introduction of the particles. The particles' dispersion stability and cell penetration can be investigated by means of confocal microscopy. The effect of the drug on cancerous cells can be determined by comparing the effect of the dual mode particles on the cells before and after the attachment of a certain drug.

II.1.1 Investigate the maximum and minimum size limits of the iron the CdS shell deliver optimal optical and magnetic properties

The size of the iron core in our current work is approximately 12 nm and CdS shell size is 2 nm. The magnetization saturation was decreased as a result of mass dilution caused by the quantum dots shell. Investigating the change in magnetic and optical properties as the size of the core and shell changes would be a useful information to obtain in order to enhance the CdS@Fe dual mode system. Such experiment would consist of two main parts; the first would be studying the effect of increasing the size of the iron core on the particle's magnetization saturation while keeping the size of the shell constant. It is worth noting that the increase in size is limited to the superparamagnetism critical size range as well as the size of cells. Once a favorable core size is selected, modification of the size of the CdS shell can be done to reach optimal optical properties. Many parameters must be considered while investigating the size of the core and the shell of this dual mode system such as the size limits of superparamagnetism, fluorescence quenching and the size of the core- shell nanoparticles after stabilization with thioglycerol.

II.1.2 Investigate the ability to replace the CdS shell with CdS/ZnS shell to enhance the fluorescence

ZnS has been used to passivate the surface of CdS quantum dots. The formation of CdS/ZnS core shell quantum dots resulted in high quantum efficiencies and enhanced photoluminescence emission. This is due to the ZnS charge and size compatibility with the CdS quantum dots which leads to an enhancement of the band edge emission.[228,229]

This modification of the optical properties of the CdS@Fe dual made system could be tested using iron particles of the chosen size (from I). The CdS shell would be replaced by CdS/Shell but the thickness will remain constant in anticipation of saving the magnetic properties of the particles. It would be interesting to study how CdS/ZnS shell would behave when surrounding a metallic iron core.

II.2 Study of the photomagnetization properties of Prussian blue@ Fe nanoparticles

As discussed in chapter four, Prussian blue magnetization can interchange from diamagnetic to paramagnetic upon irradiation with certain wavelength. PB by itself has low Curie temperature of 5.5 K which is unfavorable for technological applications such as data storage and molecular electronics. Currently, this problem is solved by introducing different ions in the place of Fe(III) in Prussian blue compound producing Prussian blue analogues. The attachment of PB to superparamagnetic iron nanoparticles

could affect the photomagnetic behavior and/ or the curie temperature of this compound leading to the use of PB in larger number of applications. Field cooled (FC) or zero field cooled (ZFC) measurements could be done using the SQUID instrument to investigate the affect of attaching PB to superparamagnetic iron nanoparticles on the Curie temperature. The effect of irradiation on the magnetic properties of PB@Fe nanoparticles can be measured using SQUID. The magnetization saturation, Curie temperature, corecivity and remnant magnetization should be measured before and after irradiation.

List of References

List of References

(1) Padovani, S.; Borgia, I.; Brunetti, B.; Sgamellotti, A.; Giulivi, A.; D'Acapito, F.; Mazzoldi, P.; Sada, C.; Battaglin, G. *Appl. Phys. A* **2004**, *79*, 229-233.

(2) Schaffer, B.; Riegler, K.; Kothleitner, G.; Grogger, W.; Hofer, F. *Micron* **2009**, *40*, 269-273.

(3) Lowry, M. S.; Hubble, D. R.; Wressell, A. L.; Vratsanos, M. S.; Pepe, F. R.; Hegedus, C. R. *J. Coat. Tech. Res.* **2008**, *5*, 233-239.

(4) Gerberich, W. W.; Mook, W. M.; Perrey, C. R.; Carter, C. B.; Baskes, M. I.; Mukherjee, R.; Gidwani, A.; Heberlein, J.; McMurry, P. H.; Girshick, S. L. *Journal of the Mechanics and Physics of Solids* **2003**, *51*, 979-992.

(5) Liu, H. P.; Ye, T.; Mao, C. D. *Angewandte Chemie-International Edition* **2007**, *46*, 6473-6475.

(6) Zhou, M.; Chang, S. D.; Grover, C. P. *Optics Express* **2004**, *12*, 2925-2931.

(7) Akthakul, A.; Hochbaum, A. I.; Stellacci, F.; Mayes, A. M. *Adv. Mater.* **2005**, *17*, 532-535.

(8) Burda, C.; Chen, X. B.; Narayanan, R.; El-Sayed, M. A. *Chemical Reviews* **2005**, *105*, 1025-1102.

(9) Dmitrii, F.; Rosei, F. *Angew. Chem. Int. Ed.* **2007**, *46*, 6006-6008.

(10) Latham, A. H.; Williams, M. E. *Accounts of Chemical Research* **2008**, *41*, 411-420.

(11) Wang, Z. L. *Advanced Materials* **1998**, *10*, 13-+.

(12) Min, Y. J.; Akbulut, M.; Kristiansen, K.; Golan, Y.; Israelachvili, J. *Nature Materials* **2008**, *7*, 527-538.

(13) Murphy, C. J.; San, T. K.; Gole, A. M.; Orendorff, C. J.; Gao, J. X.; Gou, L.; Hunyadi, S. E.; Li, T. *Journal of Physical Chemistry B* **2005**, *109*, 13857-13870.

(14) O'Farrell, N.; Houlton, A.; Horrocks, B. R. *International Journal of Nanomedicine* **2006**, *1*, 451-472.

(15) Yu, X. F.; Chen, L. D.; Deng, Y. L.; Li, K. Y.; Wang, Q. Q.; Li, Y.; Xiao, S.; Zhou, L.; Luo, X.; Liu, J.; Pang, D. W. *Journal of Fluorescence* **2007**, *17*, 243-247.

(16) Zeng, H.; Rice, P. M.; Wang, S. X.; Sun, S. H. *J. Amer. Chem. Soc.* **2004**, *126*, 11458-11459.
(17) Mottet, C.; Rossi, G.; Baletto, F.; Ferrando, R. *Physical Review Letters* **2005**, *95*.
(18) Rossi, G.; Rapallo, A.; Mottet, C.; Fortunelli, A.; Baletto, F.; Ferrando, R. *Physical Review Letters* **2004**, *93*.
(19) Astruc, D. *Nanoparticles and Catalysis*; WILEY-VCH Verlag GmbH & Co. KGaA, Weinheim, 2008.
(20) Johnson, B. F. G. *Top. Catal.* **2003**, *24*, 147-159.
(21) Verma, A.; Rotello, V. M. *Chemical Communications* **2005**, 303-312.
(22) Abu-Reziq, R.; Wang, D.; Post, M.; Alper, H. *Adv. Syn. Catal.* **2007**, *349*, 2145-2150.
(23) Smith, A. M.; Gao, X. H.; Nie, S. M. *Photochemistry and Photobiology* **2004**, *80*, 377-385.
(24) Dreybrodt, J.; Forchel, A.; Reithmaier, J. P. *Physical Review B* **1993**, *48*, 14741-14744.
(25) Tews, M. *Annalen Der Physik* **2004**, *13*, 249-304.
(26) Zeng, Z. Y.; Xiang, Y.; Zhang, L. D. *European Physical Journal B* **2000**, *17*, 699-705.
(27) Unni, C.; Philip, D.; Gopchandran, K. G. *Spectrochim. Acta, Part A* **2008**, *71*, 1402-1407.
(28) Eustis, S.; El-Sayed, M. A. *Chemical Society Reviews* **2006**, *35*, 209-217.
(29) Abdullah, A.; Annapoorni, S. 2005, p 815-819.
(30) Alschinger, M.; Maniak, M.; Stietz, F.; Vartanyan, T.; Trager, F. *Applied Physics B-Lasers and Optics* **2003**, *76*, 771-774.
(31) Hubenthal, F.; Ziegler, T.; Hendrich, C.; Alschinger, M.; Trager, F. 2005, p 165-168.
(32) Winter, J. 2007.
(33) Cai, W. B.; Niu, G.; Chen, X. Y. *Current Pharmaceutical Design* **2008**, *14*, 2943-2973.
(34) Chan, W. C. W. *Biology of Blood and Marrow Transplantation* **2006**, *12*, 87-91.
(35) Jaiswal, J. K.; Goldman, E. R.; Mattoussi, H.; Simon, S. M. *Nature Methods* **2004**, *1*, 73-78.
(36) Bhattacharya, P.; Ghosh, S.; Stiff-Roberts, A. D. *Annual Review of Materials Research* **2004**, *34*, 1-40.
(37) D'Amico, I.; Fossi, F. *Applied Physics Letters* **2002**, *81*, 5213-5215.
(38) Jacak, L.; Krasnyj, J.; Wojs, A. *Physica B* **1997**, *229*, 279-293.

(39) Mathew, D. S.; Juang, R. S. *Chemical Engineering Journal* **2007**, *129*, 51-65.

(40) Sun, S. H. *Adv. Mater.* **2006**, *18*, 393-403.

(41) Pankhurst, Q. A.; Connolly, J.; Jones, S. K.; Dobson, J. *Journal of Physics D-Applied Physics* **2003**, *36*, R167-R181.

(42) Batlle, X.; Labarta, A. *Journal of Physics D-Applied Physics* **2002**, *35*, R15-R42.

(43) Tartaj, P. *European Journal of Inorganic Chemistry* **2009**, 333-343.

(44) Bedanta, S.; Kleemann, W. *Journal of Physics D-Applied Physics* **2009**, *42*.

(45) Xu, C. J.; Sun, S. H. *Polym. Int.* **2007**, *56*, 821-826.

(46) He, Y. Q.; Li, X. G.; Swihart, M. T. *Chemistry of Materials* **2005**, *17*, 1017-1026.

(47) Hergt, R.; Hiergeist, R.; Hilger, I.; Kaiser, W. A.; Lapatnikov, Y.; Margel, S.; Richter, U. *J. Magn. Magn. Mater.* **2004**, *270*, 345-357.

(48) Hilger, I.; Hergt, R.; Kaiser, W. A. *Journal of Magnetism and Magnetic Materials* **2005**, *293*, 314-319.

(49) Zeng, Q.; Baker, I.; Loudis, J. A.; Liao, Y.; Hoopes, P. J.; Weaver, J. B. *Appl. Phys. Lett.* **2007**, *90*.

(50) Chavanpatil, M. D.; Khdair, A.; Panyam, J. *Pharmaceut. Res.* **2007**, *24*, 803-810.

(51) Lee, H.; Shao, H. P.; Huang, Y. Q.; Kwak, B. 2005, p 4102-4104.

(52) Brenner, D. E.; Nortnolle, D. P. *Cancer epidem. Biomar.* **2007**, *16*, 1918-1920.

(53) Choi, Y. E.; Kwak, J. W.; Park, J. W. *Sensors*, *10*, 428-455.

(54) Zhang, Q.; Iwakuma, N.; Sharma, P.; Moudgil, B. M.; Wu, C.; McNeill, J.; Jiang, H.; Grobmyer, S. R. *Nanotechnol.* **2009**, *20*.

(55) Qian, X. M.; Peng, X. H.; Ansari, D. O.; Yin-Goen, Q.; Chen, G. Z.; Shin, D. M.; Yang, L.; Young, A. N.; Wang, M. D.; Nie, S. M. *Nat. Biotechnol.* **2008**, *26*, 83-90.

(56) Gao, X. H.; Cui, Y. Y.; Levenson, R. M.; Chung, L. W. K.; Nie, S. M. *Nat. Biotechnol.* **2004**, *22*, 969-976.

(57) Wang, D. S.; He, J. B.; Rosenzweig, N.; Rosenzweig, Z. *Nano Lett.* **2004**, *4*, 409-413.

(58) Shultz, M. D.; Calvin, S.; Fatouros, P. P.; Morrison, S. A.; Carpenter, E. E. *J. Magnet. Magnet. Mater.* **2007**, *311*, 464-468.

(59) Gupta, A. K.; Wells, S. *Ieee Trans. Nanobiosci.* **2004**, *3*, 66-73.

(60) Lee, J. H.; Jun, Y. W.; Yeon, S. I.; Shin, J. S.; Cheon, J. *Angew. Chem. Int. Ed.* **2006**, *45*, 8160-8162.

(61) Liong, M.; Lu, J.; Kovochich, M.; Xia, T.; Ruehm, S. G.; Nel, A. E.; Tamanoi, F.; Zink, J. I. *Acs Nano* **2008**, *2*, 889-896.

(62) Lam, U. T.; Mammucari, R.; Suzuki, K.; Foster, N. R. *Industrial & Engineering Chemistry Research* **2008**, *47*, 599-614.

(63) Tartaj, P.; Morales, M. D.; Veintemillas-Verdaguer, S.; Gonzalez-Carreno, T.; Serna, C. J. *Journal of Physics D-Applied Physics* **2003**, *36*, R182-R197.

(64) Hilger, I.; Fruhauf, K.; Andra, W.; Hiergeist, R.; Hergt, R.; Kaiser, W. A. *Academic Radiology* **2002**, *9*, 198-202.

(65) Wormuth, K. *Journal of Colloid and Interface Science* **2001**, *241*, 366-377.

(66) Dobson, J. *Drug Development Research* **2006**, *67*, 55-60.

(67) Sonvico, F.; Dubernet, C.; Colombo, P.; Couvreur, P. *Current Pharmaceutical Design* **2005**, *11*, 2091-2105.

(68) Mornet, S.; Vasseur, S.; Grasset, F.; Duguet, E. *J. Mater. Chem.* **2004**, *14*, 2161-2175.

(69) Gupta, A. K.; Gupta, M. *Biomaterials* **2005**, *26*, 3995-4021.

(70) Somaskandan, K.; Veres, T.; Niewczas, M.; Simard, B. *New Journal of Chemistry* **2008**, *32*, 201-209.

(71) Bertorelle, F.; Wilhelm, C.; Roger, J.; Gazeau, F.; Menager, C.; Cabuil, V. *Langmuir* **2006**, *22*, 5385-5391.

(72) Srinivasan, B.; Huang, X. F. *Chirality* **2008**, *20*, 265-277.

(73) Sun, C.; Lee, J. S. H.; Zhang, M. Q. *Advanced Drug Delivery Reviews* **2008**, *60*, 1252-1265.

(74) Zhu, L. Z.; Ma, J. W.; Jia, N. Q.; Zhao, Y.; Shen, H. B. *Colloids Surf. B* **2009**, *68*, 1-6.

(75) Ge, Y. Q.; Zhang, Y.; He, S. Y.; Nie, F.; Teng, G. J.; Gu, N. *Nanoscale Res. Lett.* **2009**, *4*, 287-295.

(76) Eastoe, J.; Hollamby, M. J.; Hudson, L. *Adv. Colloid Interface Sci.* **2006**, *128*, 5-15.

(77) Herlin-Boime, N.; Mayne-L'Hermite, M.; Reynaud, C. *Annales De Chimie-Science Des Materiaux* **2006**, *31*, 295-315.

(78) Hua, C. C.; Zakaria, S.; Farahiyan, R.; Khong, L. T.; Nguyen, K. L.; Abdullah, M.; Ahmad, S. *Sains Malaysiana* **2008**, *37*, 389-394.

(79) Kriwet, B.; Walter, E.; Kissel, T. *Journal of Controlled Release* **1998**, *56*, 149-158.

(80) Raula, J.; Kuivanen, A.; Laehde, A.; Jiang, H.; Antopolsky, M.; Kansikas, J.; Kauppinen, E. I. *Journal of Aerosol Science* **2007**, *38*, 1172-1184.

(81) Uskokovic, V.; Drofenik, M. *Surf. Rev. Lett.* **2005**, *12*, 239-277.

(82) Murray, C. B.; Norris, D. J.; Bawendi, M. G. *Journal of the American Chemical Society* **1993**, *115*, 8706-8715.

(83) Beji, Z.; Ben Chaabane, T.; Smiri, L. S.; Ammar, S.; Fievet, F.; Jouini, N.; Greneche, J. M. *Physica Status Solidi a-Applications and Materials Science* **2006**, *203*, 504-512.

(84) Couto, G. G.; Klein, J. J.; Schreiner, W. H.; Mosca, D. H.; de Oliveira, A. J. A.; Zarbin, A. J. G. *Journal of Colloid and Interface Science* **2007**, *311*, 461-468.

(85) Rogach, A. L.; Kornowski, A.; Gao, M. Y.; Eychmuller, A.; Weller, H. *J. Phys. Chem. B* **1999**, *103*, 3065-3069.

(86) Aslam, M.; Schultz, E. A.; Sun, T.; Meade, T.; Dravid, V. P. *Crystal Growth & Design* **2007**, *7*, 471-475.

(87) Park, J. Y.; Oh, S. G.; Ha, B. H. *Korean Journal of Chemical Engineering* **2001**, *18*, 215-219.

(88) Cizeron, J.; Pileni, M. P. *Journal of Physical Chemistry* **1995**, *99*, 17410-17416.

(89) Herrera, A. P.; Resto, O.; Briano, J. G.; Rinaldi, C. 2005, p S618-S625.

(90) Pileni, M. P. *J. Phys. Chem.* **1993**, *97*, 6961-6973.

(91) Carpenter, E. E.; Calvin, S.; Stroud, R. M.; Harris, V. G. *Chemistry of Materials* **2003**, *15*, 3245-3246.

(92) Fan, M. D.; Yuan, P.; Zhu, J. X.; Chen, T. H.; Yuan, A. H.; He, H. P.; Chen, K. M.; Liu, D. *Journal of Magnetism and Magnetic Materials* **2009**, *321*, 3515-3519.

(93) Wang, C. M.; Baer, D. R.; Thomas, L. E.; Amonette, J. E.; Antony, J.; Qiang, Y.; Duscher, G. *Journal of Applied Physics* **2005**, *98*, 7.

(94) Lu, A. H.; Salabas, E. L.; Schuth, F. *Angewandte Chemie-International Edition* **2007**, *46*, 1222-1244.

(95) Bonnemann, H.; Brijoux, W.; Brinkmann, R.; Matoussevitch, N.; Waldofner, N.; Palina, N.; Modrow, H. *Inorganica Chimica Acta* **2003**, *350*, 617-624.

(96) Boyen, H. G.; Kastle, G.; Zurn, K.; Herzog, T.; Weigl, F.; Ziemann, P.; Mayer, O.; Jerome, C.; Moller, M.; Spatz, J. P.; Garnier, M. G.; Oelhafen, P. *Advanced Functional Materials* **2003**, *13*, 359-364.

(97) Kang, K.; Choi, J.; Nam, J. H.; Lee, S. C.; Kim, K. J.; Lee, S. W.; Chang, J. H. *Journal of Physical Chemistry B* **2009**, *113*, 536-543.

(98) Qiu, J. S.; Li, Y. F.; Wang, Y. P.; An, Y. L.; Zhao, Z. B.; Zhou, Y.; Li, W. *Fuel Processing Technology* **2004**, *86*, 267-274.

(99) Zhou, W. L.; Carpenter, E. E.; Lin, J.; Kumbhar, A.; Sims, J.; O'Connor, C. J. *European Physical Journal D* **2001**, *16*, 289-292.

(100) Sun, X. C. *J. Dispersion Sci. Technol.* **2003**, *24*, 557-567.

(101) Wang, L. Y.; Luo, J.; Fan, Q.; Suzuki, M.; Suzuki, I. S.; Engelhard, M. H.; Lin, Y. H.; Kim, N.; Wang, J. Q.; Zhong, C. J. *J. Phys. Chem. B* **2005**, *109*, 21593-21601.

(102) Zhou, W. L.; Carpenter, E. E.; Lin, J.; Kumbhar, A.; Sims, J.; O'Connor, C. J. *Eur. Phys. J. D* **2001**, *16*, 289-292.

(103) Di Marco, M.; Guilbert, I.; Port, M.; Robic, C.; Couvreur, P.; Dubernet, C. *International Journal of Pharmaceutics* **2007**, *331*, 197-203.

(104) Qin, Y.; Fichthorn, K. A. *Journal of Chemical Physics* **2003**, *119*, 9745-9754.

(105) Chen, C. C.; Kuo, P. L.; Cheng, Y. C. *Nanotechnology* **2009**, *20*, 7.

(106) Lalatonne, Y.; Richardi, J.; Pileni, M. P. *Nat. Mater.* **2004**, *3*, 121-125.

(107) Bonnemann, H.; Richards, R. M. *Eur. J. Inorg. Chem.* **2001**, 2455-2480.

(108) Laaksonen, T.; Ahonen, P.; Johans, C.; Kontturi, K. *Chemphyschem* **2006**, *7*, 2143-2149.

(109) Zhang, Y.; Yang, M.; Portney, N. G.; Cui, D. X.; Budak, G.; Ozbay, E.; Ozkan, M.; Ozkan, C. S. *Biomedical Microdevices* **2008**, *10*, 321-328.

(110) Qiao, R. R.; Yang, C. H.; Gao, M. Y. *Journal of Materials Chemistry* **2009**, *19*, 6274-6293.

(111) Huang, K. C.; Ehrman, S. H. *Langmuir* **2007**, *23*, 1419-1426.

(112) Binder, W. H.; Weinstabl, H.; Sachsenhofer, R. *J. Nanomater.* **2008**.

(113) Frey, N. A.; Peng, S.; Cheng, K.; Sun, S. H. *Chemical Society Reviews* **2009**, *38*, 2532-2542.

(114) Kohler, N.; Fryxell, G. E.; Zhang, M. Q. *J. Amer. Chem. Soci.* **2004**, *126*, 7206-7211.

(115) Boyer, C.; Bulmus, V.; Priyanto, P.; Teoh, W. Y.; Amal, R.; Davis, T. P. *Journal of Materials Chemistry* **2009**, *19*, 111-123.

(116) Maurizi, L.; Bisht, H.; Bouyer, F.; Millot, N. *Langmuir* **2009**, *25*, 8857-8859.

(117) Mohapatra, S.; Pramanik, P. *Colloids and Surfaces a-Physicochemical and Engineering Aspects* **2009**, *339*, 35-42.

(118) Robinson, I.; Alexander, C.; Tung, L. D.; Fernig, D. G.; Thanh, N. T. K. *Journal of Magnetism and Magnetic Materials* **2009**, *321*, 1421-1423.

(119) Jun, Y. W.; Huh, Y. M.; Choi, J. S.; Lee, J. H.; Song, H. T.; Kim, S.; Yoon, S.; Kim, K. S.; Shin, J. S.; Suh, J. S.; Cheon, J. *Journal of the American Chemical Society* **2005**, *127*, 5732-5733.

(120) Chen, Z. P.; Zhang, Y.; Zhang, S.; Xia, J. G.; Liu, J. W.; Xu, K.; Gu, N. *Colloids and Surfaces a-Physicochemical and Engineering Aspects* **2008**, *316*, 210-216.

(121) Peng, H.; Zhang, X.; Huang, K. X.; Xu, H. B. *Journal of Wuhan University of Technology-Materials Science Edition* **2008**, *23*, 480-485.

(122) Xu, C. J.; Xu, K. M.; Gu, H. W.; Zheng, R. K.; Liu, H.; Zhang, X. X.; Guo, Z. H.; Xu, B. *Journal of the American Chemical Society* **2004**, *126*, 9938-9939.

(123) Shultz, M. D.; Reveles, J. U.; Khanna, S. N.; Carpenter, E. E. *Journal of the American Chemical Society* **2007**, *129*, 2482-2487.

(124) Semwogerere, D.; Weeks, E. R. In *Encyclo. biomater. biomed. engineer.*; Taylor and Francis: Atlanta, 2005.

(125) Electronics, K. P.; Koninklijke Philips Electronics N.V.: 2008.

(126) Peterson, C. *2001*, *3*.

(127) Nicolet, T. Madison, 2001.

(128) *Srface Analysis*
The Principal Techniques; 2 ed.; Vickerman, J. C.; Gilmore, I. S., Eds.; John Wiley & Sons Ltd, 2009.

(129) Department, S. P.

(130) Predoi, D. *Digest Journal of Nanomaterials and Biostructures* **2007**, *2*, 169-173.

(131) Grabchev, I.; Petkov, C.; Bojinov, V. *Dyes. Pigm.* **2004**, *62*, 229-234.

(132) d'Avray, A. T. D.; Carpenter, E. E.; O'Connor, C. J.; Cole, R. B. *Europ. Mass Spec.* **1998**, *4*, 441-449.

(133) Tao, K.; Dou, H. J.; Sun, K. *Chemistry of Materials* **2006**, *18*, 5273-5278.
(134) Morales, M. A.; Jain, T. K.; Labhasetwar, V.; Leslie-Pelecky, D. L. *J. Appl. Phys.* **2005**, *97*.
(135) Fang, F. F.; Choi, H. J.; Seo, Y. *ACS Appl. Mater. Interfaces*, *2*, 54-60.
(136) Prozorov, T.; Prozorov, R.; Gedanken, A. *Adv. Mater.* **1998**, *10*, 1529-+.
(137) Michaels, M. A.; Sherwood, S.; Kidwell, M.; Allsbrook, M. J.; Morrison, S. A.; Rutan, S. C.; Carpenter, E. E. *J. Colloid Interface Sci.* **2007**, *311*, 70-76.
(138) Walling, M. A.; Novak, J. A.; Shepard, J. R. E. *Int. J. Mol. Sci.* **2009**, *10*, 441-491.
(139) Merkoci, A.; Marin, S.; Castaneda, M. T.; Pumera, M.; Ros, J.; Alegret, S. *Nanotechnology* **2006**, *17*, 2553-2559.
(140) Merkoci, A. *Febs Journal* **2007**, *274*, 310-316.
(141) Dyrdal, A.; Dugaev, V. K.; Barnas, J. *Epl* **2009**, *85*.
(142) Hezinger, A. F. E.; Tessmar, J.; Gopferich, A. *Eur. J. Pharm. Biopharm.* **2008**, *68*, 138-152.
(143) Tsuzuki, T.; McCormick, P. G. *Appl. Phys. A* **1997**, *65*, 607-609.
(144) Jolivet, J. P.; Cassaignon, S.; Chaneac, C.; Chiche, D.; Tronc, E. 2008, p 299-305.
(145) Parak, W. J.; Pellegrino, T.; Plank, C. *Nanotechnology* **2005**, *16*, R9-R25.
(146) Pickett, N. L.; O'Brien, P. *Chemical Record* **2001**, *1*, 467-479.
(147) Pattani, V. P.; Li, C. F.; Desai, T. A.; Vu, T. Q. *Biomed. Microdevices* **2008**, *10*, 367-374.
(148) Blow, N. *Nature* **2008**, *456*, 825-830.
(149) Crut, A.; Geron-Landre, B.; Bonnet, I.; Bonneau, S.; Desbiolles, P.; Escude, C. *Nucleic Acids Research* **2005**, *33*.
(150) Goldman, E. R.; Medintz, I. L.; Mattoussi, H. *Analyt. Bioanal. Chem.* **2006**, *384*, 560-563.
(151) Juzenas, P.; Chen, W.; Sun, Y. P.; Coelho, M. A. N.; Generalov, R.; Generalova, N.; Christensen, I. L. *Adv. Drug Delivery Rev.* **2008**, *60*, 1600-1614.
(152) Smith, A. M.; Dave, S.; Nie, S. M.; True, L.; Gao, X. H. *Expert Rev. Mol. Diagn.* **2006**, *6*, 231-244.
(153) Michalet, X.; Pinaud, F. F.; Bentolila, L. A.; Tsay, J. M.; Doose, S.; Li, J. J.; Sundaresan, G.; Wu, A. M.; Gambhir, S. S.; Weiss, S. *Science* **2005**, *307*, 538-544.
(154) Shin, S. K.; Yoon, H. J.; Jung, Y. J.; Park, J. W. *Curr. Opin. Chem. Biol.* **2006**, *10*, 423-429.
(155) Smith, A. M.; Duan, H. W.; Mohs, A. M.; Nie, S. M. *Adv. Drug Delivery Rev.* **2008**, *60*, 1226-1240.
(156) Xing, Y.; Smith, A. M.; Agrawal, A.; Ruan, G.; Nie, S. *Inter. J. Nanomed.* **2006**, *1*, 473-481.
(157) Shi, W. L.; Ma, X. Y. *Biomed. Mater.* **2006**, *1*, 81-84.
(158) Weng, J. F.; Ren, J. C. *Curr. Med. Chem.* **2006**, *13*, 897-909.
(159) Yu, W. W.; Chang, E.; Drezek, R.; Colvin, V. L. *Biochem. Biophys. Res. Commun.* **2006**, *348*, 781-786.

(160) Azzazy, H. M. E.; Mansour, M. M. H. *Clinica Chimica Acta* **2009**, *403*, 1-8.

(161) Goldman, E. R.; Medintz, I. L.; Mattoussi, H. *Analytical and Bioanalytical Chemistry* **2006**, *384*, 560-563.

(162) Smith, A. M.; Ruan, G.; Rhyner, M. N.; Nie, S. M. *Ann. Biomed. Eng.* **2006**, *34*, 3-14.

(163) Thakur, D.; Deng, S.; Baldet, T.; Winter, J. O. *Nanotechnology* **2009**, *20*.

(164) Yu, X. G.; Wan, J. Q.; Shan, Y.; Chen, K. Z.; Han, X. D. *Chem. Mater.* **2009**, *21*, 4892-4898.

(165) Arora, S.; Manoharan, S. S. *J. Phys. Chem. Solids* **2007**, *68*, 1897-1901.

(166) Carpenter, E. E.; Calvin, S.; Stroud, R. M.; Harris, V. G. *Chem. Mater.* **2003**, *15*, 3245-3246.

(167) Radwan, F. N.; Carroll, K. J.; Carpenter, E. E. *J. Appl. Phys.*, *107*.

(168) Chen, Y. F.; Rosenzweig, Z. *Anal. Chem.* **2002**, *74*, 5132-5138.

(169) Hota, G.; Idage, S. B.; Khilar, K. C. *Colloids Surf., A* **2007**, *293*, 5-12.

(170) Khomane, R. B.; Manna, A.; Mandale, A. B.; Kulkarni, B. D. *Langmuir* **2002**, *18*, 8237-8240.

(171) Kumar, A.; Mandale, A. B.; Sastry, M. *Langmuir* **2000**, *16*, 9299-9302.

(172) Stoev, M.; Katerski, A. *J. Mater. Chem.* **1996**, *6*, 377-380.

(173) Stoev, M. D.; Touskova, J.; Tousek, J. *Thin Solid Films* **1997**, *299*, 67-71.

(174) Seals, R. D.; Alexande.R; Taylor, L. T.; Dillard, J. G. *Inorg. Chem.* **1973**, *12*, 2485-2487.

(175) Agostinelli, E.; Battistoni, C.; Fiorani, D.; Mattogno, G. *Journal of Physics and Chemistry of Solids* **1989**, *50*, 269-272.

(176) Volmer, M.; Stratmann, M.; Viefhaus, H. *Surface and Interface Analysis* **1990**, *16*, 278-282.

(177) Bodie Douglas, D. M., John Alexander *Cocepts and Models of Inorganic Chemistry*; John Wiley and sons, 1994.

(178) Buser, H. J.; Schwarzenbach, D.; Petter, W.; Ludi, A. *Inorg. Chem.* **1977**, *16*, 2704-2710.

(179) Itaya, K.; Uchida, I.; Neff, V. D. *Acc. Chem. Res.* **1986**, *19*, 162-168.

(180) Faustino, P. J.; Yang, Y.; Progar, J. J.; Brownell, C. R.; Sadrieh, N.; May, J. C.; Leutzinger, E.; Place, D. A.; Duffy, E. P.; Houn, F.; Loewke, S. A.; Mecozzi, V. J.; Ellison, C. D.; Khan, M. A.; Hussain, A. S.; Lyon, R. C. *Journal of Pharmaceutical and Biomedical Analysis* **2008**, *47*, 114-125.

(181) Ware, M. *J. Chem. Educ.* **2008**, *85*, 612-621.

(182) Karyakin, A. A. *Electroanalysis* **2001**, *13*, 813-819.

(183) Lopez-Palacios, J.; Heras, A.; Colina, A.; Ruiz, V. *Electrochim. Acta* **2004**, *49*, 1027-1033.

(184) Herren, F.; Fischer, P.; Ludi, A.; Halg, W. *Inorg. Chem.* **1980**, *19*, 956-959.

(185) Du, L.; Chen, J. Z.; Qi, Y. T.; Li, D.; Yuan, C. G.; Lin, M. C.; Yew, D. T.; Kung, H. F.; Yu, J. C.; Lai, L. H. *Int. J. Nanomed.* **2007**, *2*, 805-812.

(186) Hauger, O.; Frost, E. E.; van Heeswijk, R.; Deminiere, C.; Xue, R.; Delmas, Y.; Combe, C.; Moonen, C. T. W.; Grenier, N.; Bulte, J. W. M. *Radiology* **2006**, *238*, 200-210.

(187) Holzapfel, V.; Lorenz, M.; Weiss, C. K.; Schrezenmeier, H.; Landfester, K.; Mailander, V. *J. Phys. Condens. Matter* **2006**, *18*, S2581-S2594.

(188) Koncki, R.; Wolfbeis, O. S. *Analytical Chemistry* **1998**, *70*, 2544-2550.

(189) Neff, V. D. *Journal of the Electrochemical Society* **1978**, *125*, 886-887.

(190) Bonhote, P.; Gogniat, E.; Campus, F.; Walder, L.; Gratzel, M. *Displays* **1999**, *20*, 137-144.

(191) Somani, P.; Radhakrishnan, S. *Mater. Chem. Phys.* **2002**, *76*, 15-19.

(192) Ricci, F.; Palleschi, G. *Biosens. Bioelectron.* **2005**, *21*, 389-407.

(193) Selvarani, G.; Prashant, S. K.; Sahu, A. K.; Sridhar, P.; Pitchumani, S.; Shukla, A. K. *J. Power Sources* **2008**, *178*, 86-91.

(194) Hoffman, R. S.; Stringer, J. A.; Feinberg, R. S.; Goldfrank, L. R. *Journal of Toxicology-Clinical Toxicology* **1999**, *37*, 833-837.

(195) Nigrovic, V. *Physics in Medicine and Biology* **1965**, *10*, 81-&.

(196) Verdaguer, M. *Science* **1996**, *272*, 698-699.

(197) Rentschler, E.; Affronte, M.; Massobrio, C.; Rabu, P. *Solid State Sci.* **2009**, *11*, 970-971.

(198) Martinez-Garcia, R.; Knobel, M.; Reguera, E. *J. Phys. Chem. B* **2006**, *110*, 7296-7303.

(199) Sato, O. *J. Solid State Electrochem.* **2007**, *11*, 773-779.

(200) Sato, O.; Iyoda, T.; Fujishima, A.; Hashimoto, K. *Science* **1996**, *272*, 704-705.

(201) Sato, O.; Kawakami, T.; Kimura, M.; Hishiya, S.; Kubo, S.; Einaga, Y. *J. Amer. Chem. Soc.* **2004**, *126*, 13176-13177.

(202) Itaya, K.; Akahoshi, H.; Toshima, S. *J. Electrochem. Soc.* **1982**, *129*, 1498-1500.

(203) Siperko, L. M.; Kuwana, T. *J. Electrochem. Soc.* **1983**, *130*, 396-402.

(204) Orton.

(205) Bhadeshia, H. K. D. H.

(206) Somani, P.; Mandale, A. B.; Radhakrishnan, S. *Acta Mater.* **2000**, *48*, 2859-2871.

(207) Feldman, B. J.; Murray, R. W. *Inorg. Chem.* **1987**, *26*, 1702-1708.

(208) Kulesza, P. J. *J. Electroanal. Chem.* **1990**, *289*, 103-116.

(209) Kulesza, P. J.; Chelmecki, G.; Galadyk, B. *J. Electroanal. Chem.* **1993**, *347*, 417-423.

(210) Kulesza, P. J.; Doblhofer, K. *J. Electroanal. Chem.* **1989**, *274*, 95-105.

(211) Kulesza, P. J.; Zamponi, S.; Berrettoni, M.; Marassi, R.; Malik, M. A. *Electrochim. Acta* **1995**, *40*, 681-688.

(212) Xidis, A.; Neff, V. D. *J. of Electrochem. Soc.* **1991**, *138*, 3637-3642.

(213) Buschmann, W. E.; Ensling, J.; Gutlich, P.; Miller, J. S. *Chem. Eur. J.* **1999**, *5*, 3019-3028.

(214) Bonnet, F.; Ropital, F.; Lecour, P.; Espinat, D.; Huiban, Y.; Gengembre, L.; Berthier, Y.; Marcus, P. *Surf. Interface Anal.* **2002**, *34*, 418-422.

(215) Keller, P.; Strehblow, H. H. *Corros. Sci.* **2004**, *46*, 1939-1952.

(216) Vayer, M.; Reynaud, I.; Erre, R. *J. Mater. Sci.* **2000**, *35*, 2581-2587.

(217) Xidis, A.; Neff, V. D. *J. Electrochem. Soc.* **1991**, *138*, 3637-3642.

(218) Zadronecki, M.; Wrona, P. K.; Galus, Z. *J. Electrochem. Soc.* **1999**, *146*, 620-627.

(219) Pramanik, S.; Das, D.; Das, K.; Bhattacharya, S. C. *J. Nanosci. Nanotechno.* **2007**, *7*, 663-667.

(220) Agnihotry, S. A.; Singh, P.; Joshi, A. G.; Singh, D. P.; Sood, K. N.; Shivaprasad, S. M. *Electrochim. Acta* **2006**, *51*, 4291-4301.

(221) Bal, B.; Ganguli, S.; Bhattacharya, M. *J. Phys. Chem.* **1984**, *88*, 4575-4577.

(222) Liang, G. D.; Xu, J. T.; Wang, X. S. *J. Amer. Chem. Soc.* **2009**, *131*, 5378-+.

(223) Shores, M. P.; Beauvais, L. G.; Long, J. R. *J. Amer. Chem. Soc.* **1999**, *121*, 775-779.

(224) Gindy, M. E.; Prud'homme, R. K. *Expert Opin.Drug Delivery* **2009**, *6*, 865-878.

(225) Haller, C.; Hizoh, I. *Invest. Radiol.* **2004**, *39*, 149-154.

(226) Mulder, W. J. M.; Koole, R.; Brandwijk, R. J.; Storm, G.; Chin, P. T. K.; Strijkers, G. J.; Donega, C. D.; Nicolay, K.; Griffioen, A. W. *Nano Lett.* **2006**, *6*, 1-6.

(227) Sun, C.; Lee, J. S. H.; Zhang, M. Q. *Adv. Drug Delivery Rev.* **2008**, *60*, 1252-1265.

(228) Ethayaraja, M.; Ravikumar, C.; Muthukumaran, D.; Dutta, K.; Bandyopadhyaya, R. *J. Phys. Chem. C* **2007**, *111*, 3246-3252.

(229) Santos, M. J. L.; Ferreira, J.; Radovanovic, E.; Romano, R.; Alves, O. L.; Girotto, E. M. *Thin Solid Films* **2009**, *517*, 5523-5529.

Vita

Farah Nazih Radwan was born on March 11th, 1984 in Ryadh, Saudi Arabia and is a Jordanian citizen. She Graduated from James River High School, Richmond, VA in 2001. She received her Bachelor of Science from Virginia Commonwealth University, Richmond, VA in 2005. She worked as a graduate teaching assistant during her graduate studies at Virginia Commonwealth University.